DC Breakdown in gases for complex geometries from high vacuum to atmospheric pressure

THÈSE N° 5962 (2013)

PRÉSENTÉE LE 29 NOVEMBRE 2013
À LA FACULTÉ DES SCIENCES DE BASE
CRPP - PROCÉDÉS PLASMAS
PROGRAMME DOCTORAL EN PHYSIQUE

ÉCOLE POLYTECHNIQUE FÉDÉRALE DE LAUSANNE

POUR L'OBTENTION DU GRADE DE DOCTEUR ÈS SCIENCES

PAR

Ralph SCHNYDER

acceptée sur proposition du jury:

Prof. N. Grandjean, président du jury
Dr C. Hollenstein, Dr A. Howling, directeurs de thèse
Dr I. Furno, rapporteur
Dr S. Nebuloni, rapporteur
Prof. Ph. R. von Rohr, rapporteur

EPFL

ÉCOLE POLYTECHNIQUE
FÉDÉRALE DE LAUSANNE

Suisse
2013

"Everything Should Be Made as Simple as Possible,
But Not Simpler."

Albert Einstein

"Il vaut mieux viser la perfection et la manquer
que viser l'imperfection et l'atteindre."

Bertrand Russell

Abstract

This thesis presents an experimental investigation and a numerical simulation of breakdown in a ring assembly. Previous works are mostly limited to breakdown in simple geometries such as parallel plates or pin-to-plate. Here we discuss the effect of more complex geometries for DC breakdown in gases over a large pressure range from high vacuum to atmospheric pressure. The breakdown voltage versus pressure curves shows a similar shape as Paschen curves but with a wide flat plateau between the low and high pressure thresholds. The low pressure threshold determines the limit between gas and vacuum discharges. Additional optical emission spectroscopy confirms the presence of two different kinds of discharges: Gas and vacuum discharges. Moreover the global shape of the gas breakdown voltage curve in the ring assembly has been fully understood by a complementary numerical simulation. Further current-voltage study showed that voltage only is the most significant factor for breakdown and that current determines the kind of discharge after breakdown. As the breakdown voltages are lower for gas discharges than for vacuum discharges, a numerical simulation model for gas breakdown using a fluid model was developed in order to support the experimental conclusions. Starting as simple as possible with parallel plates (1 mm and 100 mm gap width representing approximatively the shortest and longest electric field path length in the ring assembly geometry) and extending to double gap and multi-gap geometries, an understanding of the overall shape of the breakdown voltage versus pressure curve is established: The high (low) pressure thresholds of gas discharge are determined by the shortest (longest) electric field path length in a complex geometry. Moreover, the availability of multiple path lengths leads to a breakdown voltage minimum over a wide range of intermediate pressure because breakdown can occur in the most favorable gap. Finally, the numerical simulation in the ring assembly shows the importance of parameters such as the secondary electron emission coefficient which play a major role in determining the breakdown voltage value.

Résumé

Cette thèse présente une étude du break-down à savoir une initialisation d'une décharge dans une géométrie complexe. De nombreuses études ont fait état de travaux similaires portant sur des électrodes à géométrie simple (plaques parallèles ou pointe-plaque). Un assemblage d'anneaux, utilisé comme géométrie dans le cadre de cette étude, est soumis à une tension DC pour une large gamme de pressions allant de la pression atmosphérique à un vide poussé. Les résultats obtenus (tensions de break-down en fonction de la pression) ont pu distinguer les "vacuum arcs" (décharges sous vide) des décharges gazeuses qui montrent une tendance générale similaire aux courbes de Paschen. Une analyse par spectroscopie optique a confirmé la présence de ces deux types de décharge. Les mesures de courant et de tension durant le break-down ont mis en évidence le fait que la limitation du courant pouvait empêcher la décharge de se développer en arc (décharge à hauts courants pouvant être à l'origine de dommages matériels). Un modèle de simulation numérique pour des break-down de décharges gazeuses à tension DC a été développé car les décharges gazeuses présentent des tensions de break-down les plus basses. Les premiers calculs ont été fait pour une géométrie à plaques parallèles afin de valider le modèle numérique. Les tensions de break-down calculées pour une géométrie à doubles espaces comparées à celles d'une géométrie à espaces multiples (de même espace maximum et minimum que la géométrie à double espaces) ont finalement permis d'identifier les paramètres clés déterminant les seuils dans les résultats expérimentaux de la tension de break-down en fonction de la pression. Finalement les résultats numériques dans un assemblage d'anneaux présentent des similarités avec ceux obtenues expérimentalement en particulier pour les courbes de tension de break-down en fonction de la pression. Les écarts entre les mesures et les calculs suggèrent qu'une attention particulière doit être portée sur les paramètres de simulation numérique tels que les coefficients de diffusion et de mobilité des particules ainsi que le coefficient d'émission d'électrons secondaire.

Mots-clés : DC breakdown, décharge gazeuse, décharge dans le vide (vacuum discharge), courbe de Paschen, simulation du fluide, géométrie complexe, assemblage d'anneaux, multi espaces, double espaces, large gamme de pression.

Contents

Contents

1 Introduction

Discharge physics is widely studied in industry and research. Discharges are used in various applications such as:

- Electrical discharge machining

- Lamps

- Cleaning

- Thin film deposition or coating

- Lightning.

High voltage devices are commonly used all around the world from electrostatic precipitators to power supplies for X-ray generators. Because these devices are working with high voltages, they are subject to possible failures originated by arcing. Arcing, which is the formation of an electric arc, is one of the most important discharge topics. The understanding of the arcing physics will help to avoid failure or damaging by redesigning or limiting the working settings of the high voltage devices. Satellite slip ring assemblies are a key element of high voltage applications in space. The robustness of electrical equipment is fundamental for space mission. Part of so-called collectors slip ring assemblies find their utility in power transmission from solar panels to the main body of the satellite (figure 1.1). They are composed of many conducting rings separated by insulators. When the rings are rotating, brushes slip on the conducting rings allowing power transmission through a tiny contact. All these conducting parts are wired to the electrical power system of the satellite. The voltage difference between conducting rings may lead to arcing and as consequence electrical failures. When arcing happens, it is supposed to be originated by overvoltages created by an electrical

component such as the sequential switching serial regulators combined with gas from possible out-gassing (from the satellite materials), the propellants or conductive plasma from the thrusters or micro-meteorite. Arcing can then be responsible for electrical continuity failures such as soldered point failure, slip wire failure, insulation failure or short circuit [1]. Satellite slip ring assemblies are designed to withstand high voltages without arcing over a large pressure range (from atmospheric pressure on earth to high vacuum in space). The demand for higher electrical power [2] and smaller devices dimensions (higher performance with smaller costs) translates to higher arcing probabilities. An understanding of breakdown may lead to new designs, and highlight the working limits of these pieces of equipment, or might suggest design modifications to improve future devices.

The electrode configuration investigated in this thesis is used not only in the particular satellite application but similar electrode geometries can be found in other devices such as slip ring motors, wind turbines or electrical generators for AC systems, alternators and in packaging machinery. This knowledge is crucial for proper functioning without breakdown. The presented results should give step by step an insight into fundamental properties of DC breakdown in complex geometries.
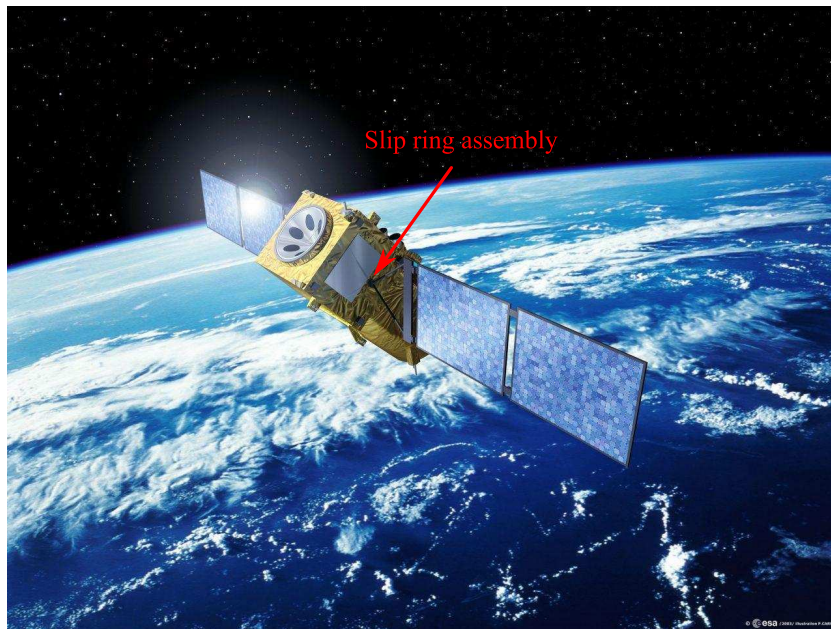

Figure 1.1: Location of slip ring assembly used for power transmission in a typical space satellite.

1.1 Plasma

Plasma science began with Crookes at the end of the 19th century [3] directly followed by Langumir at the begin of the 20th century [4]. Plasma science grew then over the years. More recent literature such as "Principles of plasma processing" from Chen [5] or "Principles of plasma discharges and materials processing" from Lieberman [6] describe the principles of plasmas developed since the beginning.

A plasma can be considered as the fourth state of matter. For a fixed pressure, the temperature of a solid can be increased so much that it will become liquid. If the temperature is further increased then the liquid transforms into a gas. Adding still more energy to a gas will dissociate the neutral particles into electrons and ionized atoms or molecules. To obtain a plasma from a gas more energy needs to be introduced in order to ionize the gas. This charged fluid mixture is composed of neutrals as well as charged particles (ions and electrons) which can interact not only by collision but also through electromagnetic fields. The electromagnetic fields inside the plasma can therefore be modified by the charged particles moving in the volume. The charged particles are sensitive to electromagnetic field and are responsible for the plasma conductivity. To characterize the existence of this fourth state of matter, some parameters need to be defined. The Debye length is the distance above which an electric potential will be screened out by the charged particles:

$$\lambda_{\mathrm{D}} = \sqrt{\frac{\epsilon_0 \mathrm{k_B} T_{\mathrm{e}}}{n_{\mathrm{e}} e^2}} \, , \tag{1.1}$$

where ϵ_0 is the vacuum permittivity, $\mathrm{k_B}$ the Boltzmann constant, T_{e} the electron temperature, n_{e} the electron density and e the elementary charge. The plasma can only exist with the presence of a collective effect. The particles need to be close enough to influence at least another charged nearby. This condition is defined by the plasma parameter Λ_{D}: The sphere of a radius equal to the Debye length should contain at least one charge carrier.

$$\Lambda_{\mathrm{D}} = \frac{4\pi}{3} n_{\mathrm{e}} \lambda_{\mathrm{D}}^3 > 1 \, . \tag{1.2}$$

Outside this sphere the charges are screened. The plasma parameter and Debye

length will change depending on the plasma because these quantities depend on the electron density and temperature. The Debye length in a plasma have to be much smaller than the physical dimensions of the system. To satisfy this condition the ion and electron density inside the plasma must be nearly equal. This quasi neutrality property ($n_e \approx n_i$) is one of the most important plasma conditions. Charged particles will always find a way to move in order to shield out large potentials gradients and maintain equal densities of the positive and negative species.
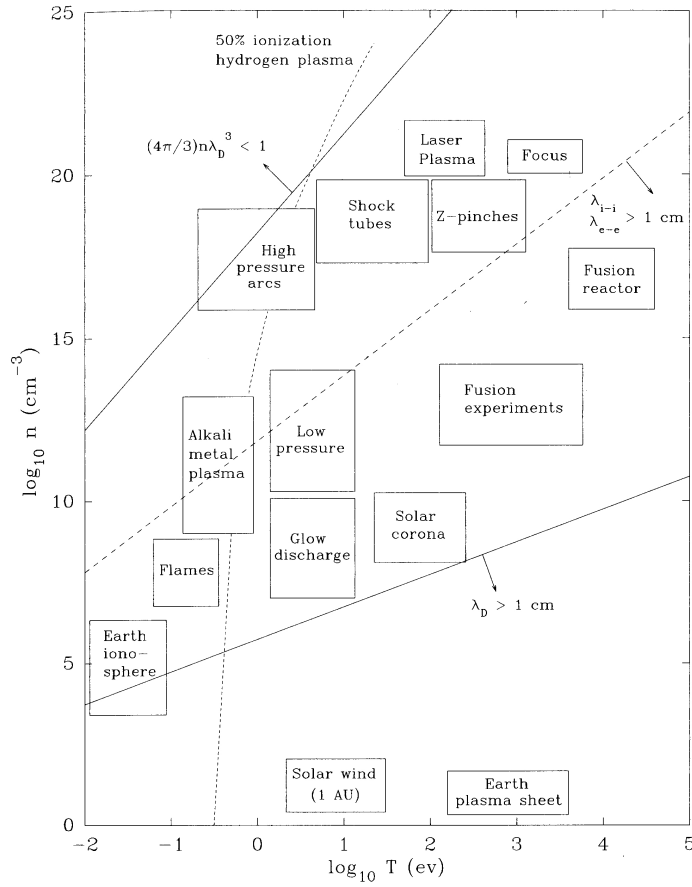
Figure 1.2: Various types of plasmas on a log-log scale, plasma density versus electron temperature [7].

Very different types of plasma exist and are summarized in figure 1.2. Large variations over several orders of magnitude in temperature and density are the origin of large varieties of plasmas. Hot plasmas such as fusion reactor plasmas fully ionize the gas (no more neutral remain). In contrast to hot plasmas, cold plasmas are only partially ionized: Only $1 - 10\%$ of the gas molecules are ionized. In this thesis we will focus on cold plasmas: glow discharges, low pressure discharges and high pressure arcs as

illustrated in figure 1.2.

The most commonly used geometry for DC plasma study is a parallel plate configuration as in figure 1.3. Two spheres or pin-to-plates geometries are also widely used. In these simple experimental configurations, one electrode is grounded whereas high voltage is applied on the other. Such simple geometries give the advantage to be able to compare experimental data with the calculated analytic solutions. The stability of a DC discharge is a question of the equilibrium between charged particle production and losses. If electrons acquire enough energy through the acceleration in the gap then they can ionize neutrals resulting in a production of ions and electrons. Nevertheless high voltage accelerates electrons and ions in the opposite direction towards the walls where they are lost. Secondary processes compensate these particles losses. One of the most important secondary process is the secondary electron emission mechanism: A positive ion can release secondary electrons from the cathode if it has enough energy when it impacts. Contrary to radio frequency (RF) plasmas, the surface processes play a main role in the DC discharge development and self-sustainment because the particles are not oscillating between the two electrodes. The steady state of DC discharges is reached when the losses are compensated by the production of particles in the volume.
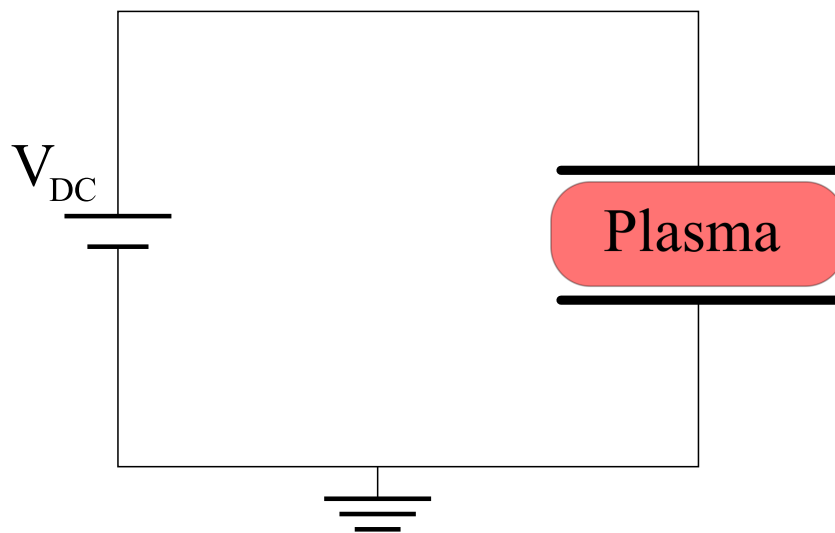

Figure 1.3: Schematic view of a plasma generated by DC voltage between a parallel plate geometry.

1.1.1 Plasma in space applications

Complex geometries such as ring assemblies used for power transmission in satellites work with high voltage. The key elements for the creation of an undesirable plasma are present: A high voltage electrode and a grounded electrode separated by gas. Some of the working conditions in the spacecraft (geometry, voltage) are known. Nevertheless parameters such as pressure are very difficult to evaluate at real functional conditions and can vary over several orders of magnitude. Some possibilities to have the presence of gas into or near the satellite are as follows:

- During the first time in space the satellite is degassing, i.e. releases gas initially attached on the surfaces or outgassing due to the pressure gradient.

- The rotation or position adjustment of a satellite is mostly done by a mono propellant rocket using hydrazine (N_2H_4) as fuel. The exhaust gas is composed by nitrogen, hydrogen and ammonia (NH_3).

- The temperature variation from shadow to sun exposure can lead to phase transition (solidification, vaporization).

- A micro-meteorite impacting on the satellite can release gas.

All these unexpected gases can temporarily create a local pressure in a part of the satellite and maybe increase the possibility of arcing. The consequences of a plasma ignition could be very different depending on nature of the discharge. Harmless discharges such as corona discharges lead only to power losses whereas arcing could be responsible for critical failures.

1.2 Objectives

The objectives of this thesis are to investigate DC breakdown in complex geometries. Understanding the occurrence and the propagation of electrical arcs under vacuum is of great importance to prevent damaging effects on equipment such as used in satellites. The study of parameters which should impact on breakdown such as pressure, voltage, gas type and geometrical parameters should help to explain the breakdown voltage versus pressure curves. Additionally optical emission spectroscopy will highlight the compositions of the discharges, results which should complement breakdown voltage investigation. Moreover the investigation in consequences of breakdown will be crucial to suggest how to possibly avoid any damaged or failures originated by a discharge in a complex geometry. The complex satellite ring assembly is simplified into

a representative simple ring assembly for investigations of geometrical parameters impact such as ring insulator thickness.

The numerical simulation should help to better understand the physics of discharge and to support the experimental results or conclusions. With an adapted model it should be possible to learn more about DC gas breakdown.

The results should finally directly be used for industrial applications: To determine the physical limits for safe operation of a typical slip ring assembly, to propose to space equipment manufacturers a scientific basis to better understand the reasons of arc occurrence on spacecraft and their onboard effects or to propose design guidelines to improve slip ring assembly arc robustness of spacecrafts.

2 DC Breakdown theory

In this chapter, the DC breakdown, a topic studied by numerous authors [8, 9, 5, 6, 10, 11, 12, 13], is briefly described. A DC breakdown can develop either into a gas or vacuum discharge. There exist many kinds of gas discharges or various ways of discharge classifications such as Townsend dark discharge, normal glow discharge, abnormal glow discharge, arc, sparks or corona discharges. Each type of discharge gives little information about the ignition processes at the origin of the breakdown. The breakdown mechanisms depend on several parameters like pressure, distance between the electrodes and electric field. After gas breakdown, the discharge develops according to the external electrical circuit. For example, if the external circuit cannot provide sufficient current to a glow discharge, it will not develop into an electric arc. Contrary to gas discharges vacuum discharges are dominated by other breakdown mechanisms such as field emission.

2.1   Gas breakdown

Initially the volume between the electrodes is filled with gas and a voltage is applied building up an electric field. If the field is high enough a free electron (from cosmic rays background ionization) is accelerated sufficiently to ionize a gas particle as shown in figure 2.1. If the electric field is maintained the two remaining electrons could ionize again each releasing an electron, and so on. This primary process of electron multiplication is called the Townsend mechanism or Townsend avalanche. Note that an electron emitted close to the anode cannot produce much ionization because it cannot travel far before it is neutralized. At the opposite end, an electron born close to the cathode travels through the full gap and has much more ionization capabilities. The ionization can be quantified by the ionization frequency (number of ionizations per unit time). As the electrons evolve not only in time but also in space (drift direction

of knocked-out electrons), the ionization is interpreted by the ionization coefficient instead of by the ionization frequency: Number of ionization events performed by an electron in a path per unit length along the field. The ionization coefficient is represented by α (Townsend's first coefficient). From numerical and theoretical analysis, the empirical expression of α commonly used is:

$$\alpha = Ap\exp(-Bp/E)\,, \tag{2.1}$$

where A and B are constant parameters determined experimentally, depending on the type of gas as presented in [6, Table 14.1] or [9, Table 4.1]. p is the pressure and E the electric field. The Townsend mechanism could be accompanied by other volume ionization mechanisms such as photoionization ($A + \gamma \rightarrow A^+ + e$), ionization by excited atoms or metasables ($A + A^* \rightarrow A^+ + e + A$), or associative ionization ($A + A^* \rightarrow A_2^+ + e$). On the other hand recombination processes are also possible by different ways. Dissociative recombination ($A_2^+ + e \rightarrow A + A^*$) or radiative recombination ($A^+ + e \rightarrow A + \gamma$) are two of them. Moreover gases with a high electron affinity can remove free electrons from the volume by attachment. Breakdown can only occur if the electron/ion production dominates the losses. DC breakdown has constantly an applied electric field accelerating the charged particles. Nevertheless if the voltage is pulsed, the charged particles are only accelerated during the pulse duration when the voltage is applied. A pulse voltage is characterized by three parameters impacting on the breakdown development:

- The pulse intensity or amplitude, impacting on how fast the charged particles are accelerated, must be high enough so that electrons born in the volume during the pulse generates enough new particles before the particles are lost by the mechanisms cited above. If enough particle remain when the next pulse occurs, breakdown starts.

- The pulse length, determining how long the voltage is applied, must be long enough. This affects how long the charged particles are accelerated in the volume.

- The pulse frequency is the number of pulses per unit time. It must be high enough so that the duration between two pulses is short, because no charged particles are accelerated and only losses occur between two pulses.

The Townsend mechanism cannot initiate breakdown by itself, but needs some complementary mechanisms such as secondary electron emission. Secondary electron
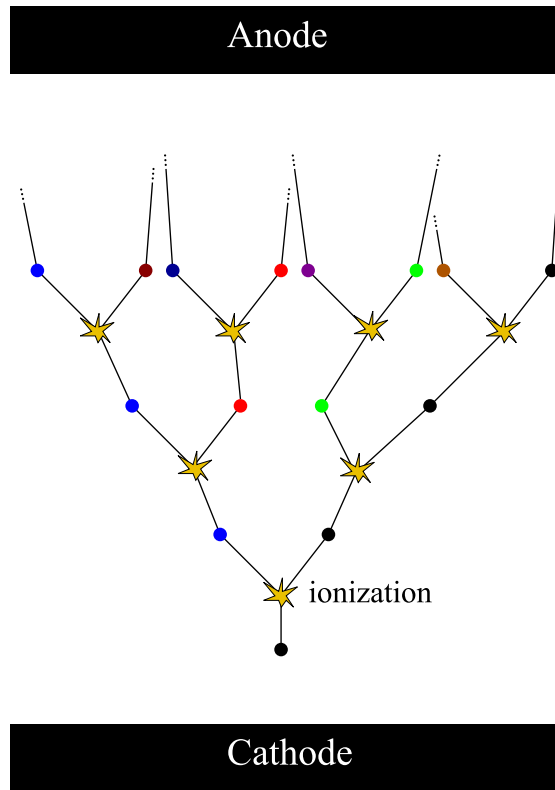
Figure 2.1: Schematic of electron multiplication starting with an initial free electron (•) accelerated by the field and moving toward the anode.

emission involves excited atoms, metasables and photons which contribute to electron production. Nevertheless secondary electron emission by positive ion impact on the cathode is the dominant mechanisms in gas discharges such as glow or corona discharges: An ion accelerated by the field and impacting on a surface has enough energy to released one or more electrons from the surface. This mechanism illustrated in figure 2.2 is in reality quite complex [6]. Figure 2.2(a) shows the confinement of electrons in a solid (metal). The electrons fill the energy levels of the conduction band whose maximum energy is the Fermi level $\mathscr{E}_\text{F}$. These electrons are confined in the solid by a potential barrier of at least height $\mathscr{E}_\phi$ (work function). An incident ion on the cathode cannot directly knock out an electron due to its relatively small kinetic energy. But approaching close enough (atomic dimensions) to the cathode surface as in figure 2.2(b), the ion replaces the existing potential barrier seen by the electrons (figure 2.2(a)) by a deep potential well which is separated from the surface only by very thin potential barrier ($\sim$atomic radius a_eff). There is also a possibility for an electron with an energy $\mathscr{E}_\text{e1}$ (one of the energy levels of the conduction band) to tunnel through the barrier, enter into the ground state of the ionized atom ($\mathscr{E}_\text{iz}$) and

neutralize the ion. This remaining energy $\mathscr{E}_{iz} - \mathscr{E}_{e1}$ is acquired by a second electron from the conduction band of the metal with an initial energy of $\mathscr{E}_{e2}$. If the exceeding energy of neutralization is bigger than the second electron energy ($\mathscr{E}_{iz} - \mathscr{E}_{e1} > \mathscr{E}_{e2}$), then the second electron could leave the surface (Auger emission) as a free electron. Otherwise it remains trapped in the surface. Depending on the energy of the ion and the potential energies of the electrons in the conduction band, more than one secondary electron could escape from the surface. The secondary emission coefficient is defined as γ_{se} and quantifies the number of electrons released per ion impact on the surface.

A discharge strongly depends on the first ionization coefficient α and the secondary electron emission coefficient γ_{se} and becomes self sustained when the current flowing between the electrodes continues to grow with the voltage increase due to the primary and secondary processes. Its breakdown initiation takes its origin in the charge multiplication. The simplest way to describe this phenomenon can be found in [6]: In a parallel plate configuration of gap width d, $z = 0$ is fixed at the cathode. Electrons are emitted at the cathode and are accelerated towards the anode by the electric field. They ionize the background gas which is quantified by the Townsend first coefficient α (ionization coefficient). The electron flux Γ_e across the gap is given by:

$$d\Gamma_e = \alpha(z)\Gamma_e dz. \tag{2.2}$$

The solution of this equation is:

$$\Gamma_e(z) = \Gamma_e(0) \exp\left(\int_0^z \alpha(z')dz'\right). \tag{2.3}$$

Taking into account the ion fluxes, the continuity of the total charge or creation of electron-ion pairs must be satisfied:

$$\Gamma_i(0) - \Gamma_i(d) \quad = \quad \Gamma_e(d) - \Gamma_e(0) \tag{2.4}$$

$$= \quad \Gamma_e(0)\left[\exp\left(\int_0^d \alpha(z)dz\right) - 1\right] \quad \text{from equation (2.3)}. \tag{2.5}$$

The ion flux at the anode $\Gamma_i(d) = 0$ and the secondary electron emission at the cathode needs to be added for breakdown of a self-sustained discharge: $\gamma_{se}\Gamma_i(0) = \Gamma_e(0)$. The condition for self-sustainment could be written by:

$$\exp\left(\int_0^d \alpha(z)dz\right) = 1 + \frac{1}{\gamma_{se}}. \tag{2.6}$$

Surface

Metal | Free space

$\mathcal{E}_\phi$

$\Phi = 0$

Electrons $\mathcal{E}_F$

(a)

Auger
emission

a_{eff}

$\Phi = 0$

$\mathcal{E}_\phi$ $\mathcal{E}_{e2}$ $\mathcal{E}_{e1}$

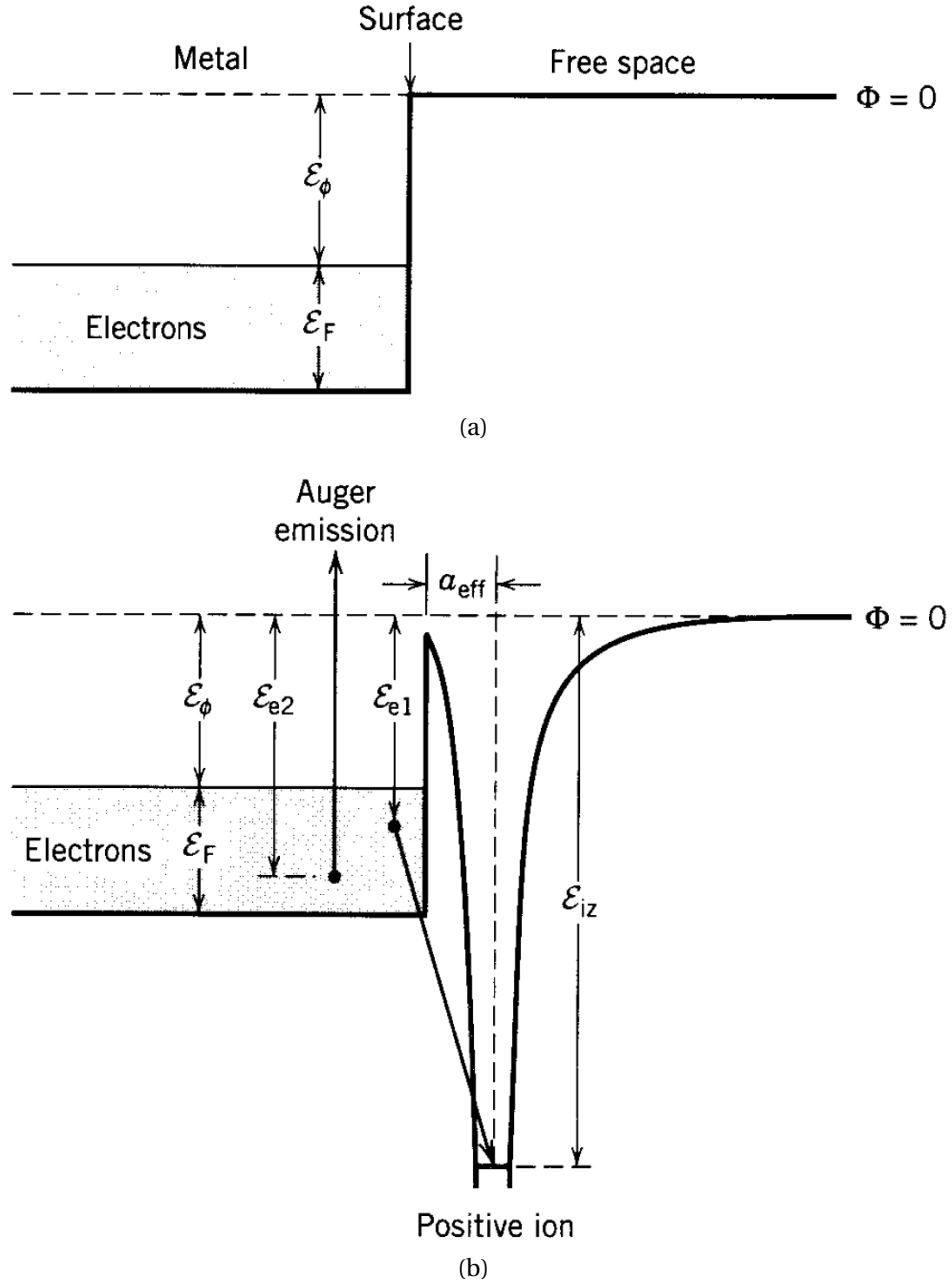Electrons $\mathcal{E}_F$

$\mathcal{E}_{iz}$

Positive ion

(b)

Figure 2.2: Potential energy at the metal surface [6]. (a) Without ion, the Fermi energy $\mathcal{E}_F$ and the work function $\mathcal{E}_\phi$. (b) Illustration of secondary electron emission by ion impact on metal surface. The presence of an ion changes the potential leading to Auger emission due to electron tunneling.

This condition in equation (2.6) describes an exponential increase of current or a charge multiplication. Assuming that $\alpha(z) = $ const in a parallel plate geometry of gap d, the condition for breakdown can be expressed by:

$$\alpha d = \ln(1 + 1/\gamma_{se}) \tag{2.7}$$

For a typical value of $\gamma_{se} = 0.01$, the breakdown condition is $\alpha d = 4.61$. The breakdown condition in complex geometries (non-uniform electric fields) becomes [9]:

$$\int \alpha(x)dx = \ln(1 + 1/\gamma_{se}) \, , \tag{2.8}$$

integrated along the electrons' trajectories.

2.1.1 Breakdown voltage

As introduced before, an electric field applied to electrodes can initiate a breakdown. The breakdown of a discharge depend therefore on the electric field or the applied voltage. The electric field in a parallel plate geometry is given by $E = V/d$, where V is the voltage and d the inter-electrode gap. The gas discharge breakdown voltage V_{Bd} as a function of the pressure p is known as the Paschen law [6]. Substituting the value of α in equation (2.7) by equation (2.1), we obtain:

$$Ap\exp(-Bp/E)\,d \;=\; \ln(1 + 1/\gamma_{se})$$

$$\Rightarrow \frac{-Bp}{E} \;=\; \ln\left[\frac{\ln(1 + 1/\gamma_{se})}{Apd}\right] = \ln[\ln(1 + 1/\gamma_{se})] - \ln[Apd]$$

Using $E = V/d$, the equation becomes:

$$\frac{-Bpd}{V} = \ln[\ln(1 + 1/\gamma_{se})] - \ln[Apd]$$

Finally the breakdown voltage is expressed by:

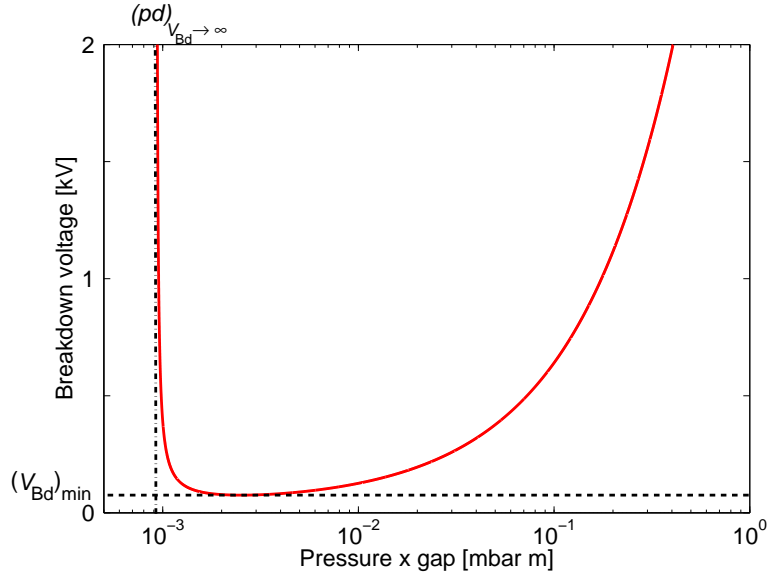$$V_{Bd} = \frac{B\,pd}{\ln(A\,pd) - \ln[\ln(1 + 1/\gamma_{se})]} \, . \tag{2.9}$$

Figure 2.3: Typical Paschen curve for a parallel plate geometry based on equation equation (2.9).

The breakdown voltage is a function only of the product pd. This expression is called Paschen law. There are significant differences between the A and B values given in the literature. Each experiment can be slightly different from others (procedure, geometry, material, purity of gases,...) and therefore gives different values but of the same order of magnitude. From equation (2.9), the lower limit of pd for asymptotic V_{Bd} can be expressed and shown in figure 2.3:

$$(pd)_{V_{\mathrm{Bd}} \to \infty} = \frac{\ln(1 + 1/\gamma_{\mathrm{se}})}{A} \; . \tag{2.10}$$

This expression depends on the type of gas through A, and on γ_{se} and determines the threshold between gas and vacuum breakdown. The minimum breakdown voltage can also be determined:

$$(V_{\mathrm{Bd}})_{\min} = \frac{\exp(1) B \ln(1 + 1/\gamma_{\mathrm{se}})}{A} \; . \tag{2.11}$$

The breakdown approach using the Townsend breakdown criterion can be used to estimated the parameters involved in the equation (A, B and γ_{se}) for a wide range of pd values in gases [14].

2.1.2 Gas discharges

Each gas discharges is characterized by the current and the voltage. Figure 2.4 taken from [8] shows the current-voltage curves of some discharges (Townsend dark discharges, corona, glow discharges and arcs) for different geometries, pressures and various gases. For a specific geometry and pressure there can be different kinds of discharges. For example at atmospheric pressure in a pin-to-plate geometry three different discharges (corona, glow and spark discharges) are identified according to current and voltage [15]. Figure 2.5 shows a schematic of a current-voltage curve for a geometry, pressure and gas where many types of discharge could occur. The external electrical circuit provides the voltage and the current and forms a closed circuit. If the power supply is followed by an external resistance, the load line is defined by the following equation and illustrated figure 2.5:

$$\varepsilon = V + \Omega i \,, \tag{2.12}$$

where Ω is the external resistance and ε the electromotive force provided by the power supply. The intersection of the current-voltage curve and the load line determines the discharge current and voltage characteristics and depends therefore on the external electrical circuit. High current discharges such as arcs can damage the experimental setup. The external resistance determines the slope of the load line in such a way that it can avoid that a low current discharge (glow or corona discharge) develops into an powerful high current discharge (arc). External current limitation is very useful for non destructive tests such as breakdown studies if the power supply is not limited in current.

The current-voltage curve shows that different discharges can be achieved. If a voltage below the breakdown voltage is applied, a small current can be measured. This phenomenon is illustrated in figure 2.5 by (AB) and is called dark current. No self-sustained discharge can develop in this region, which can be named as a non self-sustained discharge region.

Townsend discharge

If the external resistance is so high that the circuit can provide only very weak currents ($i \sim 10^{-10} - 10^{-5}$ A), the electron and ions densities are so low that space charges are negligible and therefore the external field is not distorted. As long as the space charge is weak, the electric field is independent of the charge and the voltage on the current-voltage curve is constant (BC on figure 2.5). This very low current discharges
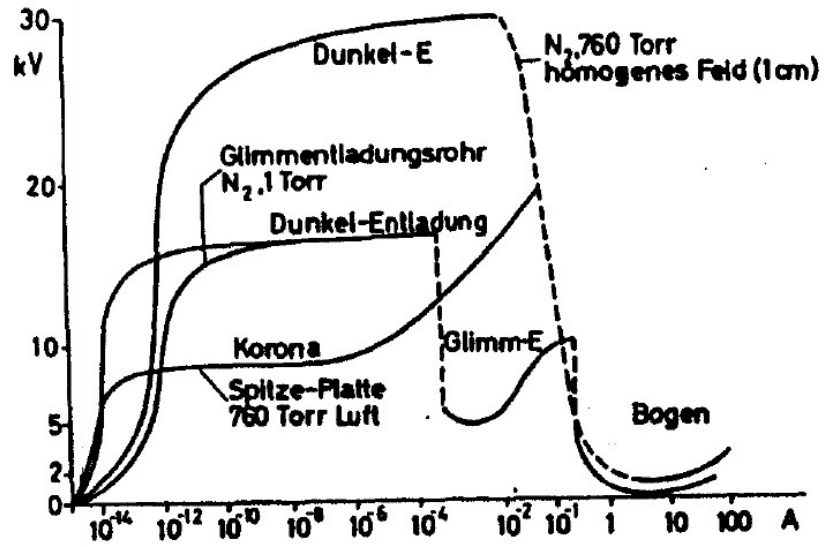
Figure 2.4: Current-voltage characteristics extracted from [8] for different pressures, gases and geometries.
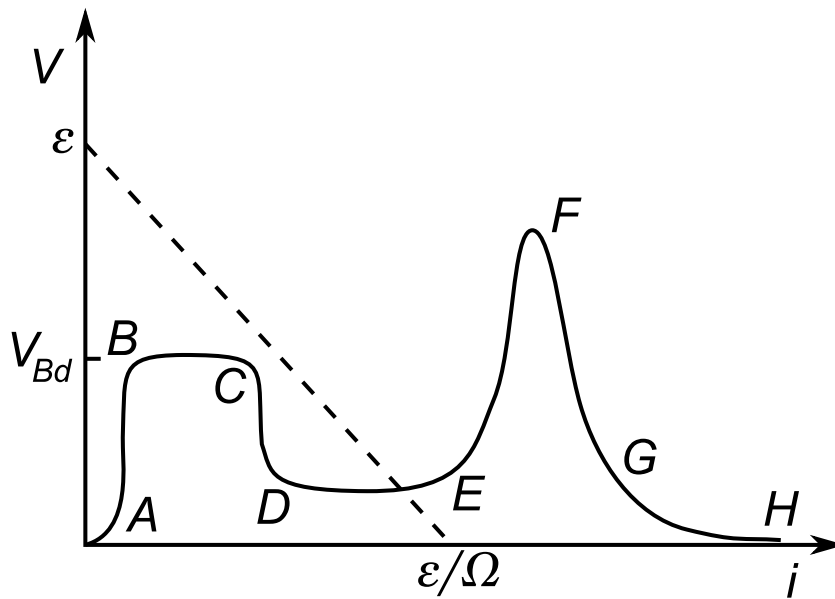

Figure 2.5: Schematic of a current-voltage characteristic curve in a discharge tube and a load line from [9] : (AB) dark current, (BC) Townsend or dark discharge, (DE) normal glow, (EF) abnormal glow, (FG) transition to arc, (GH) arc.

are called Townsend or dark discharge and need sensitive instruments to be measured. The ionization in these discharges is so small that the emitted light is hardly visible [9]. This explains the origin of the discharge's name: dark discharge. Our current probes are not sensitive enough to measure such low currents. This kind of gas discharge could therefore be observed but not measured.

Glow discharge

In figure 2.5 the section (DF) represents the glow discharge: normal glow (DE) and abnormal glow (EF) discharge. After a voltage drop (CD) the normal glow discharge forms and remains with a constant voltage over a large range of current ($i \sim 10^{-4} - 10^{-1}$ A). When the current is increased or decreased during a normal glow (DE), the glow on cathode surface expand respectively contracts. Nevertheless the total current density remains the same because the current variation is compensated by a change in the surface area through which the current flows.

When the current during a normal glow discharge is increased (above 10^{-1} A) so much that every cathode surface is covered by the glow, the total current density could only be increased by a voltage increase because the charged particles need to be more accelerated by the electric field. This discharge is called abnormal glow discharge (EF). Compared to the normal glow discharge, it becomes more bright and extends in the volume with a current increase.

Self-sustained glow discharges in non-uniform electric field are called corona. The electric field depends on the geometry: In a parallel plate configuration it is constant in the volume whereas in a pin-to-plate geometry it is non-uniform. In complex geometries the field can be strongly non-uniform. Charged particles can therefore be much more accelerated in the region where the electric field is strong. The glow discharge will only develop in this enhanced electric field region. The charge multiplication for discharge initiation depends on the electrode polarity:

- If the electric field is concentrated around the cathode, the glow discharge is called negative corona (glow around the cathode). The discharge mechanisms do not differ much from glow discharge: The Townsend mechanism and secondary processes only occur over short paths near the cathode, where the field is enhanced [16]. As a particle move out of the enhanced field region, they are almost no more accelerated (weak electric field in the volume) losing their ionization potential [17].

18

- In contrast to negative corona, positive corona is a glow discharge around the anode where the electric field is concentrated. This discharge cannot count on secondary electron emission by ion impact on the cathode because the enhanced field is only near the anode. The secondary mechanism in the vicinity of the electrode is therefore ensured by photo processes as for streamers (see next section).

Arcs

The transition from a glow discharge to an arc occurs in the segment (FG) of figure 2.5 at around $i \sim 1\,\text{A}$ and is characterized by an abrupt voltage drop. The transition is caused by cathode heating as the current gradually increases and raises the current density of the abnormal glow [9]. The secondary emission based on knocking out electrons with ions arriving at the cathode is replaced by heating up of the metal electrode leading to thermionic field emission. This heating up method is much more efficient than the secondary electron emission by ion impact ($\gamma_{\text{se}} \sim 10^{-3} - 10^{-1}$) and could emit up to 9 electrons per ion impact on the cathode [9]. Every kind of gas discharge with sufficient high voltage and current could develop into an arc.

Streamer concept, first stage of spark

Up to this point, the breakdown mechanism has been described by the Paschen theory: ionization in the gas combined with secondary electron emission related to the cathode. However, another mechanism is known to determine breakdown in gases in particular at high pressure and high fields. The so-called streamer theory [13, 12, 9] takes into account not only ionization in the gas but also the resulting space charge. It is based on the concept of the growth of a thin channel across the gap between the electrodes. The channel built up begins with the primary avalanche. The space charge inside the avalanche creates its own electric field separating the charges. Not only ionization by collision occurs in the vicinity of the head of the avalanche but also photo ionization by energetic photons is assumed to play a decisive role. The additional produced particles by these photons are joining the primary avalanche and contributing to its propagation towards the electrode. The streamer formation criterion is fulfilled when the field of the space charges produced by avalanche reach a value of the same order of the external field. This leads to the following well-known Meek breakdown criterion (omitting attachment):

$$\int \alpha(E(l))\mathrm{d}l \geq \chi \, , \tag{2.13}$$

19

where the first Townsend coefficient $\alpha(E)$ is integrated along the electrical field line between the electrodes. Recent streamer studies [18, 19] propose χ equal to 18.5. Eriksson uses this criterion for streamer evaluation in complex geometries with inhomogeneous fields [19]. There are some differences in the proposed value of χ in the literature for uniform fields. In fact, [13] gives 17, [12] 20 and [9] 21. Moreover, in non-uniform fields the agreement with the criterion is less good [11]. Townsend's mechanisms are predominant for $pd < 2.63$ mbar m and voltages up to small overvoltages (voltages above the breakdown voltage) [9, 13] and the Meek breakdown criterion should therefore not be used for these conditions. If this criterion is applied where Townsend's mechanism is valid ($\alpha d \sim 4.61$ for $\gamma_{\text{se}} = 0.01$ from equation (2.7)) for high pd values then the breakdown voltages obtained will be overestimated [20].

The spark could be seen as a pulsed arc. The streamer breakdown could initiate a spark if a high current is possible: The spark uses the thin channel (streamer) conducting property closing the circuit to discharge through the gap with a much larger current. If the power supply can maintain the large current during the discharge, then the spark develop into an arc. Else it will burn out and build up again.

2.2   Vacuum discharges

Vacuum discharges have been described during the past few years by many authors partially listed here [9, 11, 12, 21, 22, 23]. Contrary to gas discharges, the vacuum discharge initiation mechanisms originate at the electrode because they occur in conditions (low pressure or very small gaps) where the mean free path is equal to or bigger than, the inter electrode gap. The voltages for vacuum breakdown are high because energy is first needed to release a medium such as metal vapor or adsorbed gas from the electrode used for the breakdown initialization. Pre breakdown emission processes are therefore needed.

2.2.1   Introduction and basics of electron emission

When a high electric field is applied between two electrodes in vacuum, an electron could be released from the electrode surface under some specific conditions. Farrall described this field emission phenomena in [22]. Emission means that electrons escape the surface of the electrode and it has therefore to overcome the surface energy barrier. This principle is illustrated in figure 2.6. Three different kinds of emission can be distinguished [9]:

1. Electron emission without external electric field can occur thermionically. The heat provides the sufficient energy for the electrons so that the energy levels above the Fermi level are populated figure 2.6(a). A fraction of these electron are then able to escape.

2. The method of image charge can be used to determine the potential energy of an electron outside the surface as in figure 2.6(b): An electron outside the metal at a distance x is assumed to have an image charge of opposite sign at $-x$ within the metal. An additional external field reduces the effective work function from ϕ to ϕ' as shown in figure 2.6(c) (Schottky effect). This mechanism combined to the thermionic heating is called the field enhanced thermionic emission (or thermionic field emission) and considerably increases the number of released electrons because potential barrier height is reduced.

3. Field emission is based on quantum mechanical process. There is a finite probability for an electron tunneling trough the metal over the distance δ (figure 2.6(c)). Increasing the external electric field reduces both the height and the width of the barrier at the Fermi level and therefore increasing the field emission (the probability for tunneling).
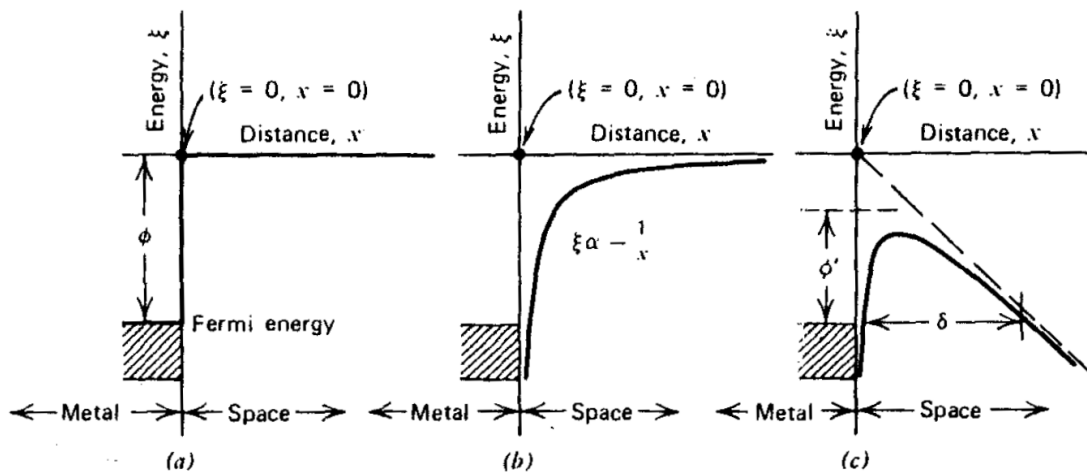

Figure 2.6: Potential energy versus distance for an electron near a metal surface from [22]: (a) without image charge, (b) with image charge, (c) with image charge and external electric field (dashed line: only electric field).

2.2.2 Field emission mechanism

The Fowler-Nordheim theory [22] describes the field emission current density J:

$$J = \frac{1.541 \cdot 10^{-2} \cdot E^2}{\phi \cdot t^2(y)} \exp\left(\frac{-6.831 \cdot 10^9 \phi^{\frac{3}{2}} v(y)}{E}\right) \quad \frac{A}{m^2} \, , \qquad (2.14)$$

where E is the local electric field, ϕ the material work function, y a parameter depending on E and ϕ ($y = 3.795 \cdot 10^{-4}\sqrt{E}/\phi$), and $t(y)$ respectively $v(y)$ are complex functions experimentally determined by Nordheim [24]. Miller gives tabulated (and corrected) values of $t(y)$ respectively $v(y)$ in [25, 26]. Moreover, E can be written as $\beta \cdot E'$ where β is the local field enhancement factor, and E' the applied field. The work function and the field enhancement factor depend strongly on surface structure and material. One way to find the field enhancement factor assuming the work function constant, is simply to write equation (2.14) as follow:

$$\ln\left(\frac{J}{E'^2}\right) = \ln\left(\frac{1.541 \cdot 10^{-2} \cdot \beta^2}{\phi \cdot t^2(y)}\right) - \frac{-6.831 \cdot 10^9 \phi^{\frac{3}{2}} v(y) \cdot \beta}{E'} \, . \qquad (2.15)$$

β can be obtained from the slope of the simple interpolation $\ln\left(\frac{J}{E'^2}\right) = m \cdot \frac{1}{E'} + h$ because the current and the electric field are easily measurable in a parallel plates geometry and the other parameters are given in literature.

Nevertheless, field emission is very sensitive to small surface changes. Surface modifications for example can lead to abrupt variations in field emission current. The local electric field enhancement factor $\beta = 1$ for perfectly smooth and clean surfaces. The aim for most applications is to obtain a β as close as possible to 1 and a high work function in order to increase the breakdown limits of their system. A defect in the surface finishing can lead to higher β. Simple gas exposure (adsorption), dirt on surfaces or other contaminants can change the work function [27, 28]. Fortunately, electrodes can be partially conditioned or cleaned by sparking with limited current. Too high currents can damage the surface and create protrusions. Some authors investigated the impact of the surface condition on breakdown strength: The use of alloys for electrode material instead of pure metal as well as the modification of the surface after heat treatment (surface layer) impact on the work function [29, 30, 31]. The number of protrusions considered as field emission emitters enhancing the local electric field can be partially removed by mechanical treatment [32] or conditioning by sparking [33].

Fowler-Nordheim theory is a powerful law for the understanding of pre breakdown current in vacuum systems. However the emission is very sensitive to surface modification [34]. It is therefore necessary to be careful with this theory, in particular with the two parameters the work function and the field enhancement factor which have been identified as important.

2.2.3 Breakdown in vacuum

When voltage is applied to the electrodes in order to have a high electric field, a current flows through the gap. Before breakdown the field emission in room temperature (cold surfaces) is the dominant emission mechanism. As the breakdown begins the high current density can only be provided by thermionic field emission [9]. Breakdown occurs when the current density approaches a critical value of $\sim 10^{12}$ A/m^2 [21]. The breakdown itself is originated by Joule heating and precipitated by vaporization of the emitter where the field is enhanced. The consequence of the electron flux striking the anode results in a positive ion flux returning to the cathode. The cathode field is therefore further enhanced due to the space charge cloud produced by the ion concentration, facilitating breakdown. The vacuum discharge can finally develop in the metal vapor, residual gas or impurities issued form the electrodes. These discharges only occur in such low pressure or small gaps where the particle densities in the volume become so low that the gas discharge could not initiate. As shown above the initiation mechanisms depend strongly on surface which is modified more or less with each vacuum discharge leading already to breakdown voltage variations simply by history.

3 Experimental Setup

This chapter describes the experimental setup and the diagnostics. Working over a large pressure range (high vacuum to atmospheric pressure) is first discussed. Then the two main setups are described: The simple ring assembly used for most of the experimental measurements and the slip ring assembly from industry. Additionally to the experimental setups, the characteristics of the different electric devices such as voltage generators or electrical probes are presented. Finally the chapter ends with a section on a method to measure the breakdown voltage and different ways to use optical emission spectroscopy results.

3.1   Pumping and gases

Breakdown measurements are performed over a wide pressure range (from $2 \cdot 10^{-5}$ to 10^3 mbar) in a cylindrical vacuum vessel as shown in figure 3.1. The vessel is 400 mm high and has a radius of 160 mm. Two large windows offer the possibility for visual observations or to install optical fibers for light intensity measurements or optical spectroscopy. A base pressure of 10^{-6} mbar is reached with a turbomolecular pump. For pressure above 0.01 mbar the turbo pump can be isolated from the vacuum chamber by a valve. Only a root pump is used in this case. Different gases can be introduced by means of a micro valve. Atmospheric pressure is obtained by reducing the pumping speed of the root pump. The pumping speed is changed by a second throttle valve placed between the chamber and the root pump. Various gases can be tested but argon, air and nitrogen have mainly been used. The pressure in the vacuum vessel is measured by a full range vacuum pressure gauge (Balzers compact full range gauge PKR 250: Pirani and cold cathode gauge combination) for pressures of $5 \cdot 10^{-9}$ to 10^3 mbar in air. The measured pressure by this gauge deviates above 1 mbar from the real pressure for gases different from air as presented in figure 3.2
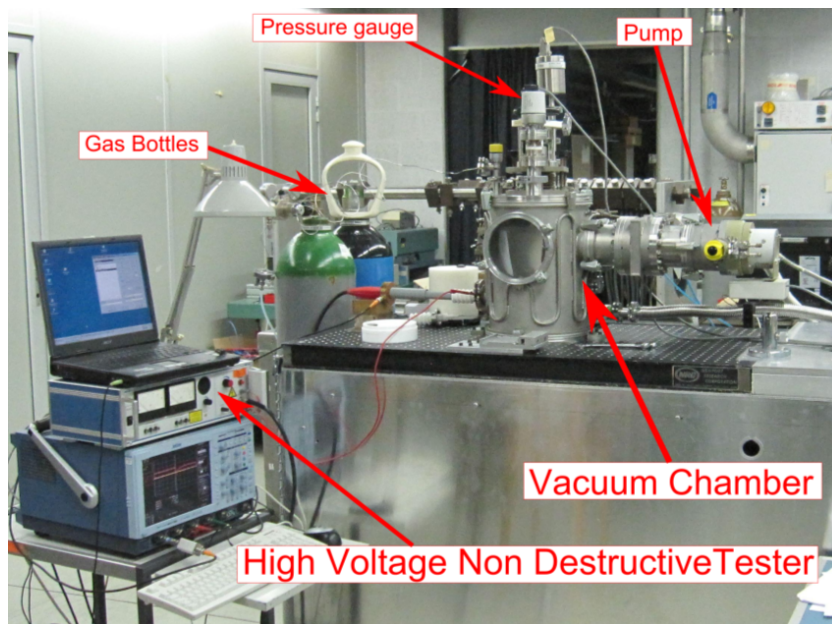
Figure 3.1: Picture of the main experimental setup without optical diagnostics.

[35]. This is explained by the physics of the Pirani gauge. Gas molecules cool the heated wire down by collisions with it. If the pressure is decreased, the number of gas molecules also decreases. Less heat is therefore removed from the heated wire and the temperature rises. As the wire resistance changes with the temperature, the pressure can be deduced. This is dependent on the kind of gas present in the chamber. Initially the probe is calibrated for air. To have a measurement independent of the gas a second pressure gauge is installed: a baratron (MKS capacitance manometer 1000 mbar model 628B13MDE1B). A so called baratron is a pressure gauge relying on a change of a capacitor capacitance by the gas pressure. It uses the metal diaphragm and an adjacent fixed electrode to create a variable capacitor to detect strain due to applied pressure. This mechanism is independent of the gas type and is used here to measure pressures above 1 mbar.

3.2 Slip ring assembly

RUAG Space produces slip ring assemblies for power transmission in satellites (figure 3.3). They need to withstand high voltages without breaking down over a wide gas pressure range. An example of a typical satellite slip ring assembly is shown in figure 3.3. It is composed of gold coated rings and brushes in order to have the best possible conductivity. The inside of this assembly is filled with an insulating resin. Arcing
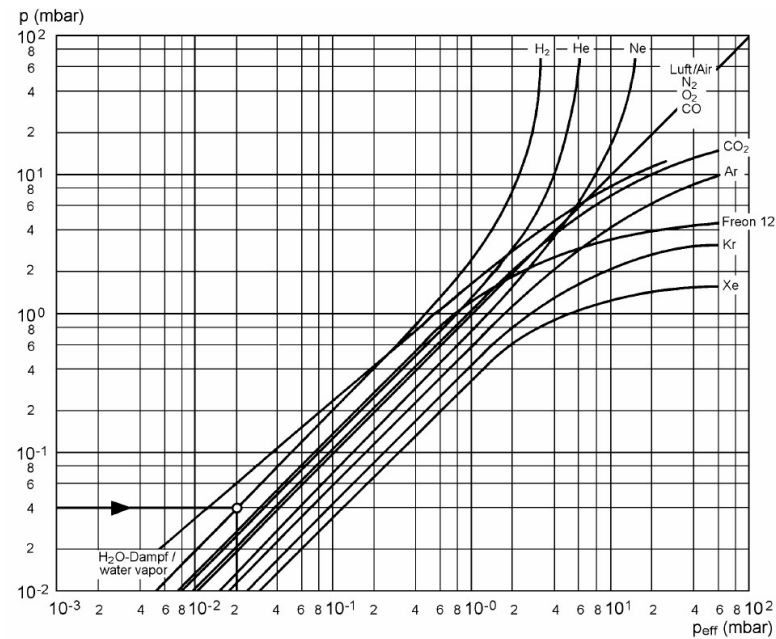
Figure 3.2: Gas dependency of indicated pressure for the Pirani gauge. The gauge is calibrated for air.

should therefore only happens externally. The slip ring assembly is responsible for the power transmission from the solar panels to the spacecraft. The slip rings are connected to the spacecraft using different tracks. Some tracks supply the voltage whereas some are grounded. The schematic of the track allocation is shown in figure 3.4. The high voltage was connected on either track 15 or 17 for the measurements of breakdown. The tracks 1 to 14 and 18 to 20 are grounded and the rest is floating.

The slip ring assembly compared to the simple ring assembly has slipping brushes on the ring, which may have an impact on breakdown voltage. In order to rotate the rotor from the outside of the vacuum chamber, an additional feed through was placed at the top of the vacuum chamber. A metal rod with a fork at its end is attached to the feed through. The fork is pushed into the top holes of the slip ring assembly in order to rotate the rotor. The brushes and external structure of the assembly remained still. Experimentally the rotation speed has been chosen higher than the functional speeds for space applications and is at about 1 rpm. For solar array drive mechanism (SADM) space applications, the functional rotation speed in geostationary conditions (GEO) is 1 turn per day whereas in low earth orbit (LEO) it is about one turn per 100 minutes.
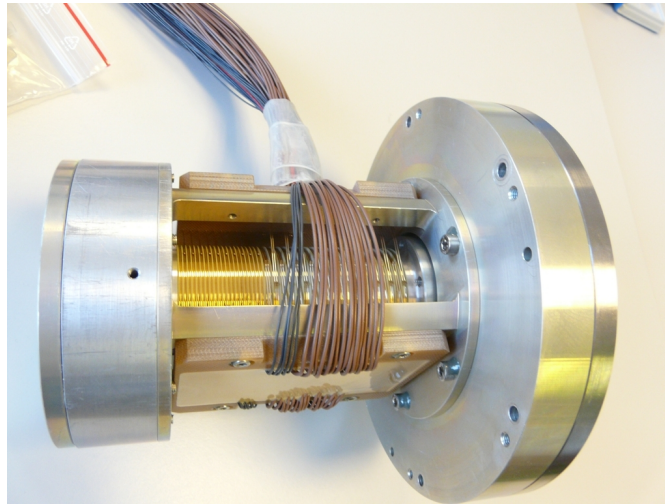
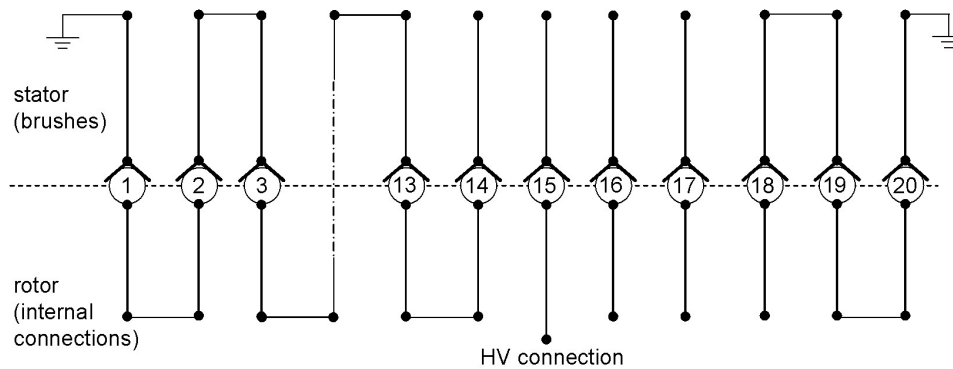Figure 3.3: Typical satellite slip ring assembly

Figure 3.4: Electrical wiring schematic of slip ring assembly. The circles represent the gold rings and the two lines are the brushes slipping on the ring during rotation. High voltage was applied on track 15 or 17 in this experiment. All other tracks are grounded or floating.
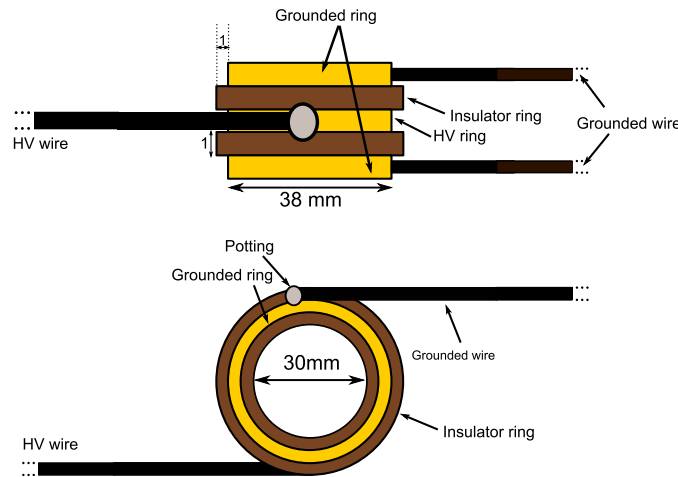
Figure 3.5: Typical dimensions of simplified adjustable ring assembly. The ring edges have a 0.1 mm radius of curvature. The surface finish of the conductors is N7 (roughness value Ra = 1.6 μm).

3.3 Simple ring assembly

In order to conveniently study breakdown for these complex geometries (slip ring assemblies) a simple easily modifiable ring assembly has been designed based on a simple structure (figure 3.5).

The complete assembly of a satellite slip ring was substituted by a representative ring geometry composed of only five rings (three conductors separated by two insulators) as shown in figure 3.5. The conductor rings were made of brass and were not gold coated as for the slip ring assembly from RUAG. The top and bottom rings are grounded whereas the middle one is at high voltage. The internal (external) ring diameter of the brass conductors is 34 mm (38 mm) and the internal diameter of the insulator rings is 30 mm (internal barrier). The external diameter of the insulator can be 38 mm (no external barrier) or 40 mm (external barrier). The ring thickness can vary from 1 mm to 4 mm by steps of 1 mm. An epoxy structural adhesive (Scotch Weld 2216 B/A) is used to cover the soldered connection (named potting) between the metal rings and the wires, except when mentioned. The ring assembly is held together by a PTFE holder (figure 3.6(b)) and is placed in the middle of the grounded cylindrical vacuum chamber (figure 3.6(a)). The PTFE holder has a hole in order to obtain pressure equilibrium between the inside of the ring assembly and the vacuum chamber. The three types of insulator material used have very different breakthrough voltages: Vetronite® G-11 20 kV/mm [36], Ultem® 2300R Resin 25 kV/mm [37], Macor® 62 kV/mm [38].
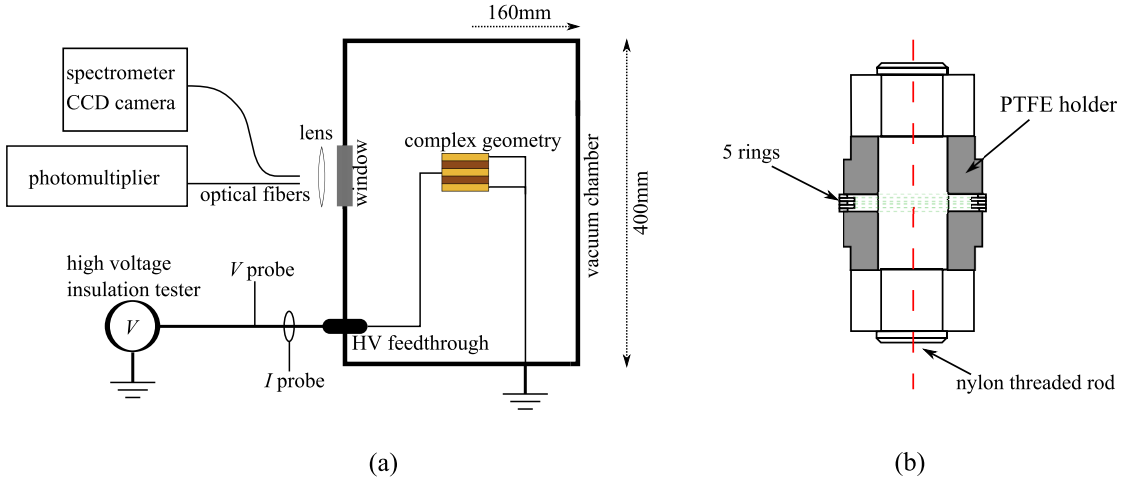
Figure 3.6: (a) Schematic drawing of the experimental setup (side view). The assembly of 5 rings is placed in the middle of the cylindrical vacuum chamber. The electrodes are brass rings: the top and bottom rings are grounded and the middle ring is at high voltage. The insulator rings are of Ultem resin. (b) Scale drawing of the ring assembly and PTFE holder. Rings thickness is 1 mm. External diameter of the rings is 38 mm.

3.4 Electrical characteristics and measurements

In high voltage breakdown studies, the connections between the experimental setup and the voltage generator must be done carefully to avoid any undesired parasitic arcing. A high voltage feed through as figure 3.7(b) makes the electric link between the inside and the outside of the vacuum chamber. Initially the feed through looks like the one presented in figure 3.7(a). The metal rod is surrounded by a PTFE piece to avoid breakdown between the rod and the grounded vacuum chamber walls. Then a high voltage connector is placed at the end of the rod as in figure 3.7(b). These high voltage connectors are suitable to connect the experimental setup to the feed through.

The breakdown processes depend not only on the applied voltage but also on its waveform. Several kinds of voltage generators are used depending on the type of measurements:

- A non-destructive high voltage insulation tester (Danbridge JP30A) is used to apply DC voltages up to 30 kV especially for DC breakdown voltage measurements (mostly for breakdown voltage versus pressure curves). No external resistance was necessary to avoid high current damaging because the tester current limit is set as low as 100 μA.

- A 3 kV high voltage generator (Glassman PK3R1300) with a regulable current limit up to 1.3 A was used for current investigations. Additional current limita-

tion could be realized by adding external inductance free resistances between the high voltage generator and the vacuum chamber. Current-voltage characteristics curves or the impact of current on discharge have been investigated.

- A pulse generator using a fast high voltage transistor switch (Behlke HTS 201-03-GSM) in the positive pulse configuration (figure 3.8) provides a square voltage waveform for a frequency of 0.4 to 4000 Hz and pulse width between 10 and 10^{-3} ms.

- Polarity and AC voltage breakdown investigation was possible with high voltage AC/DC generator (Trek Model 615-10) reaching voltages up to 20 kV AC (from 100 Hz to 10 kHz) and 10 kV DC (positive or negative).

- The last generator is directly related to the main application of the solar panels power supply [1] and will be called solar cell simulator. A simple DC voltage is not representative to the output signal produced by satellites solar panels. A pulse generator has been fabricated by the HEIG-VD from Yverdon-les-Bains (VD) representing voltage signals arriving at the ring assembly according to two different worst case electrical circuits present in satellites. It offers therefore two realistic voltage waveforms at a repetition frequency of 1 kHz: A square voltage waveform with the serial shadow diode and a pulsed voltage at 400 kHz without it as shown in figure 3.10. It is capable of reaching voltages up to 1 kV and its design is presented in figure 3.9.

| (a) | (b) |
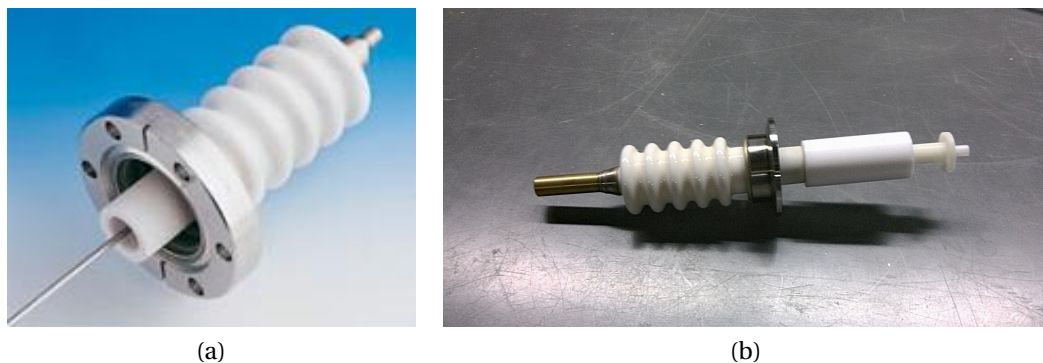
Figure 3.7: High voltage vacuum feed throughs: (a) Typical feed through without additional adaptations. (b) The feed through rod is surrounded by a PTFE piece and connected to a high voltage connector. The brass cylinder on the left makes the connection with the high voltage generator or tester at the outside of the vacuum chamber.
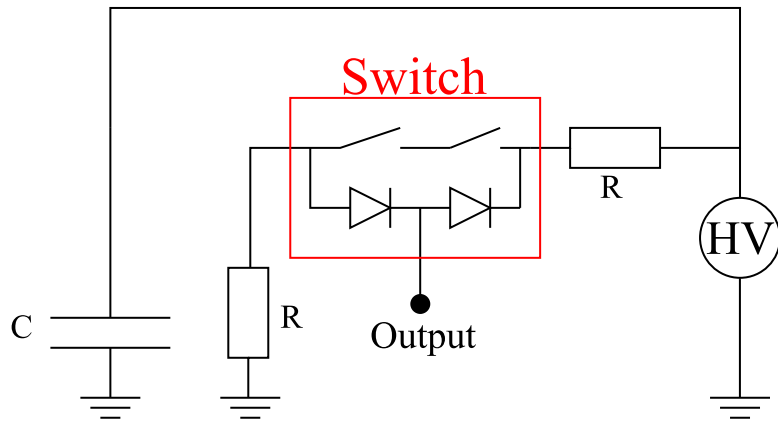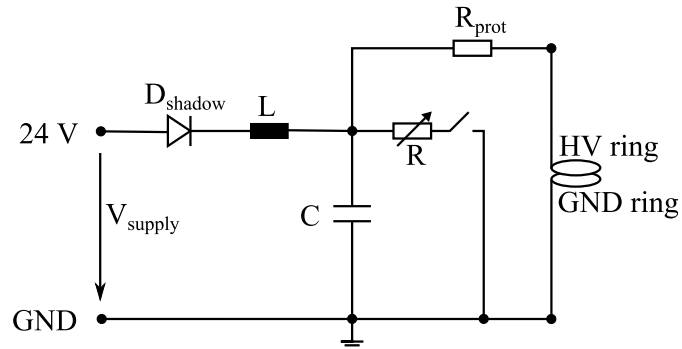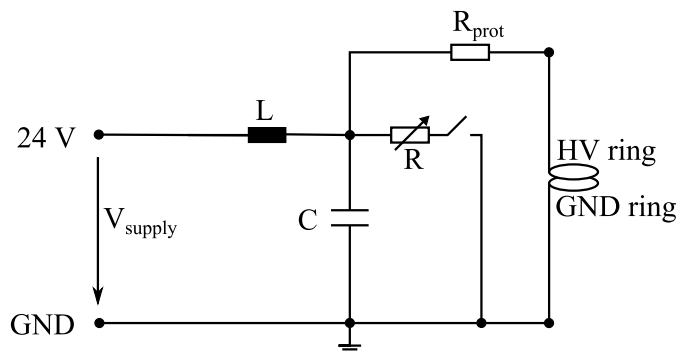
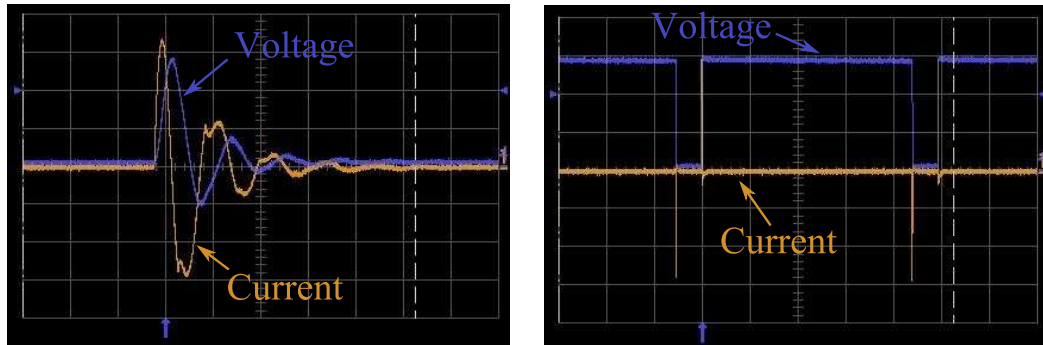Figure 3.8: Electrical circuit for a positive pulsed voltage output from [39].

(a) With shadow diode D_{shadow}

(b) Without shadow diode D_{shadow}

Figure 3.9: Pulse generator form HEIG-VD from Yverdon-les-Bains (VD) with two possible configurations.

(a) Without shadow diode (time scale : 2 μs/div)

(b) With shadow diode (time scale : 0.2 ms/div)

Figure 3.10: Summary of voltage simulator characteristics provided by HEIG-VD from Yverdon-les-Bains (VD). Current in orange (40 mA/div) and voltage in blue (100 V/div).

The voltage and current are measured with a voltage probe (LeCroy PMK 14kVAC) and a fast current transformer (Bergoz FCT-016-10:1-WB or FCT-016-100:1-WB) and read on a LeCroy wavepro 950 1GHz oscilloscope as shown in figure 3.6.

3.5 Breakdown measurement and optical emission spectroscopy

An optical fiber and lens directed towards the electrodes and connected to a photomultiplier provide light intensity measurement (see figure 3.6). When breakdown occurs, electron and ion densities grow rapidly leading to a rapid increase of current and light intensity. The measurements are stopped when either current or light intensity rise exponentially as illustrated in figure 3.11 where the time scales on the scope are at around typical a value of several μs/div. Breakdown can be determined without light intensity measurement as in figure 3.11(a). It is nevertheless easier to trigger on the light intensity for low current breakdowns. Breakdown in situations like in figure 3.11(b) can either be triggered on current or on light intensity. The breakdown voltage is defined as the voltage needed to initiate a discharge. To determine the breakdown voltage, the applied voltage is increased linearly. To avoid possible high overvoltages, the voltage increasing rate was fixed below 200 V s^{-1}. The measured DC breakdown voltage is the voltage before light or current increase because the breakdown formation time is significantly slower then the voltage ramp. The applied voltage increase rate can impact on the measured breakdown voltage. A too fast voltage ramp can lead to large overvoltages. The ideal theoretical voltage ramp to measure the breakdown
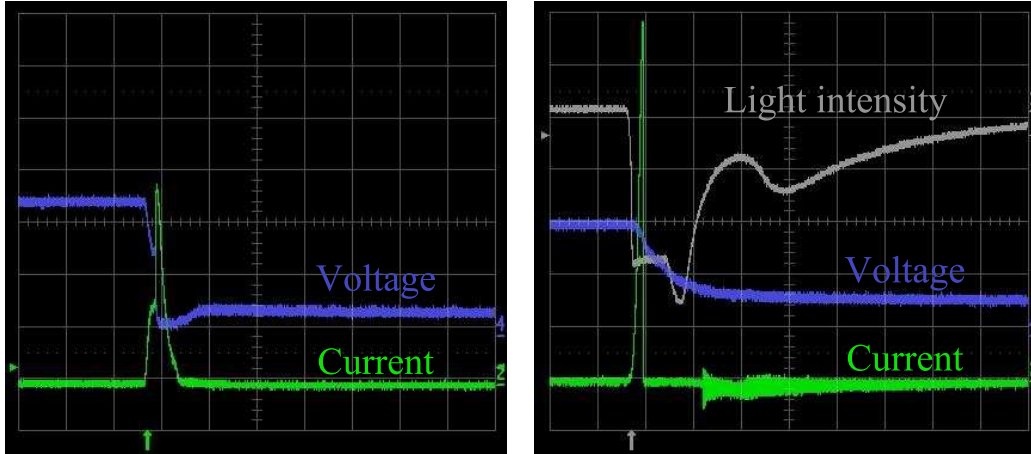
(a) Trigger on current peak for a typical gas discharge breakdown in argon at 0.239 mbar with a time scale of 0.2 ms/div

(b) Trigger on light intensity for a typical gas discharge breakdown in argon at 0.5 mbar with a time scale of 0.1 ms/div

Figure 3.11: Example breakdown measurements. Voltage in blue, current in green, light intensity in grey (inverted scale).

voltage is a static voltage [40]. As soon as the voltage ramp speed is increased there is a slight overvoltage effect in the measured breakdown voltage.

Moreover the light intensity trigger is especially used when the current peak is weak or for pulsed voltages. Pulsed voltages or fast changes of the applied voltage in the electric circuit generate current pulses in absence of breakdown. Most of the breakdown voltage versus pressure curves are obtained by following a standard procedure (figure 3.12) for each gas, geometry or different kind of electrical setup: First a pressure of about two orders of magnitude higher then the base pressure ($\sim 10^{-6}$ mbar) is set. After pressure stabilization, starting from 0 V the voltage is slowly increased until breakdown detection. Then the voltage is returned to zero and the pressure is slightly increased and so on until atmospheric pressure. To complete the breakdown voltage versus pressure curve, additional measurements are done by decreasing the pressure again and repeat the procedure for the supplementary points. The measurements (including voltage ramp) are repeated respecting a time interval of a few seconds: the time for recording data or changing pressure. When the time between two measurements is too short a memory effect could affect the results as in [41]: Metastables or remaining charged particles from previous discharge could help the ignition of the next breakdown.

Optical emission spectroscopy is a simple plasma diagnostic but can be quite difficult to interpret. An optical spectrometer (SpectraPro 275) with a 0.3 nm resolution
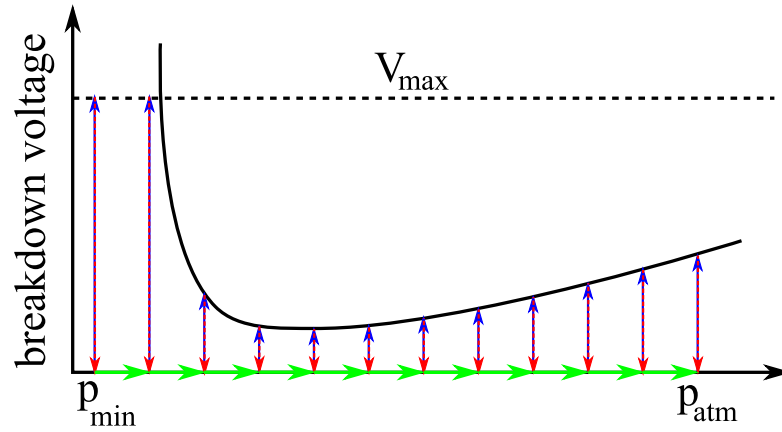
Figure 3.12: Typical breakdown voltage versus pressure measurement procedure. Blue arrows: voltage ramp for a fixed pressure, red arrows: voltage set to 0 V and green arrows: the pressure increment. The V_{max} is the generator maximum voltage.
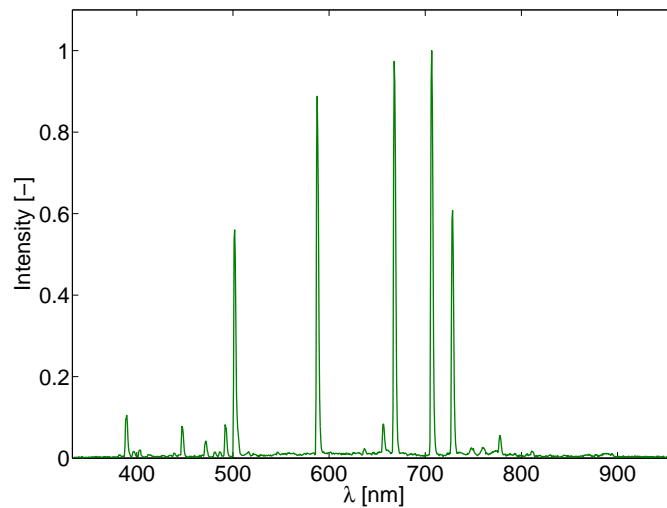

Figure 3.13: Typical result of optical emission spectroscopy. Gas discharge in helium at 0.3 mbar

equipped with a CCD camera is used to record the spectra. The data are treated with the software WinSpec [42]. For this thesis, spectral acquisition for a large range of wavelengths (from 300 nm to 950 nm) will determine the main excited or ionized states of the gas or metal vapor during the discharge, sufficient to distinguish the different types of discharge. A typical example of a recorded spectrum during a gas discharge in helium is shown in figure 3.13.

4 Experimental Results

4.1 Breakdown voltage versus pressure curve

Breakdown voltage versus pressure curves are given for a simple ring assembly and then for a slip ring assembly. The parameters which may impact on breakdown in the
follows: the effect of gas and gas pressure, dimensions and material of insulator rings, thickness of conductor ring, housing and potting on soldered points between rings and wires. Further analysis focuses on optical emission spectroscopy and their results are discussed. Finally the current-voltage characteristics show how to distinguish the different discharges after breakdown and how to avoid high current damages.

4.1.1 Simple ring assembly

Over the large pressure range investigated two kind of discharges are found: Gas and vacuum discharges. The Townsend mechanism leads to the breakdown in the gas discharges (section 2.1). On the other hand, vacuum breakdown occurs at very low pressures where ionization collisions are rare (section 2.2).

In Paschen curves for simple geometries such as parallel plates (figure 2.3), breakdown voltages are expressed according to the product of gas pressure and gap width between electrodes. Since the ring assembly does not have a well defined gap, it is not possible to express the breakdown voltages according to pressure times gap as in Paschen curves. DC breakdown voltages for the ring assembly geometry were measured for gas pressures from 10^{-4} to 10^{3} mbar in different gases and are shown in figure 4.1 as a function only of the gas pressure. In figure 4.1 two distinct mechanisms are seen over the large gas pressure range: Vacuum discharges occur at low pressures whereas gas discharges dominate at high pressures. In the transition zone between 10^{-3} and 10^{-2}

mbar both types of discharge can be present. This conclusion will be supported by optical emission spectroscopy. In the vacuum discharge range ($2 \cdot 10^{-5}$ to 10^{-3} mbar) the breakdown voltages are dispersed even for the same pressure and are independent of gas type due to the nature of vacuum discharges. The spread in measured voltages in the vacuum discharge range shows the changing surface condition dependence of breakdown. The spread in breakdown voltages could also be caused by overvoltage due to a too high voltage ramp. The so called overvoltage occurs when the voltage is increased above the breakdown voltage so fast that the measured breakdown voltage does not correspond to the breakdown voltage. Measuring the breakdown voltage by varying the pressure with a fixed voltage as [43] could avoid the overvoltage impact at this low pressure range. Above 10^{-3} mbar, gas discharge processes need to be taken into account. From 10^{-2} to 10^3 mbar the gas discharge breakdown voltage curve looks similar to a stretched Paschen curve for each gas tested. In contrast to the history dependent nature of vacuum breakdown due to the evolution of the surface condition, the gas breakdown voltage at a given pressure is highly reproducible because the ionization mechanism in the gas is nearly independent of the surface condition. This explains the strong pressure dependence of the data spread in figure 4.1. Apart from the thresholds at high pressure and low pressure, a wide pressure range from about 0.1 to 10 mbar shows almost constant breakdown voltage values. The wide flat shape has been understood with numerical simulation (see section 5.3) and finds its origin in the many possible electric field path lengths present in the ring assembly geometry. The high pressure breakdown threshold is determined by the shortest electric field line path length and the low pressure threshold by the longest one. In between it can be considered that there is a superposition of many Paschen curves issued from each different field line length. Breakdown will occur on the path which needs the less voltage. The small elbow at round 1 mbar is the consequence of a breakdown location change. Breakdown at high pressure occurs between the rings and below 1 mbar the most favorable breakdown path is between the high voltage ring and the grounded vacuum chamber wall. As the metal of the wall and the ring is not the same, the minimum breakdown voltage shifts due to a change of the secondary electron emission coefficient γ_{se} in equation (2.11). The overall shape of the breakdown voltage versus pressure curve remains the same for all tested gases. The vacuum breakdown voltage is higher than the gas breakdown voltage because the ignition processes of both kind of discharges is different and much more energy is needed to ignite a vacuum discharge than a gas discharge. Looking only at the gas discharge region of figure 4.2 the gas type has an effect on breakdown voltage as shown in figure 4.2. Nitrogen and air breakdown voltages are similar and Argon gas presents some lower breakdown voltages in accordance with gas discharge theory [6]. Each gas has different ionization energies influencing the gas breakdown processes.
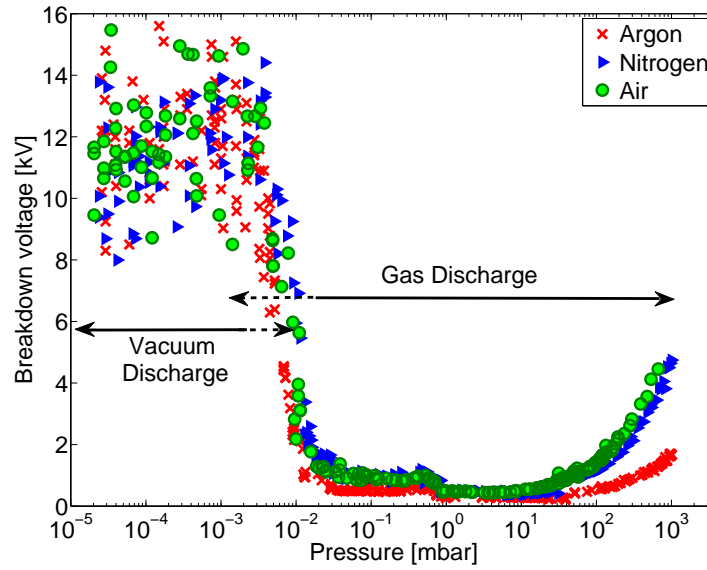
Figure 4.1: Measured DC breakdown voltages for the ring assembly from $2 \cdot 10^{-5}$ to 10^3 mbar in different gases.

The presence of metasables, abundant in argon, which have a low ionization energy play a major role in gas discharges [44]. Moreover some atoms or molecules in air such as O, O_2 and H_2O are electronegative gases [9]. This presence of electronegative gases removing by attachment free electrons, which can no more ionize, impacts on the breakdown voltage. This explains the breakdown voltage differences between the different gases in figure 4.2. There is no gas dependence in the vacuum discharge range (for pressures below 10^{-3} mbar) as expected because the gas densities are so low.

Geometry impact on DC breakdown

All following breakdown voltage versus pressure curves in this section have been done in air. Figure 4.3 highlights the importance of covering the soldered connections between the wires and the rings. The electric field line path between the soldering point and a ring must be considered as an additional possible breakdown path. To avoid this, an epoxy structural adhesive is used as potting to limit the breakdown only between the rings. The shortest breakdown path will therefore be the distance between to conductor rings.

If the conductor thickness is increased (with the same insulator dimension), the shortest and longest electric field line path remain the same and no changes are observed
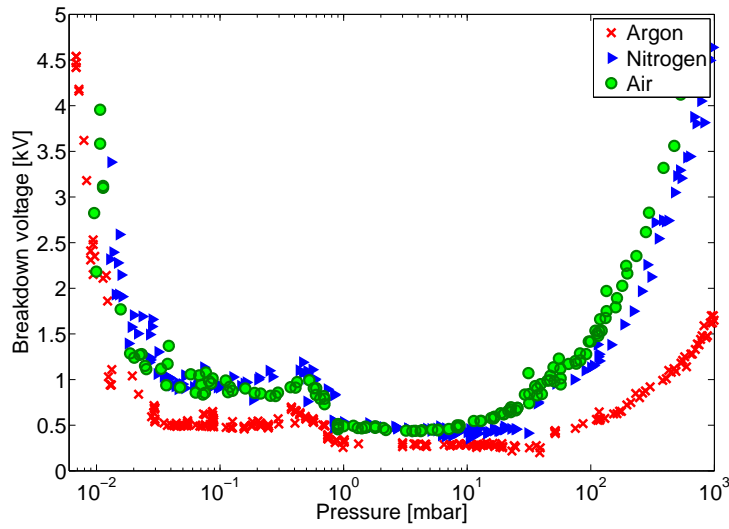
Figure 4.2: Measured DC breakdown voltages for the ring assembly from $6 \cdot 10^{-2}$ to 10^3 mbar in different gases. Rescaling of figure 4.1
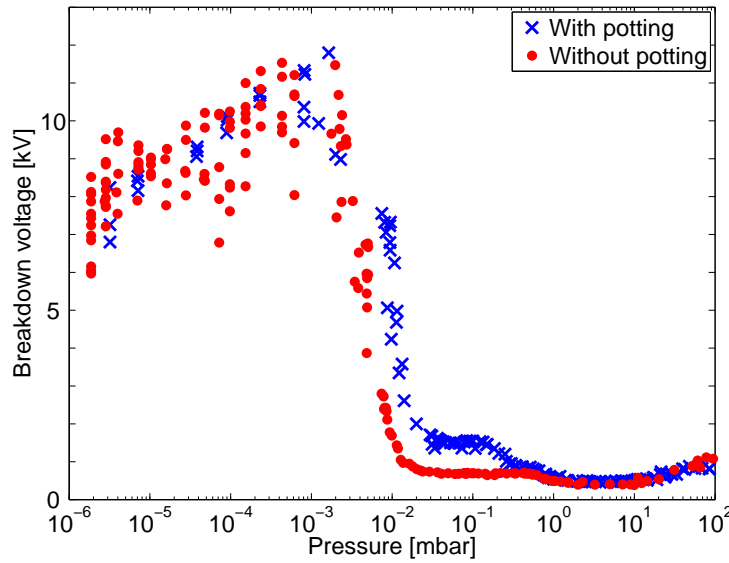

Figure 4.3: Measured DC breakdown voltages for the ring assembly. The geometry with the soldered connections between the metal rings and the wires covered by potting shows higher breakdown voltages than the geometry without potting due to less available breakdown paths.
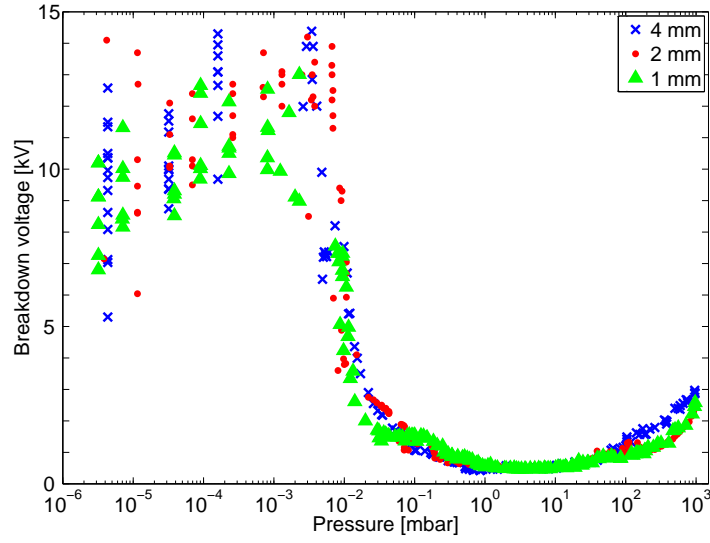
Figure 4.4: Measured DC breakdown voltages for the ring assembly. The change of conductor ring thickness (no changes in internal and external diameter) leads to no effect on breakdown voltage.

in the breakdown voltage versus pressure curve. This result is presented in figure 4.4. Nevertheless if the external diameter of the insulator ring is increased, then the shortest path is blocked by the external barrier. This impacts directly with a breakdown voltage increase for high pressure and vacuum arcs discharges as shown in figure 4.5. Instead of changing the external diameter of the insulator, the thickness of the insulator rings could also affect the breakdown paths availabilities (conductor and insulators external diameter is the same). In figure 4.6 the insulator rings are 1 mm respectively 4 mm thick. Obviously again for high pressure and vacuum arc discharges, breakdown occurs easier in the first configuration. The ring insulator thickness determines the shortest distance between the conductor rings. If breakdown voltage is expressed versus pressure times the shortest distance between the conducting rings as in figure 4.7, the curves are superposed for $pd > 10^{-1}$ mbar mm like Paschen curves (V_{Bd} versus pd) in parallel plate configuration with different gaps. This illustrates the validity of the Paschen theory for this region of pd. Other processes such as vacuum breakdown need to be taken into account for $pd < 10^{-1}$ mbar mm.

Due to the grounded vacuum chamber, the longest breakdown path is the distance from the anode to the chamber walls (see figure 3.6). If the ring assembly is placed in a grounded tube (housing) as in figure 4.8 then the longest electric field line paths is reduced impacting on the left hand side breakdown voltage threshold as in figure 4.9. The smallest tube shows a voltage drop between 10^{-1} mbar and 10^{-2} mbar due to the
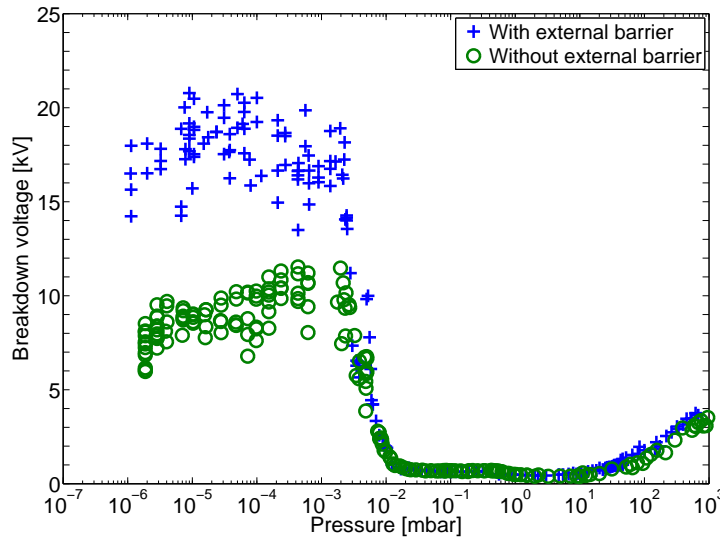
Figure 4.5: Measured DC breakdown voltages for the ring assembly. The insulator external barrier increases breakdown voltage only for short electric field line path regions (vacuum arcs and high pressure discharges), because it disables the shortest breakdown path of the geometry.
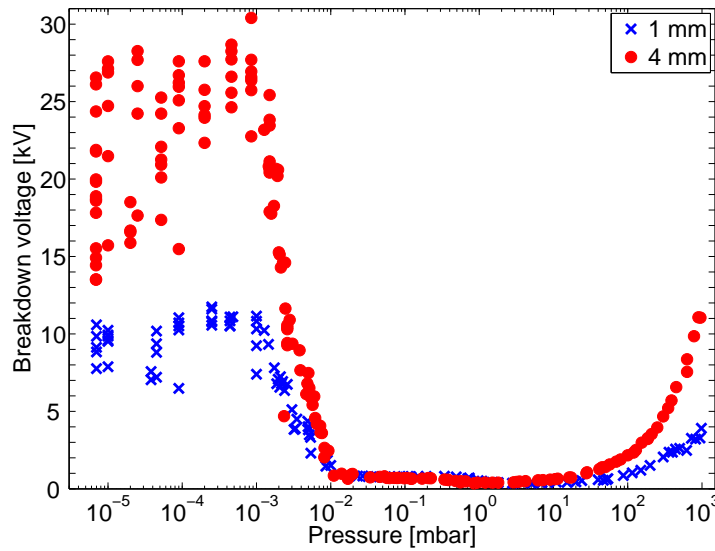

Figure 4.6: Measured DC breakdown voltages for the ring assembly. The increase of insulator ring thickness (no changes in internal and external diameter) leads to an increase of breakdown voltage in high pressure gas discharge as well in vacuum discharge regions where breakdown occurs along the shortest electric filed line.
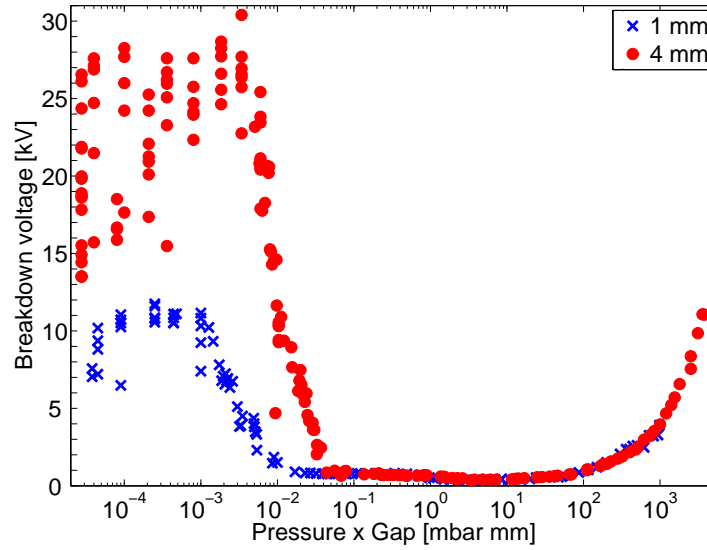
Figure 4.7: Measured DC breakdown voltages for the ring assembly versus pressure times the shortest available breakdown path determined by the insulator thickness.

opening at the top of the housing tube. The housing (grounded tube around the ring assembly) limits the path length availability and therefore increases the breakdown voltage. The effect increases with the decrease of the tube internal diameter.

The type of insulator has been tested and the DC breakdown voltage versus pressure remains the same. The material of the insulator does not play any role in breakdown in our measurements. Nevertheless the breakthrough strength has to be sufficient to support the high voltage application. Examples of a dielectric failure are illustrated in section 4.5.

AC or Pulse generator

Up till now DC voltage has been applied to the ring assembly. Breakdown for different kinds of voltage waveforms such as pulsed or sinusoidal have been studied over many years. Contrary to DC voltage, both electrodes can be conditioned with AC because both polarities are applied on the setup [45]. The breakdown voltage in the vacuum discharge range could therefore be slightly higher for AC voltage than for DC voltage [46]. Our AC voltage generator could not reach high enough voltages to ignite vacuum breakdown for the tested geometry. We will therefore focus only on gas breakdown. The polarity (negative and positive DC voltage) and AC voltage (100 Hz) have been investigated. In figure 4.10 negative and positive breakdown voltage show the same
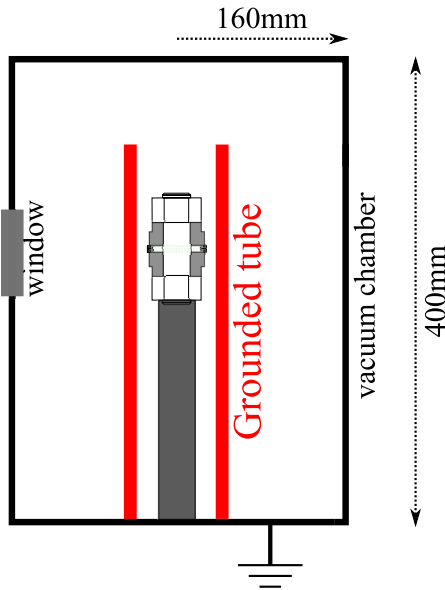
Figure 4.8: Schematic of a ring assembly in a vacuum chamber. A grounded tube surrounds the ring assembly (housing).
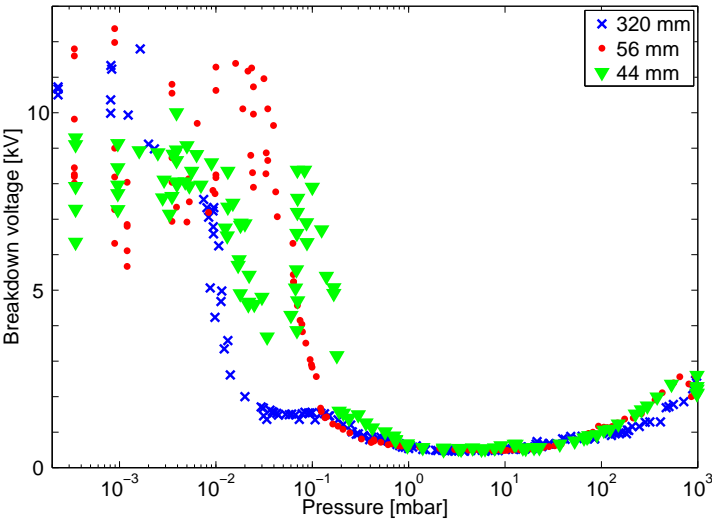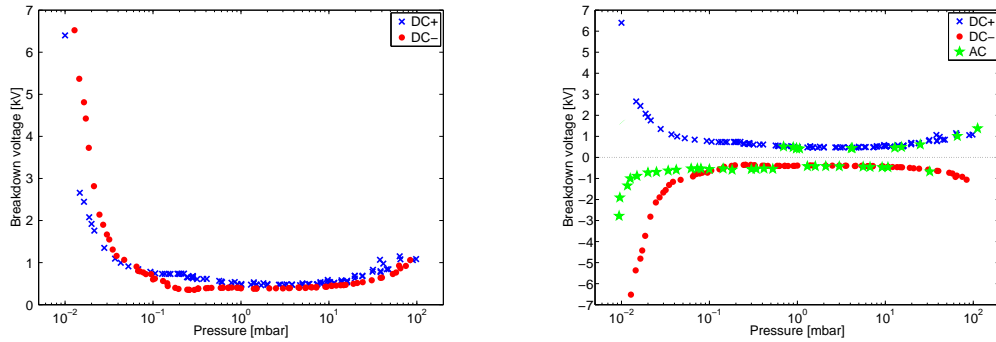

Figure 4.9: Measured DC breakdown voltages for the ring assembly (external diameter of 38 mm) placed in a grounded tube (open at the top) of various internal diameters.

(a) Absolute breakdown voltages for positive and negative DC voltage

(b) DC and AC 100 Hz voltage

Figure 4.10: Breakdown voltage versus pressure.

shape according to pressure. The grounded vacuum chamber surface, much bigger than the ring surface, is considered as negative (positive) when positive (negative) voltage is applied on the middle ring. The absolute DC breakdown voltage of negative polarity is slightly lower than positive polarity due to the positive and negative surface asymmetry changing the impact area of the surface processes such as secondary electron emission by ion impact or particle losses on the surfaces. Nevertheless below 0.1 mbar the negative breakdown voltage is higher than the positive one. This effect is attributed to the change of secondary electron emission coefficient. At low pressure breakdown occurs in the long gaps, here therefore between the middle ring and the vacuum chamber wall. Changing the polarity will change the target area of the ions, i.e. the secondary emission rate by ion impact. Breakdown below 0.1 mbar is easier to obtain with AC than with DC as shown in figure 4.10(b) because the oscillating field reduces the particle losses on the surface limiting the drift. For higher pressures the breakdown voltages are very similar to DC because the AC frequency is so low that it could be considered as a mix of negative and positive DC. AC breakdown can therefore ignite either at positive voltage or at negative voltage and chooses the easiest breakdown possibility.

As described in section 2.1.1, breakdown cannot only develop with electrons but also needs ions which release electron by secondary emission. Most of the ions are created near the anode and travel towards the cathode. As the electrons are faster the ion drift velocity determines the minimum amount of time necessary to cross the gap [11]. Considering a pulsed voltage, the breakdown development process is continuously interrupted. For breakdown it is necessary to keep some particles from a pulse until the next pulse. Short pulses at low frequencies need higher voltage to accelerate the charged particles through the gap and initiate breakdown. Figure 4.11 supports this
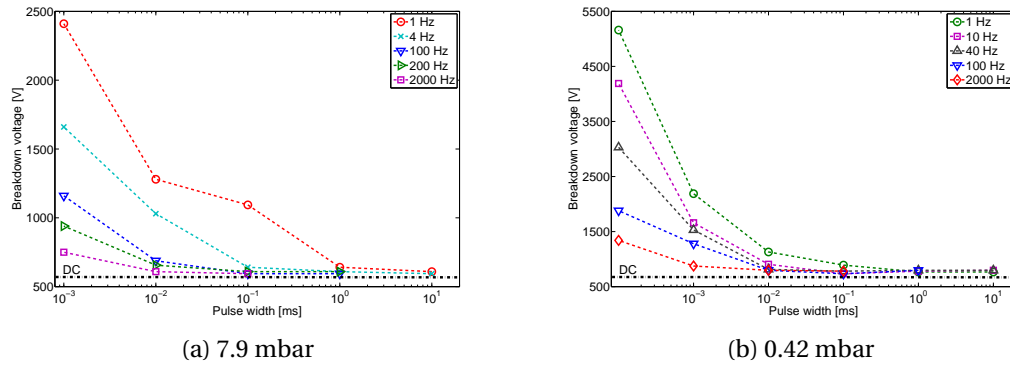
(a) 7.9 mbar   (b) 0.42 mbar

Figure 4.11: Breakdown voltage versus pulse width from pulse generator for various pulse frequencies. The dashed horizontal line represent DC voltage breakdown.

theory: The breakdown voltage clearly increases as the frequency or the pulse width decreases. If the frequency is high enough and the pulse width long enough then breakdown with pulsed voltage looks similar to DC breakdown. It is hard to define at which frequency and pulse width the breakdown voltage could be considered same as DC. Moreover the statistical nature of breakdown starts to play a role with this kind of pulsed voltage. If the applied voltage reaches the breakdown voltage then breakdown does not occur before a delay called breakdown delay time. This delay is the sum of the statistical time delay (from the application of voltage to the appearance of a free electron that may produce breakdown) and the formative time (from this last moment to the collapse of the applied voltage and occurrence of a self-sustained current) [47]. The breakdown time delay has a value around 1 ms but depends on the electron yield and the relaxation time which is the time necessary for a system to return from a perturbed state into equilibrium. The pulsed voltage with pulse width shorter than 1 ms have therefore less probability to ignite a discharge leading to the need of more and more voltage for breakdown as the pulse width decreases.

4.1.2 Slip ring geometry from industry and conclusions

The breakdown voltage of the real slip ring assembly is compared with the simple ring assembly geometry in figure 4.12. The dimension of the conductor and insulator rings are in both cases 1 mm thick and the external diameter of the insulator rings is 2 mm bigger than the conductor diameter (external barrier). The results show that the simplified geometry represents quite well the complete slip ring assembly over the full tested pressure range and validates the testing in a simpler geometry. Both vacuum arcs and gas discharge zones are present as well the constant minimum breakdown voltage in the middle range pressures. The transition between vacuum and gas discharge (low pressure threshold) occurs at a slightly higher pressure for the slip ring assembly than for the simple ring assembly. The biggest distance between the conductors and the wall chamber determines this threshold and is smaller for the slip ring assembly because the diameter of the conductor ring of the slip ring assembly is bigger than the ones of the simple ring assembly.

To represent the most realistic situation the solar cell simulator is connected to the slip ring assembly. Figure 4.13 shows similar voltages for DC voltage and the solar cell simulator (with shadow diode: square voltage waveform) on two different configurations (high voltage on P15 and P17 in figure 3.4). In agreement with the previous pulse generator results (frequency and pulse width investigation in section 4.1.1), no breakdown occurred using the solar cell simulator without shadow diode (maximum peak voltage is 1 kV) because the voltage peak was limited to only 1 kV and the pulse was to short. In figure 4.13, the smallest and the longest breakdown path are the same for both configurations determining the low and high pressure threshold. The intermediate breakdown possibilities do not play any role in the gas discharge thresholds. Moreover the DC voltage and solar cell simulator comparison suggests quite similar breakdown voltages. Nevertheless the breakdown voltage is slightly higher for the simulator due to its squared waveform interrupting periodically the ignition processes. As the breakdown time is very short, the pulsed simulated voltage signal looks like DC according to previous results on pulse width and frequencies (section 4.1.1). In figure 4.14, breakdown voltage from solar cell simulator with shadow diode in a rotating slip ring, i.e. slipping brushes on the rings at 1 rpm is compared to static measurements. There is no significant difference in breakdown voltage because the electric field lines as well as the pressure remains the same. Moreover the rotation speed is far below the one needed for a significant heat up of the contact due to friction.

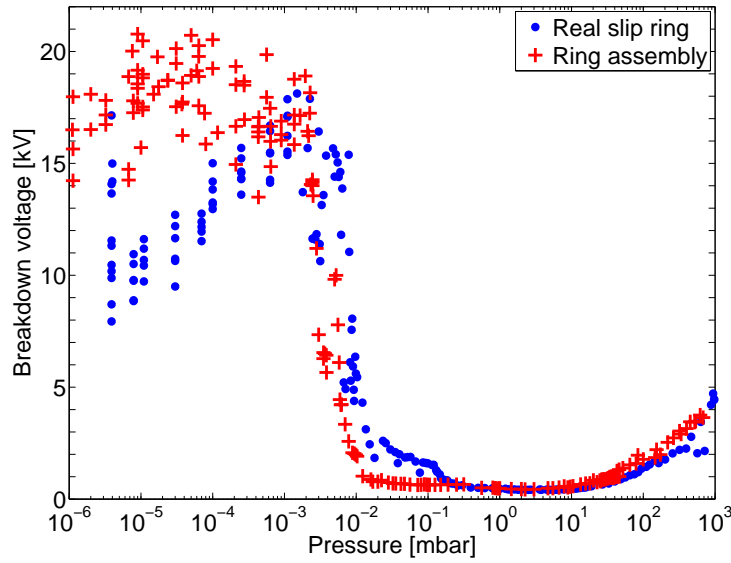Finally a general breakdown curve could be established for complex geometries as

Figure 4.12: Measured DC breakdown voltages for the a complete slip ring assembly as presented in figure 3.3 provided by industry in air compared to a simple ring assembly.

in figure 4.15. A safe zone is defined as the region where no breakdown occurs based on previous results. Obviously below a $5 \cdot 10^{-3}$ mbar the working voltage could be increases because vacuum discharges need higher voltages for breakdown than gas discharges. The lowest breakdown voltage is located in the gas discharge region and defined by the minimum breakdown voltage depending on each gas and secondary emission coefficient (see equation (2.11)). Once a breakdown is initialized, the safety of the device is no more guaranteed and any damages could be possible as presented in section 4.5. In simple words: No breakdown, no failure! Nevertheless it is possible to have non destructive discharges as presented in figure 4.16 in the risk zone if the current is sufficiently limited by the external circuit.
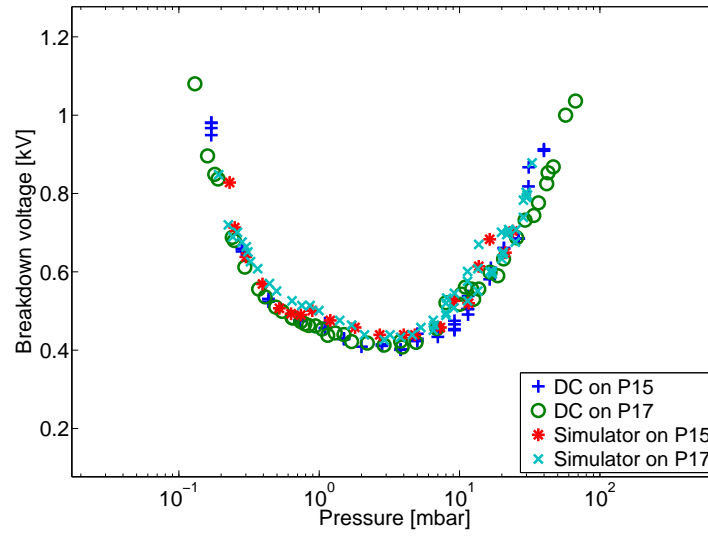
Figure 4.13: Measured breakdown voltages for complete slip ring assembly in air. Comparison between different high voltage connection (P15 and P17) and between DC voltage and solar cell simulator.
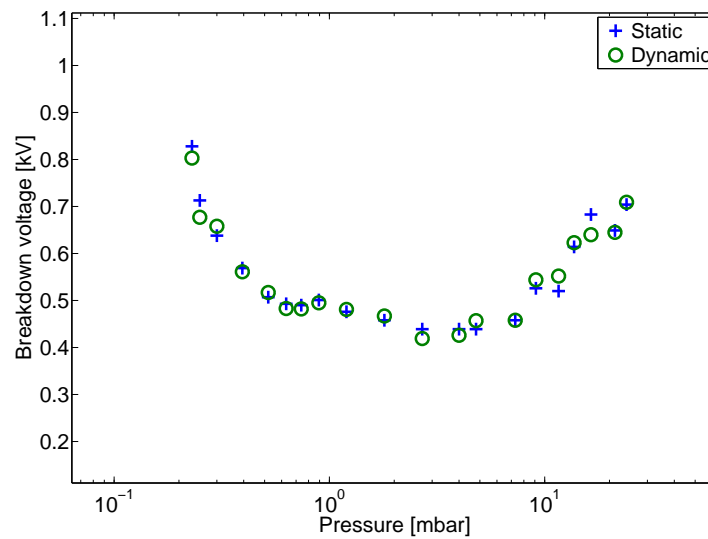

Figure 4.14: Measured breakdown voltages provided by solar cell simulator applied to a complete slip ring assembly in air. Rotation (1 rpm have no impact on breakdown voltage measurements.
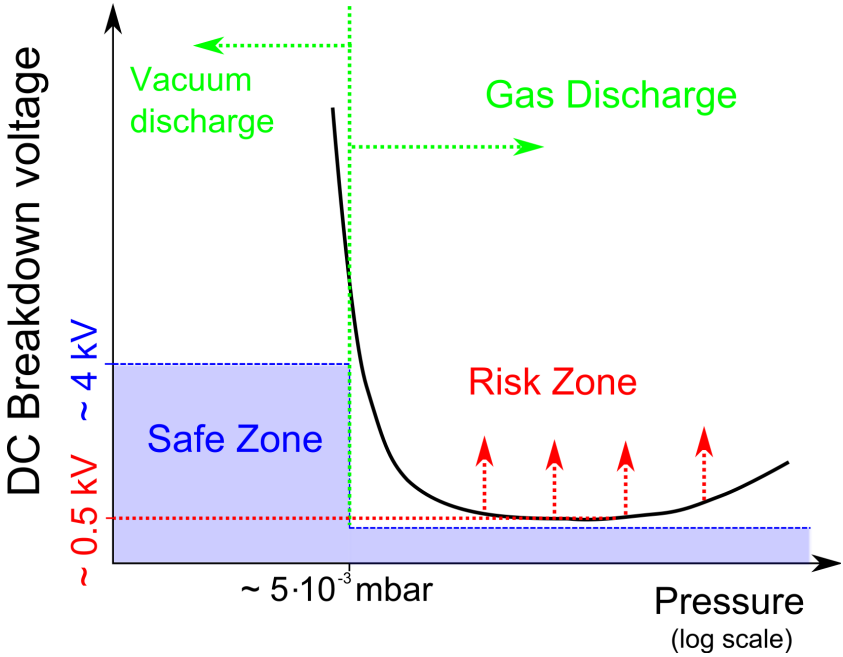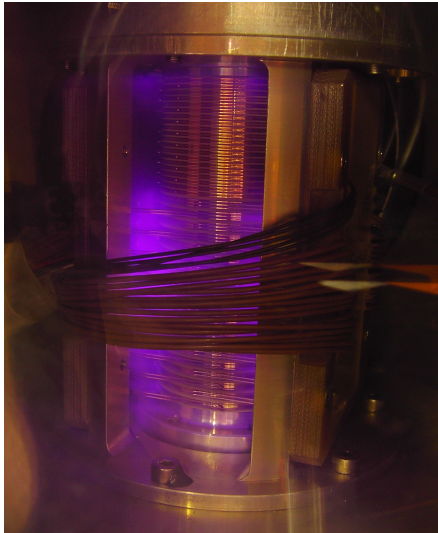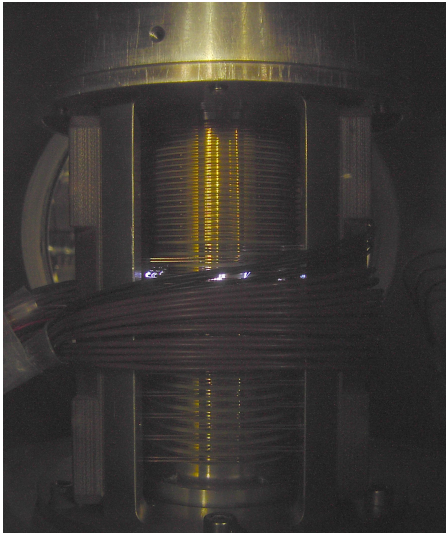
Figure 4.15: General worst case schematic for a breakdown voltage versus pressure curve. The safe zone is defined where no breakdown occurs.

(a) Corona discharge   (b) High pressure arcing

Figure 4.16: Two different kind of non destructive discharges (current limited) in the slip ring assembly.
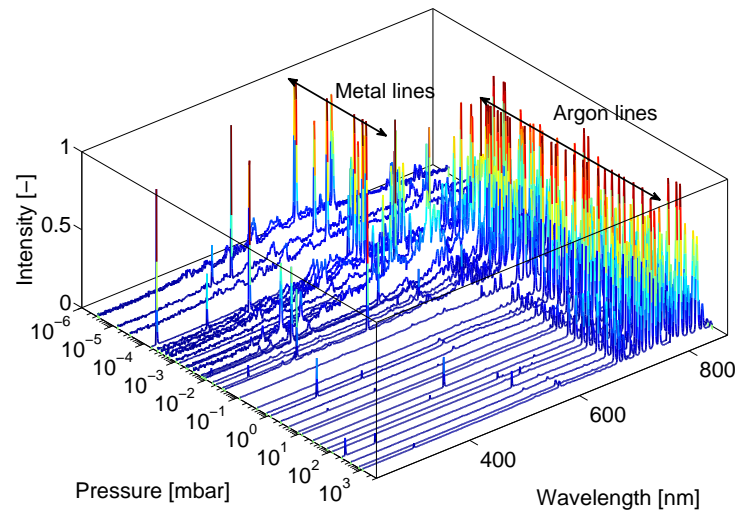
Figure 4.17: Optical emission spectroscopy using argon gas. Metal lines are observed for pressures below 10^{-3} mbar (vacuum discharge) whereas argon lines occur for pressures above 10^{-2} mbar (gas discharge). For clarity, each spectrum is normalized to its dominant line.

4.2 Optical emission spectroscopy

Different processes are involved for vacuum and gas discharges leading to different optical emission spectra. Figure 4.17 shows the result of a combination of optical spectra taken at different pressures in argon. Each spectrum is normalized to its maximum line intensity. The optical data acquisition can take several seconds in particular for discharges with low light intensities. Optical emission spectroscopy can be used to distinguish gas discharges from vacuum ones. Optical spectroscopy in argon is easier to interpret than air because argon is a monatomic gas. In a vacuum discharge, metal vapor from the electrodes provides the medium for the discharge development. Only metal lines are present at low gas pressures in the vacuum discharge zone ($p < 10^{-3}$ mbar in figure 4.17). The dominant metal spectral lines based on atomic spectra line database [48] are listed below:

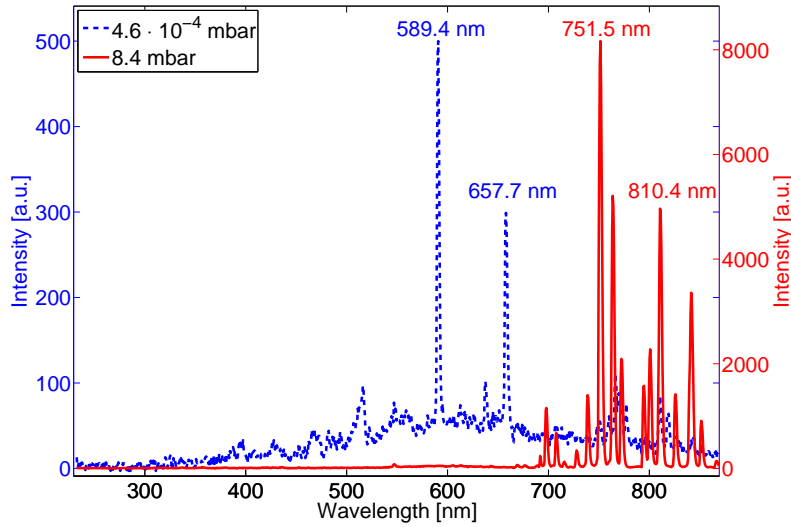| Copper	Zinc
515.3 nm	481.0 nm
657.7 nm	492.4 nm
766.4 nm	589.4 nm
809.2 nm	636.2 nm

Figure 4.18: Optical emission spectra in argon gas: In low gas pressures the dominant emission lines are copper and zinc due to the vacuum discharge processes. Moreover the spectrum has a weak background of unresolved lines due to the multiple but weak metal emission lines. At high gas pressure argon emission lines are dominant.

The main composites of brass are copper ($\sim$ 57%) and zinc ($\sim$ 36%) and the metallic optical emission lines show the presence of these metals in the discharge. In the transition region, both metal and gas lines (argon lines) can be observed. For pressures above 10^{-2} mbar the presence of only gas lines confirms the gas discharge domination. The main argon lines are based on atomic spectra line database [48]:

Argon
751.5 nm
763.5 nm
810.3 nm
842.1 nm

A direct comparison of a gas discharge and a vacuum discharge spectra in figure 4.18 illustrates well the differences between the two distinct types of discharges.

In figure 4.19 two argon emission lines (763.5 nm and 842.1 nm and two metal emission lines (589.2 nm and 657.7 nm) intensities have been picked out for each spectrum measured over the large pressure range. These lines intensities are normalized to the maximum of each relative spectrum and are plotted versus pressure. Only metal lines
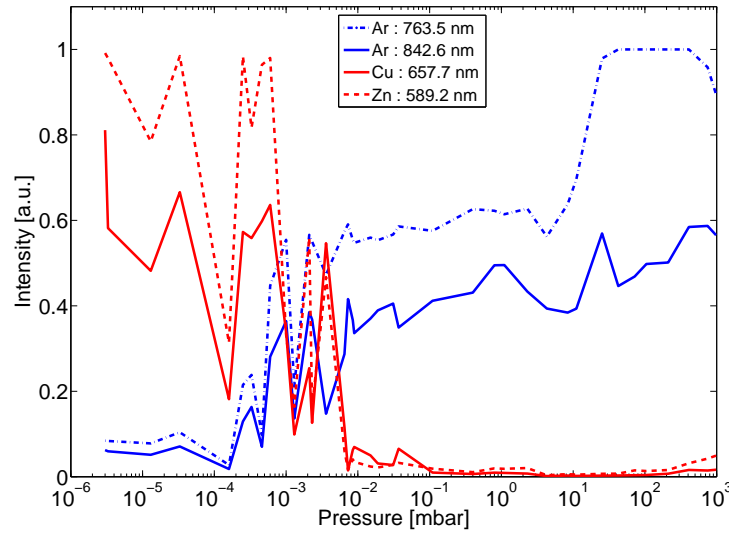
Figure 4.19: Optical emission intensities normalized to maximum line in argon gas. Copper lines are observed for pressures below 10^{-3} mbar (vacuum discharge) whereas argon lines occur for pressures above 10^{-2} mbar (gas discharge).

are present at low pressure in the vacuum discharge zone spectrum ($p < 10^{-3}$ mbar) and only gas lines in the gas discharge zone ($p > 10^{-2}$ mbar). The transition zone presents both types of emission lines. For pressure below 10^{-3} mbar argon lines are nearly zero. This is another way to highlight the difference between vacuum and gas discharges.

The optical emission emission spectroscopy results in air (figure 4.20) are similar to argon gas, but more complex to interpret because it is composed of several gases (mostly nitrogen, oxygen). Moreover, different kinds of gas discharges could be distinguished based on optical observations presented in the next section: Arcs, negative corona, positive corona and vacuum arcs. An optical spectrum of each kind of discharge is presented in figure 4.21 and the N_2 lines are interpreted based on [49]. N_2 second positive system and N_2 first positive system are groups of specific emission lines characterizing each N_2 excited state decaying into lower states illustrated in figure 4.21(b) and (c):

- (a) shows an example of an arc discharge. The energies involved are so high that the nitrogen molecule is dissociated. The dominant emission lines in this spectra are nitrogen atomic lines (746.8 nm, 776 nm, 843 nm and 868 nm [48]).

- In (b) the N_2 second positive system dominates, characterizing the negative

corona.

- (c), where the N_2 first positive system dominates, and (b) show the difference between the positive and negative corona due to the additional photo processes during a positive corona.

- Because vacuum discharge processes are not dependent on gas, the vacuum arc spectrum in (d) is similar the vacuum arc spectrum in figure 4.18 performed in argon gas.

- The transition between vacuum and gas discharges is still visible in (e). The spectrum looks like the one in (d) with additional N_2 first positive emission lines.
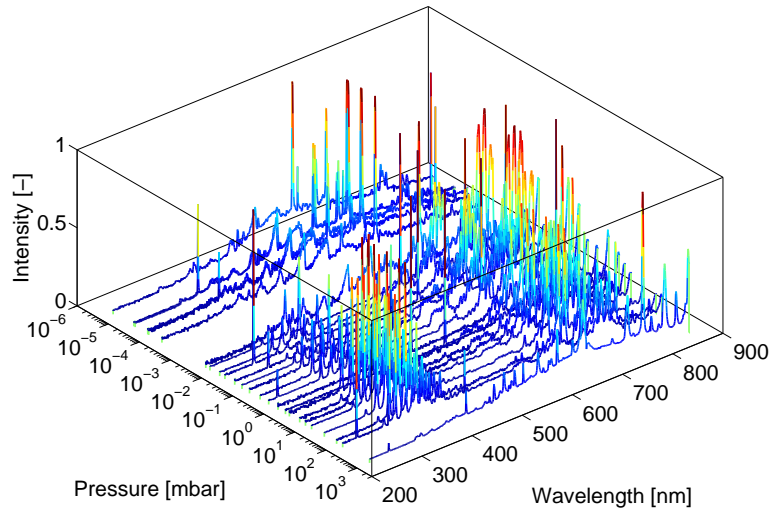

Figure 4.20: Optical emission spectroscopy in air: Metal lines below 10^{-3} mbar, a transition between 10^{-3} mbar and 10^{-2} mbar and above 10^{-2} mbar only gas lines are visible. Many emission lines are present above 10^{-3} mbar characterizing the different kinds of discharge in air. Single spectra are shown in figure 4.21

4.3 Visual observations

The changes in optical emission spectrum according to the type of discharge are supported by observations made through the window of the vacuum chamber: The discharge is observed to occur between the rings in the form of an arc (figure 4.23) at high pressures (above ~ 100 mbar) in air. As the pressure is decreased the arc becomes

(a) Arc

(b) Negative corona

(c) Positive corona

(d) Vacuum arcs

(e) Vacuum arcs spectrum with the presence of N_2 first positive
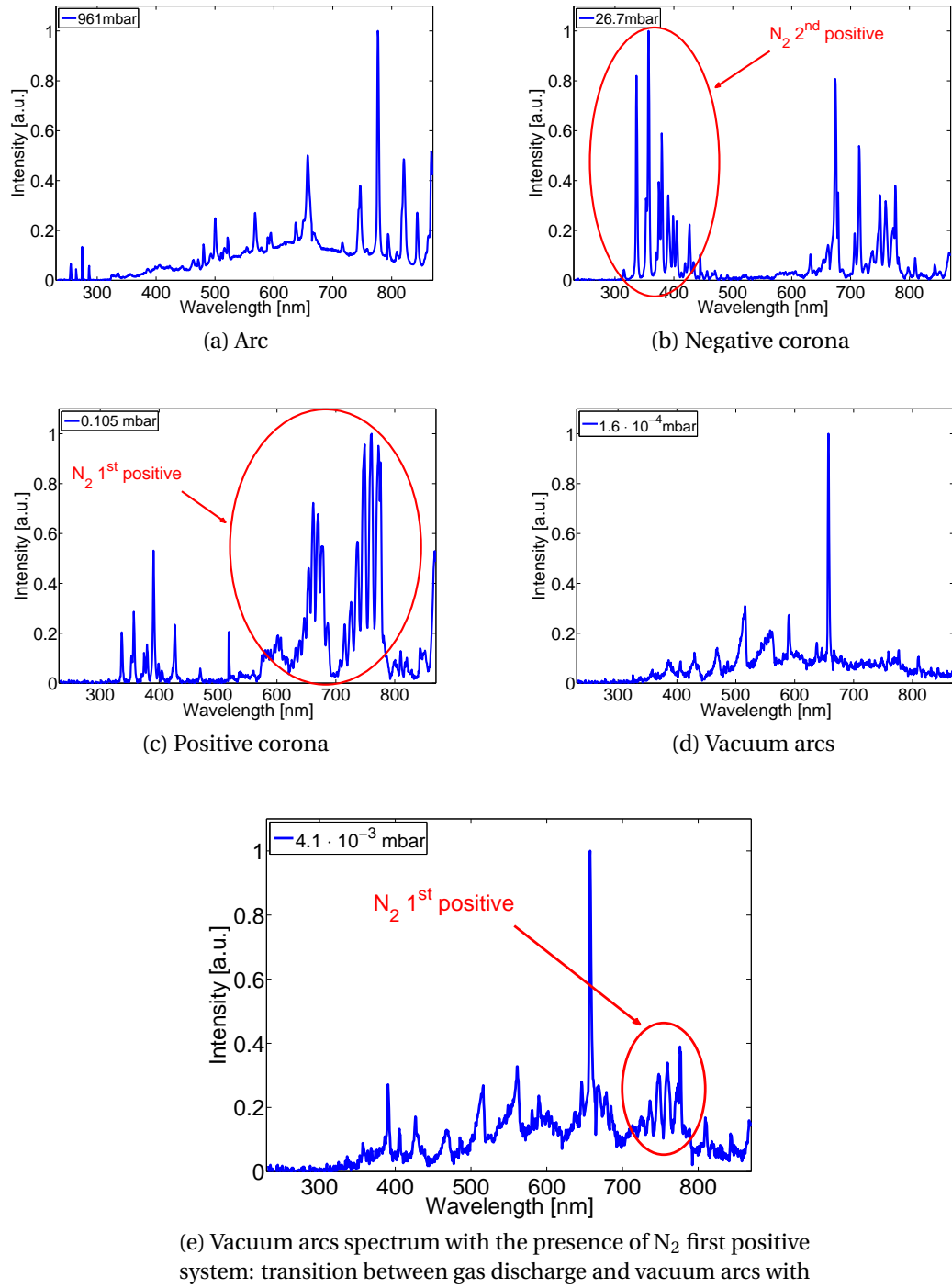system: transition between gas discharge and vacuum arcs with

Figure 4.21: Optical emission spectra for different kinds of discharges in air.
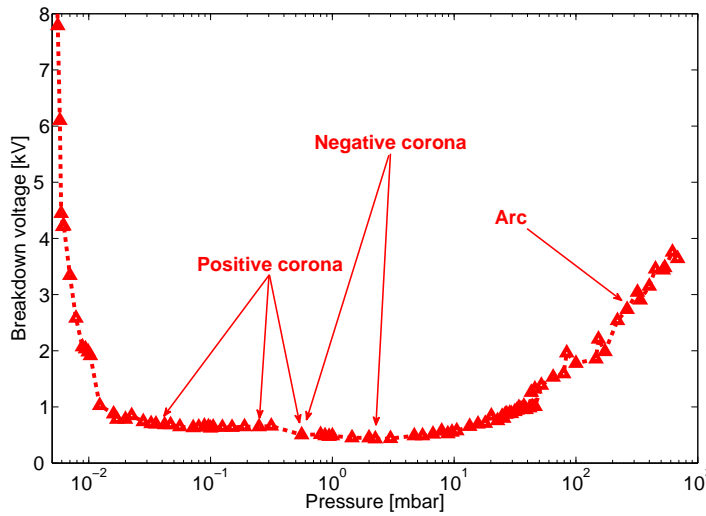
Figure 4.22: Breakdown voltage versus pressure curve with location of the different kinds of gas discharges in air presented in figure 4.23-figure 4.28: Arcs, negative corona, positive corona.

more diffuse and gradually covers the top and bottom grounded rings (figure 4.24). A transition occurs at about 1 mbar: the high voltage ring light intensity dominates instead of the grounded rings (figure 4.25). Then the negative corona disappears completely (figure 4.26), becomes diffuse and fills the full chamber volume as the pressure decreases (figure 4.28). The negative and positive corona also have different colors, purple and respectively pink in air. This change in color is visible in the optical emission spectroscopy due to the different discharge mechanisms involved. The corona occurs only where the field is enhanced due to the inhomogeneity. Looking at the calculated field lines from figure 5.17 and the corona pictures from figure 4.25 or figure 4.27 supports this fact. At 10^{-2} mbar, vacuum arcs between the rings begin and below 10^{-3} mbar gas discharges are absent as in figure 4.29. At high currents the discharges become more intense as in figure 4.27.

If the volume inside the ring assembly held by the PTFE holder is not filled, it is theoretically possible to have a non visible breakdown hidden inside the ring assembly. Most of the observations indicated that breakdown occurs externally between the rings or the rings and the vacuum chamber. Nevertheless it is not possible to affirm that no plasma was inside the ring assembly. Based on the calculated electric field line inside the ring assembly (figure 5.17), there are very limited paths going from the anode to the cathode for the electron without encountering a piece of insulator. On the assumption that enough charges could accumulate on the insulator surface and
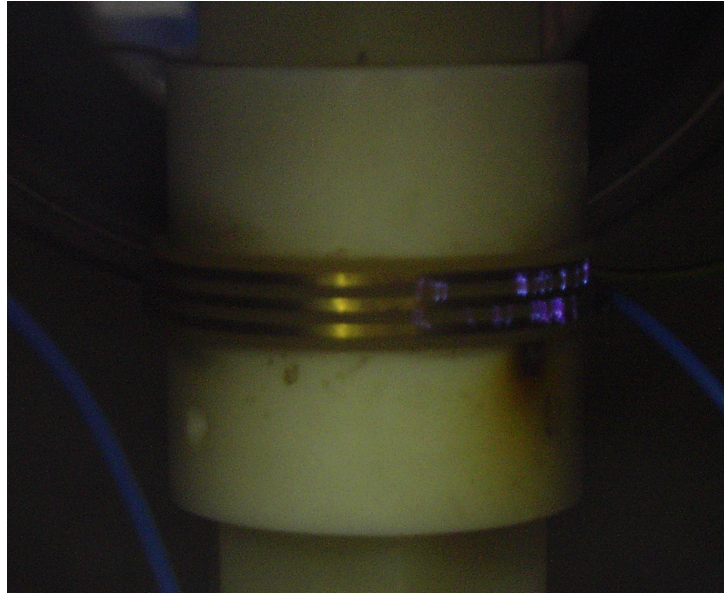
Figure 4.23: Small burning arcs with low current at 280 mbar in a ring assembly geometry.

to modify the electric field, electrons could also travel freely from one electrode to another and possibly initiate breakdown. However, in our case the densities are so low that surface charge accumulation should not significantly modify the electric field. Obviously vacuum arcs and arcs could occur internally if there is not internal barrier formed by the insulator (internal insulator ring diameter same as conductor one) as in the setup used in figure 4.37.

4.4   Current-voltage characteristics

In the previous chapters several kinds of discharges have been highlighted. This following current-voltage investigation presents the electrical parameters which impact on the discharge such as the elements in the external electrical circuit [50]. It is important for satellite applications to know if discharges could damage the material or simply produce power losses. A high voltage generator could be used here for discharge current investigations instead of the non-destructive high voltage insulation tester. For a suitable current comparison, it is necessary to keep the same external circuit at least for the same experiment. External resistances where add between the generator and the high voltage feed through to limit the current as schematically shown in figure 4.30(a). Figure 4.31 shows breakdown voltage versus peak-to-peak current for different pressures. For a constant pressure, the breakdown voltage should be independent of
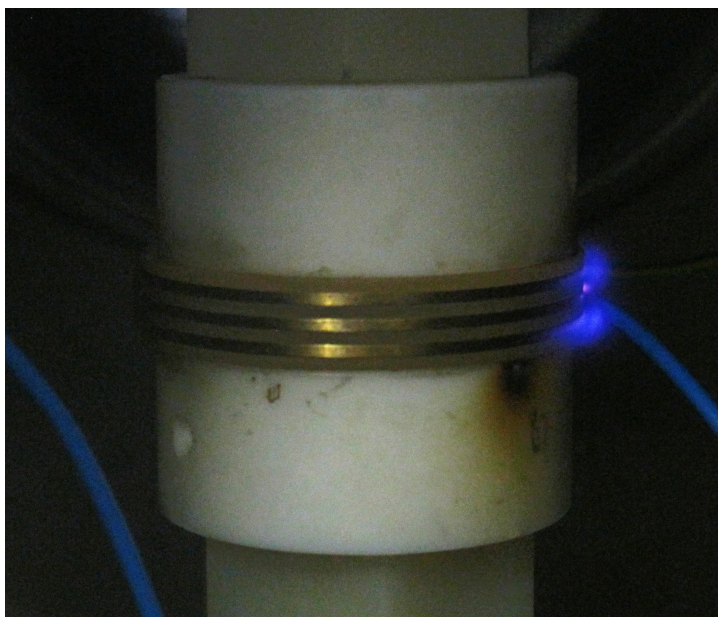
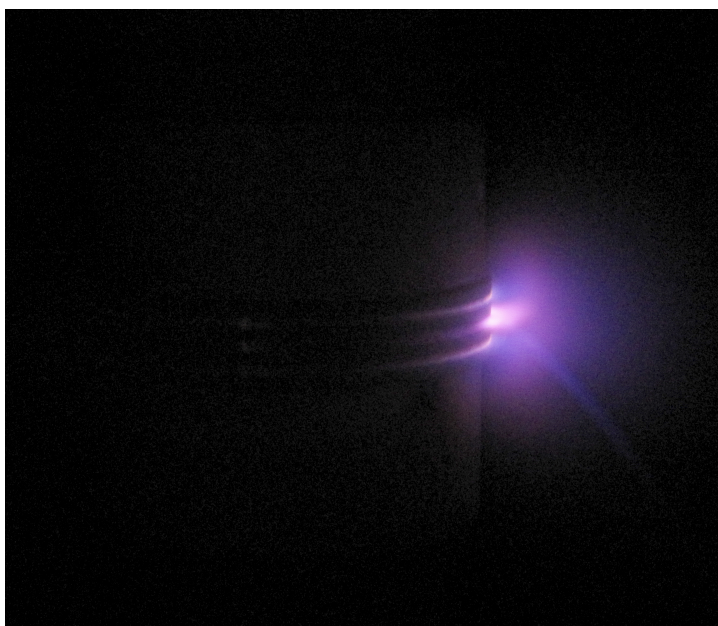Figure 4.24: Negative corona with low current at 2.3 mbar in a ring assembly geometry.

Figure 4.25: Positive corona with low current at 0.6 mbar in a ring assembly geometry. There is still some remaining parts of the negative corona.
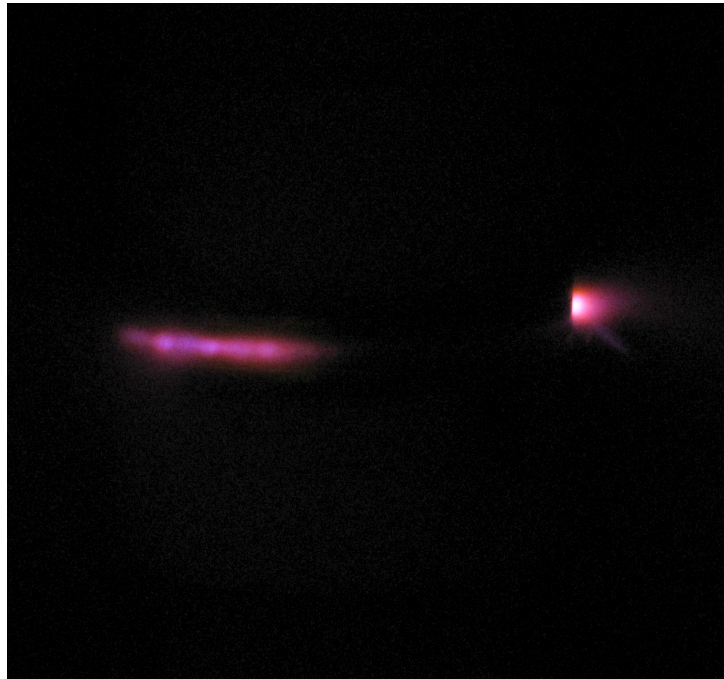
Figure 4.26: Positive corona with low current at 0.3 mbar in a ring assembly geometry.
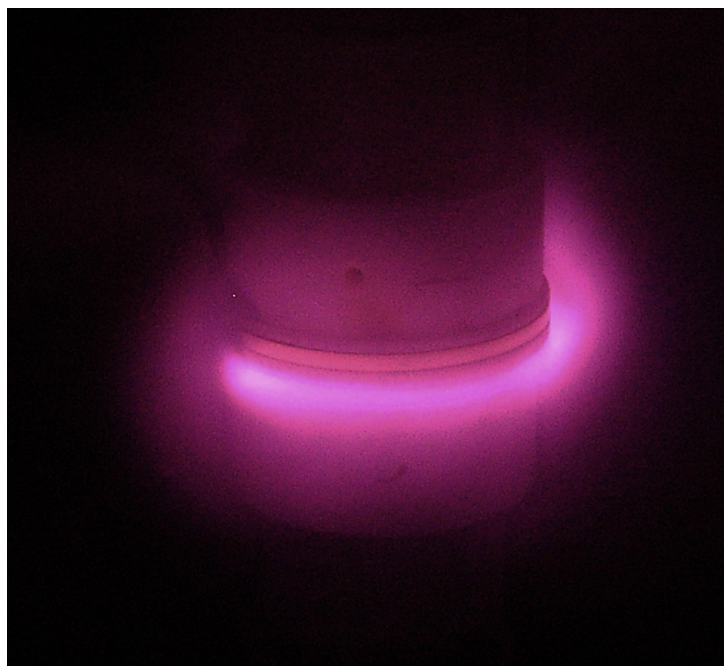

Figure 4.27: Positive corona at 0.3 mbar in a ring assembly geometry. The discharge conditions are exactly the same as in figure 4.26 except the current which is less limited.
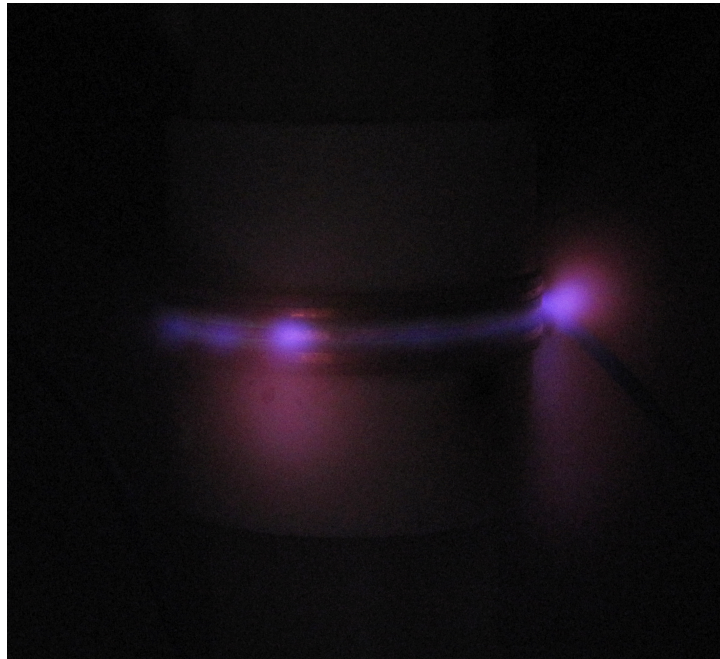
Figure 4.28: Positive corona with low current at 0.04 mbar in a ring assembly geometry becomes more and more diffuse. There are still no vacuum arcs.
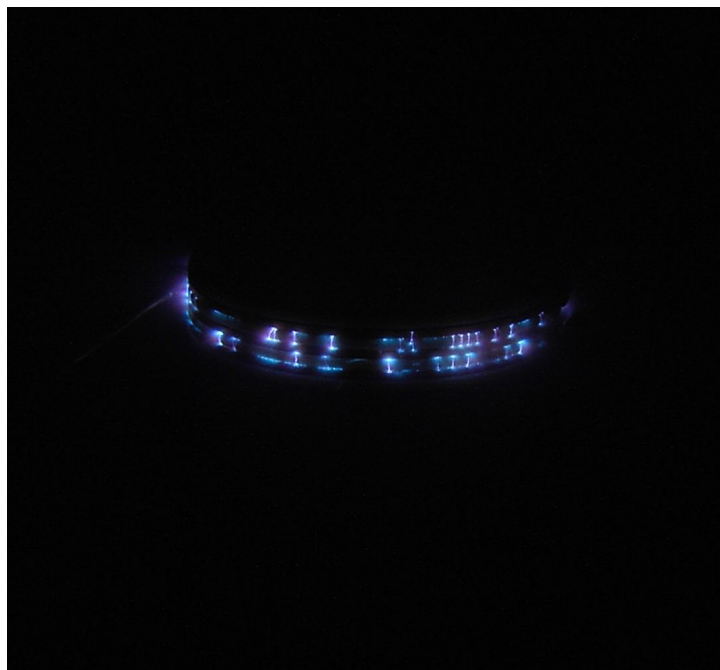

Figure 4.29: Vacuum arcs at $7.3 \, 10^{-6}$ mbar in a ring assembly geometry.

the external circuit. In figure 4.32 the breakdown voltage is the same whatever the external resistance but the current is strongly reduced because increasing the resistance limits the charged particle flow development during breakdown. Nevertheless according to the load line curve (figure 2.5), a really large resistance will limit the breakdown formation and probably increases the breakdown voltage. The effect is similar with an external capacitance (see the electric schematic in figure 4.30(b)) in parallel with the electrode setup in figure 4.33: Breakdown voltage (provided in this case by the non-destructive high voltage insulation tester) remains the same again. The current is strongly increased when the 40 nF capacitance discharges through the ring electrodes compared to the limited current provided by the high voltage tester. Finally the external circuit is not influencing the breakdown voltage but only the current intensity or waveform which determines the form of the discharge and the possibility to damage the experimental setup. This shows the importance of the parasitic capacitance or external circuit.

Observing the maximum current involved during breakdown voltage measurements over a large pressure range as in figure 4.34 is a tool to distinguish the different kinds of discharges. In accordance with optical spectroscopy and observations, the arcs and vacuum arcs generate obviously high currents whereas glow discharge only low ones. Figure 4.35 illustrating the current versus the voltage for various gas pressures could represent a danger scale. The right top corner is the region where the most energetic breakdowns occur with possible failures whereas the left bottom one groups the low energy breakdowns. Vacuum arcs ignite at such low pressures that they need to generate the discharge medium from the electrodes. This process requires a lot of current and voltage. Then gas breakdowns take place when the pressure is increased. The voltage necessary for breakdown then decreases because less energy is needed to accelerate the electron when the mean free path is shorter (more collisions). The current is also decreased due to the gas density increase slowing down the particles. For pressures above 0.1 mbar the tendency is inverted. The collisions become so frequent that the electrons no longer have enough energy to ionize. The voltage is therefore increased because the electrons need to be sufficiently accelerated between two collisions before they reach the next target. The current increases with the pressure due to the density increase which leads to a large number of moving particles.

4.4.1 Gas discharges

For gas discharges, the external circuit (generator, external resistances, capacitances and inductances) dictates if the discharge will develop to a normal glow, abnormal or

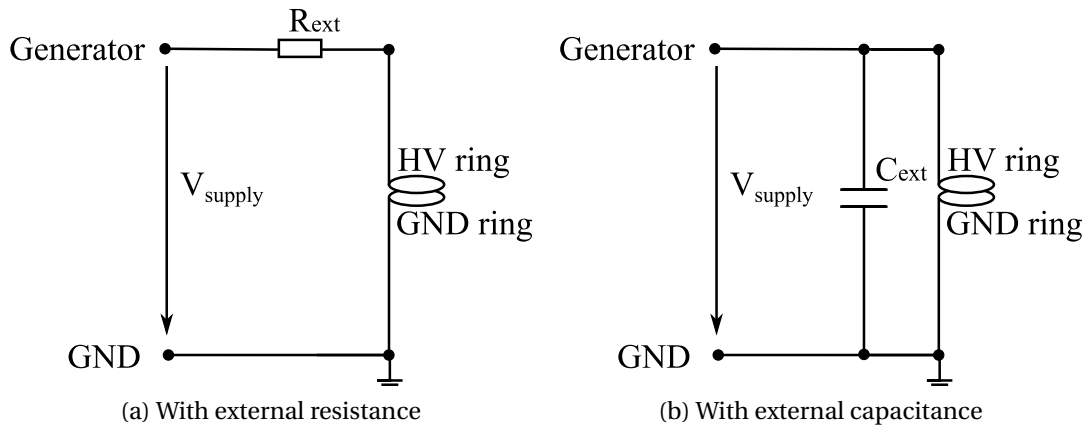(a) With external resistance   (b) With external capacitance

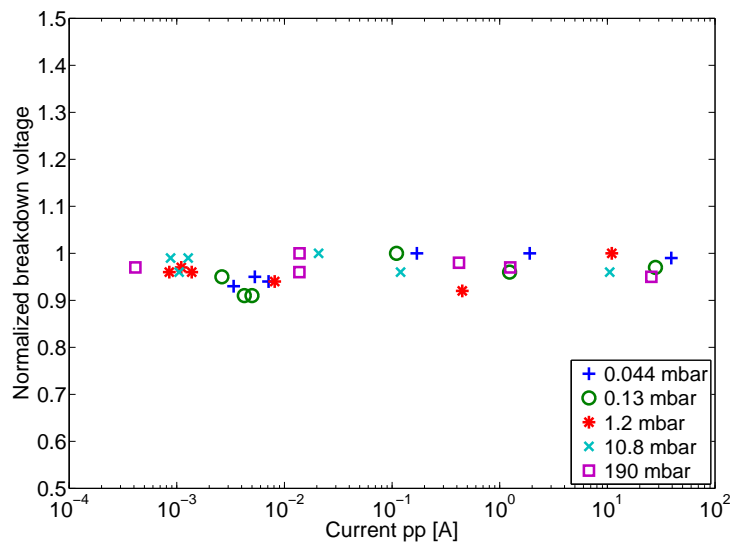Figure 4.30: Electric schematics of external circuit

Figure 4.31: Breakdown voltages in air normalized to the maximum of each pressure. The external resistances limiting the discharge current has significant no impact on breakdown voltage. Nevertheless reducing the current can prevent arcing.
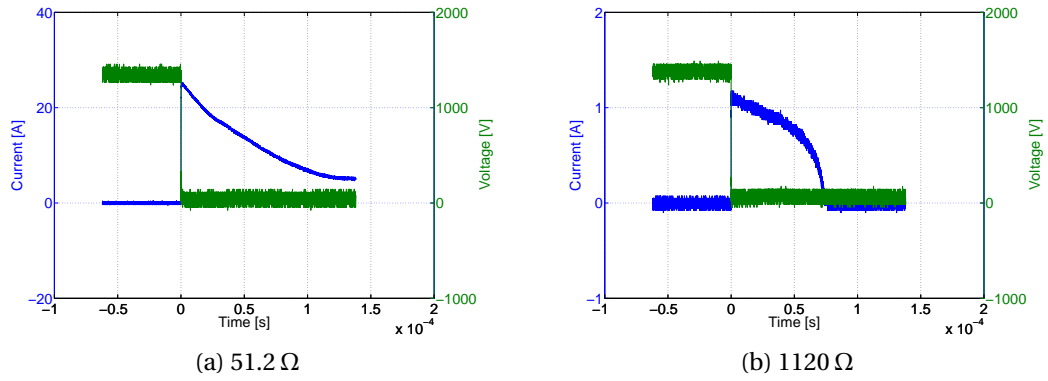
(a) 51.2 Ω   (b) 1120 Ω

Figure 4.32: Breakdown measurement with different external resistances: Current and voltage for 190 mbar in air. Breakdown voltage remains the same.

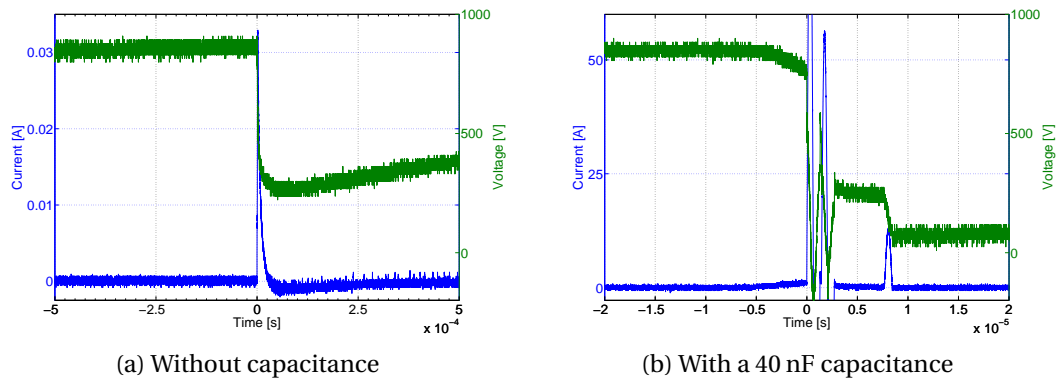(a) Without capacitance   (b) With a 40 nF capacitance

Figure 4.33: Breakdown measurement with/without external capacitance: Current and voltage for 0.83 mbar in air. Breakdown voltage remains the same.
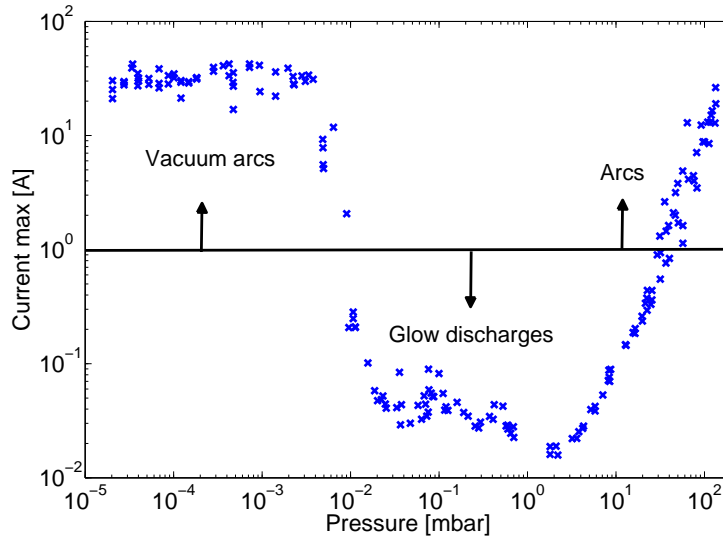
Figure 4.34: Maximum current in air over a large pressure scale. Vacuum arcs and high pressure gas discharge arcs occur above 1 A and transition to glow and glow discharges (glow and corona discharges) below 1 A. These limits suggested by [9, 8] support mostly the observed transitions from the different kind of discharges.

Figure 4.35: Maximum current in air versus breakdown voltage. There is no simple relationship between current and voltage even if the external circuit remains the same during the measurements.

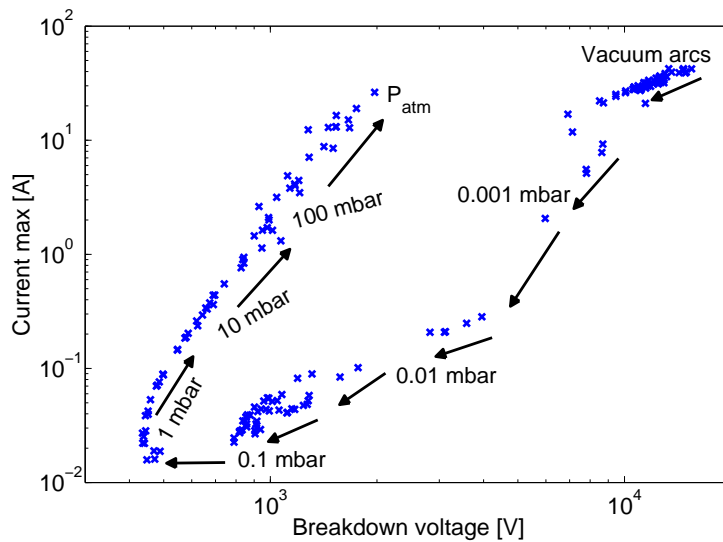arc. As example at 1.2 mbar in figure 4.36, it is possible to approximatively measure the typical current-voltage curve for gas discharges by varying the current limit of the generator, the external resistance and the voltage. For each resistance in zone 1, there is a linear relation between current and voltage typically describing dark current. The discharge is ignited (breakdown) when the breakdown voltage is reached. With high resistances the currents are weak and the discharge develops to a normal glow (zone 2). In this small zone increasing (decreasing) the current, expands (retracts) the glow covering the cathode surface. When no more free surface is available on the cathode, the current increases with the voltage because more electrons per square meter needs to be extracted (zone 3) characterizing the abnormal glow. Zone 4 is the beginning of the arc discharge. Very low resistance such as 51.2 Ω in figure 4.36 can lead directly to high current discharge such as arc. Measuring the dark current can directly predict what kind of discharge will follow the breakdown if the current-voltage curve is known. Nevertheless the current-voltage curve shape depends strongly on pressure. At atmospheric pressure whatever the resistance either arc occurs or no breakdown at all. If the current is limited too much the processes needed for breakdown such as electron avalanche can not develop properly. As example, equilibrium is reached in figure 2.5 where the load line crosses the current-voltage characteristic curve. An external resistance, too big, can steepen the load line slope so much that there is no more intersection and therefore no breakdown. Nevertheless the resistance has to withstand these high constraints (power dissipation) without failing.

Once the current is not limited, the discharge can become out of control even if the breakdown voltage remains the same. Every breakdown can therefore possibly lead to a damaging discharge if the current is not limited. Figure 4.37 shows discharges with more and more current ending with a failure. At the beginning (at the lowest current) the discharge is weak. As soon as the current is increased the total power involved in the discharge is also increased leading to a change in kind of discharge i.e. a change of the equilibrium location in the current-voltage curve. With a sufficient current even arc discharges are possible (above 50% of the current limit in figure 4.37). The light is finally so intense that the picture is saturated in spite of the very small exposure time. High light intensities are directly related to high currents flowing between the electrodes. When the electrodes are enough heated up, metal could evaporated even in gas discharges damaging the setup. Just before complete failure the recorded optical emission spectra in figure 4.38 could illustrate the presence of metal traces from the electrodes. In this case copper emission lines are highlighted. Copper is in fact the main composite of the brass electrodes. The high current discharge is not uniquely a metal composed discharge such as vacuum discharges but contains also gas lines. The argon lines illustrated in figure 4.38 are present in both low and high current discharges.
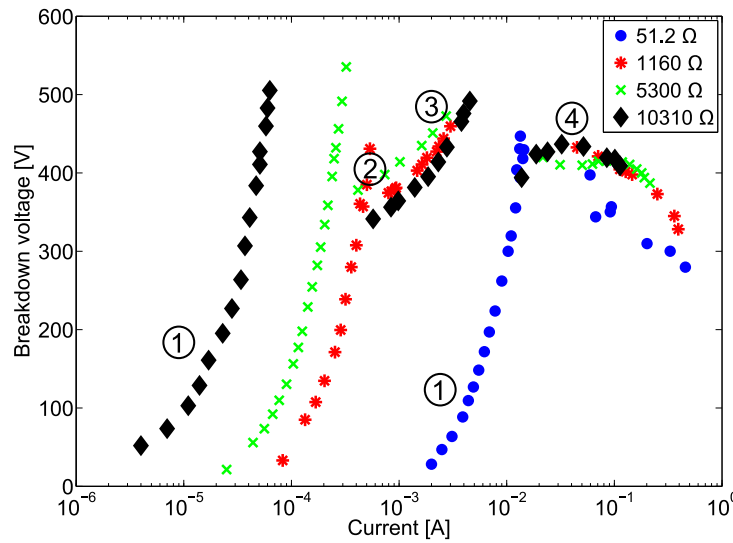
Figure 4.36: Current-voltage characteristic curve in air at 1.2 mbar. Dark current (zone 1), normal glow (zone 2), abnormal glow (zone 3) and transition to arcs (zone 4).

Figure 4.37: Ring assembly without holder. In argon gas at 1.6 mbar, breakdown occur at the same breakdown voltage but the current limit is increased. The current limit in the pictures from left to right is set at 10%, 20%, 30%, 50% respectively 100% of the maximum current limit 1.3 A of the generator.

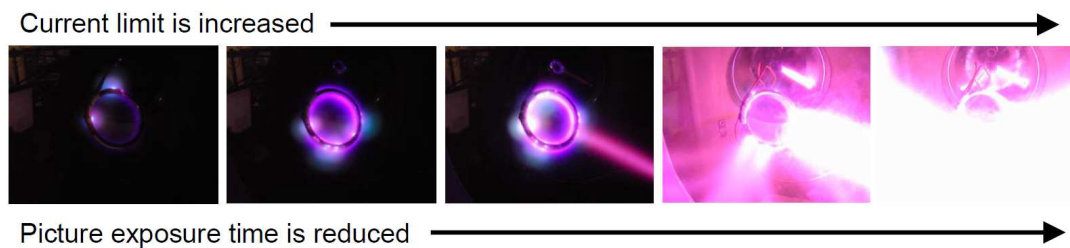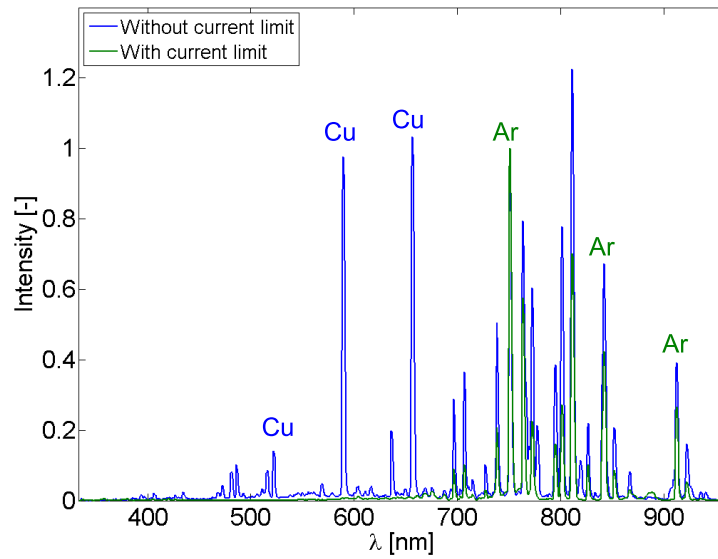Figure 4.38: Optical emission spectroscopy in argon gas at 0.5 mbar normalized to argon emission line 763 nm . Without current limit, high current discharge heat the electrodes up leading to metal evaporation visible in the spectrum.

4.4.2 Vacuum discharges

Conditioning is typical for vacuum discharges and is illustrated in figure 4.39. As explained in section 2.2, a medium is needed for breakdown to occur. Breakdown is located where the electric field is the most enhanced. The first few vacuum arcs may clean the surface from the attached contaminants, dust. After about two dozen arcs (depending on the surface), breakdown voltage is no more increasing but fluctuating (around 10 kV in the figure). Most contaminants are expected to be removed and now the protrusions or metal roughness are playing a major role. During breakdown the metal is melting locally, removing the metal spot responsible for breakdown or creating another defect which could enhance even more the local electric field.
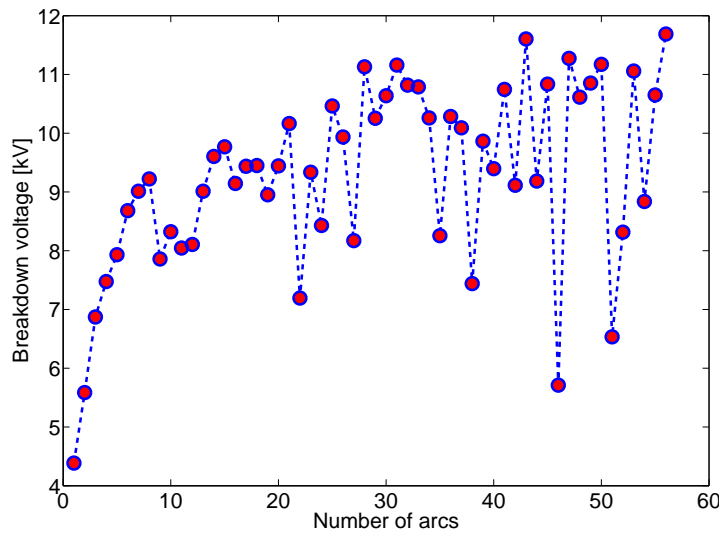
Figure 4.39: DC conditioning in air at base pressure.

4.5 Damages and failures

Most of the experimental measurements did not damage or modify the experimental setup enough so that it became unusable. Nevertheless for vacuum arcs the voltages could be so high that the insulator was to weak to withstand the voltage. Breakthrough strength (see section 3.3) was too low and breakdown occurs as shown in figure 4.40 with the weakest insulator Vetronite®. Limiting the discharge current if possible is a good idea to protect the setup from irreversible damages. In fact high current can heat the electrodes up and the discharge can build a metal bridge between the anode and cathode (figure 4.41). Moreover weaknesses of wire insulation have also been observed in the slip ring tests under high current discharges. The wire insulation evaporated or burned away leaving damaged wire as in figure 4.42. Finally if the discharge is maintained for an enough longer time with high currents the insulators can melt as in figure 4.43.

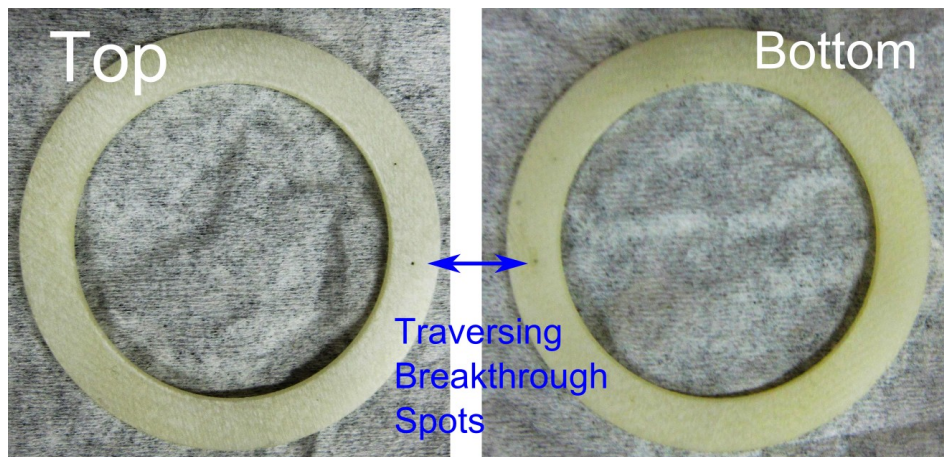Figure 4.40: Breakthrough at voltage around 20 kV. The Vetronite® ring of a thickness of 1 mm shows weakness with such high voltages. Only a few vacuum arcs led to a permanent short circuit.
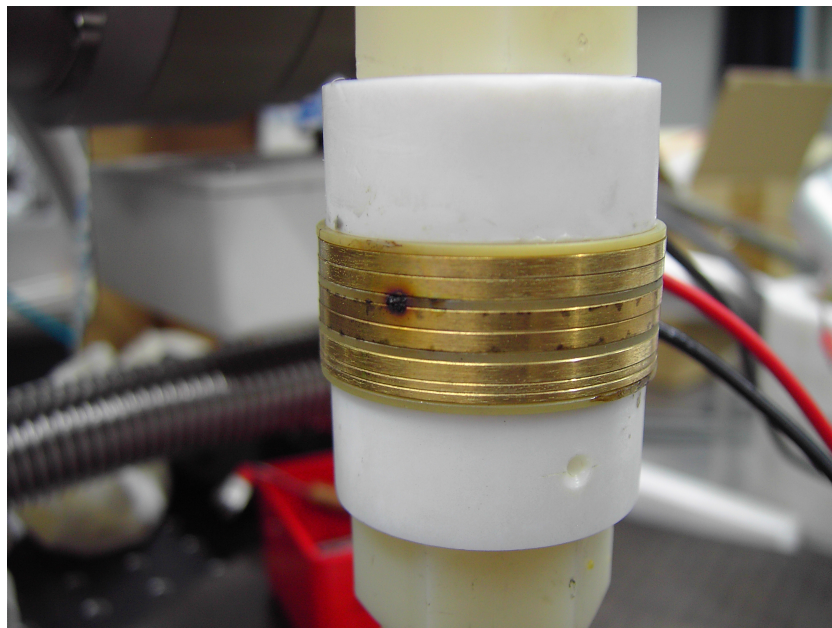

Figure 4.41: Metal bridge between high voltage and grounded rings due to high current gas discharges.
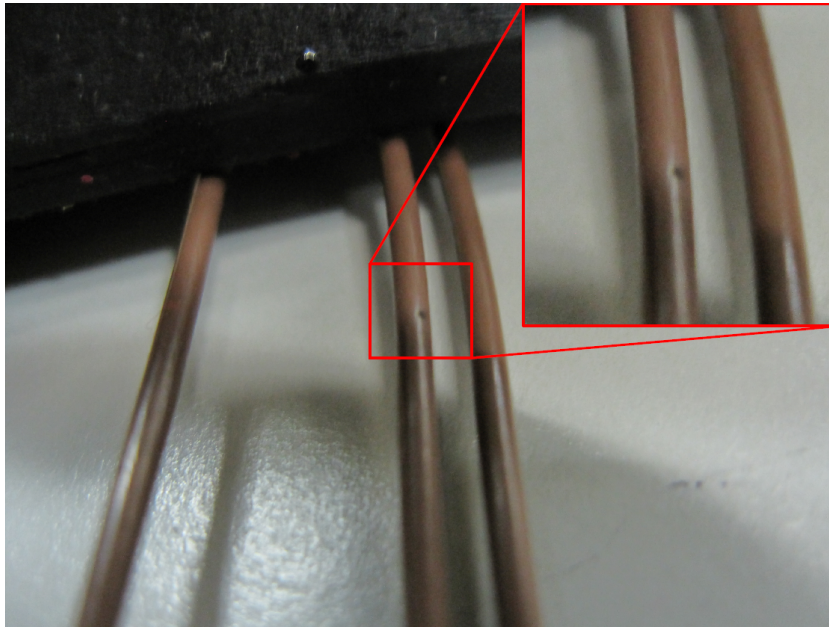
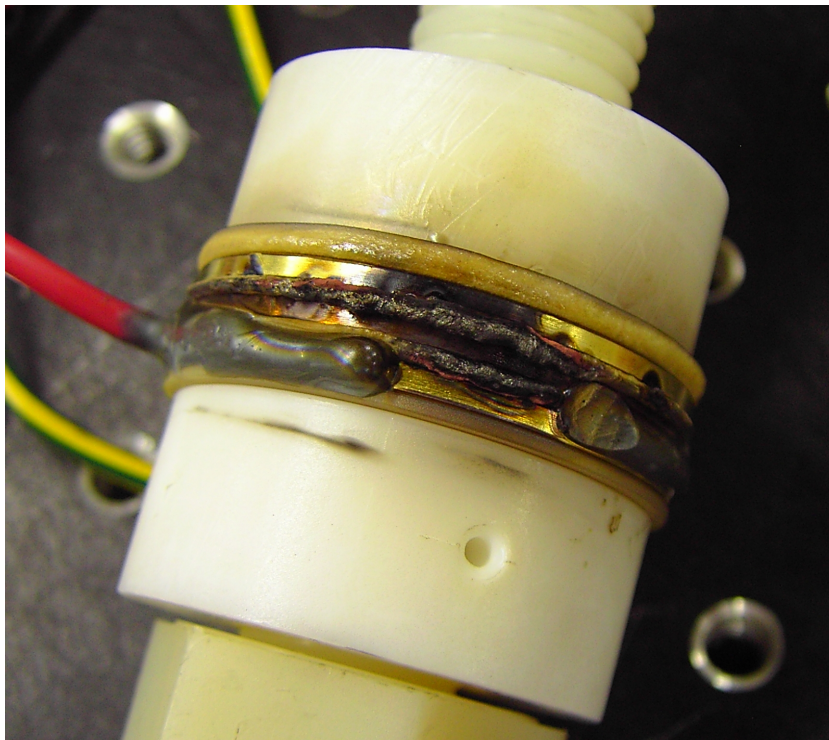Figure 4.42: Wire failure for the slip ring assembly.

Figure 4.43: The insulators did not resist to the high temperature and melted.

5 Numerical Simulation

Numerical simulation of gas breakdown or discharge has started several years ago. Already in the 70's breakdown in non uniform electric fields has been studied [51]. This research topic still remains actual: Numerical model for complex or non usual geometries (Wire-cylinder) [52], gas breakdown at atmospheric pressure in parallel plates [53], streamer formation in a complex geometry [19] or DC gas breakdown in a ring assembly over a large pressure range [54]. This chapter describes an approach of numerical simulation of DC gas breakdown in complex geometry. The aim is here to calculate the global shape from the measured breakdown voltage versus pressure curve in a ring assembly and to understand the underlying breakdown physics. First the breakdown model is presented as well as the important space and boundary conditions. Then the swarm parameters such as mobility and diffusion of particles, ionization coefficient and secondary electron emission coefficient are discussed. Once all parameters are well defined, the simulation of a single gap parallel plate geometry will be presented. The comparison with theoretical breakdown voltages shows that the numerical model represents well the reality for this simple geometry. In a final step simulation of a ring assembly geometry will be undertaken and the calculated breakdown voltages compared to the experimental breakdown voltages.

5.1   DC gas breakdown model

The present simulations are calculated with the finite element software COMSOL 4.2 [55]. Electrons and ions are considered to move independently in an immobile background gas as in [53]. Fluid models are widely used to solve various plasmas (assumed to be charged gases with the pressure high enough to treat the electrons and ions collectively as fluids [56]). They are based on solving the continuity and transport equations in combination with Poisson's equation. In this study, a fluid

model is applied to compute the DC gas breakdown by solving the electron and ion continuity equations and the Poisson's equation. Moreover the species flow is assumed to be laminar. This laminar flow condition is only fulfilled if the Knudsen number Kn = $\lambda_{\mathrm{mfp}}/d < 0.1$ where d is the smallest distance in the geometry and λ_{mfp} the mean free path [57, Section 2.1.2]. The mean free path is defined as the average distance that a particle travels before a collision [57]:

$$\lambda_{\mathrm{mfp}} = \frac{d}{d\sqrt{2}\pi l^2 \rho},$$ (5.1)

where d is the traveled distance (in m), l the molecular diameter of the gas (in m) and ρ number molecule density (in m^{-3}). After simplification with the perfect gas law the expression become:

$$\lambda_{\mathrm{mfp}} = \frac{T}{l^2 p} \cdot 3.067 \cdot 10^{-29},$$ (5.2)

where T is the temperature (in K) and p the pressure (in atm). For a constant temperature, the mean free path is therefore only dependent on pressure and is given in dry air at ambient temperature by: $\lambda_{\mathrm{mfp}} p = 6.726 \cdot 10^{-8}$ [58]. It is possible to link this last expression with the laminar flow condition ($\lambda_{\mathrm{mfp}}/d < 0.1$). For parallel plate geometry in air at ambient temperature this validity condition for a laminar flow can be written as $pd > 6.72 \cdot 10^{-4}$ [mbar·m]. The fluid model validity for complex geometries will be discussed later along with the simulation results.

The breakdown in the numerical simulation is defined by a significant increase of electron density and net flux of electrons and ions as shown in figure 5.1. The simulation stop limit for breakdown is fixed when both density and current reach at least 1000 times their values calculated at the end of the initial stabilization time. This means that when these two conditions are reached the simulation is stopped and the breakdown voltage is determined. 1000 times was chosen as a good limit because above this value the calculations needed much longer time to finish the computation due to the exponential increases (large gradients) of densities.
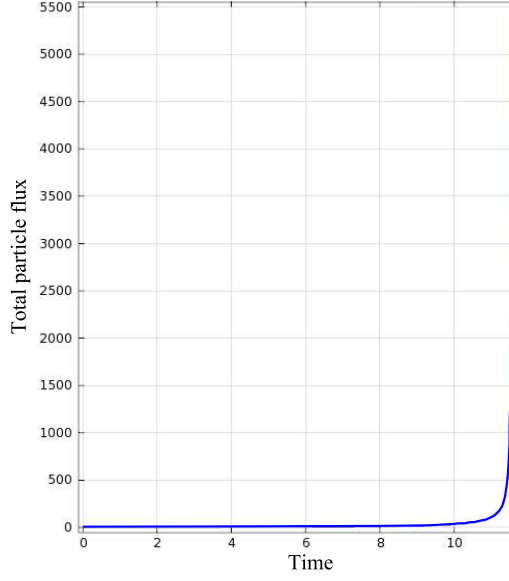
Figure 5.1: Typical total flux exponential increase showing breakdown.

5.1.1 Fluid model and electrostatics equations

The two-fluid model describes each species by a continuity equation [59]:

$$\frac{\mathrm{d}n_j}{\mathrm{d}t} + \vec{\nabla} \cdot \vec{\Gamma}_j = S_j \,, \tag{5.3}$$

where n_j is the density and S_j the net source term for species j. The flux Γ_j is the sum of a diffusive and a convective flux term, neglecting the background gas velocity:

$$\vec{\Gamma}_j = \vec{\Gamma}_j^{\mathrm{Diffusive}} + \vec{\Gamma}_j^{\mathrm{Convective}} \tag{5.4}$$

$$= -D_j \vec{\nabla} n_j + \frac{q_j}{|q_j|} \mu_j n_j \vec{E} \,, \tag{5.5}$$

where D_j, μ_j and q_j are respectively the diffusion coefficient, the mobility and the charge of each species. Furthermore, the electric field $\vec{E} = -\vec{\nabla}V$ is calculated from the Poisson equation and the boundary conditions on voltage. Before breakdown the charged species have negligible influence on the vacuum potential due to their very low densities. Therefore the Poisson's equation can be replaced by the Laplace

equation :

$$\nabla^2 V = -\frac{(n_\mathrm{i} - n_\mathrm{e}) \cdot \mathrm{e}}{\epsilon_0} \approx 0 \,, \tag{5.6}$$

where e is the electron charge and ϵ_0 the vacuum permittivity. This assumption must be discussed for numerical simulation with high pressures and voltages especially when streamers could appear [17] (the local electric field produced by the charged particles becomes important compared to the applied electric field). However in our worst condition for pd, breakdown occurs at high pressure in the smallest path length as shown by experimental and numerical simulation results. This gives $pd <$ 1.8 mbar m which is below the value of the streamer limit of 2.63 presented in section 2.1.2. Moreover the calculated electron and ion densities even at atmospheric pressure are so low before breakdown and lead to $\frac{(n_\mathrm{i} - n_\mathrm{e}) \cdot \mathrm{e}}{\epsilon_0} < 10^{-6}$. Furthermore, since the electron and ion densities remain low, surface charge accumulation on insulators is neglected. Partial differential equation modules (PDE) are used in COMSOL for the species fluid model. The electric part is implemented in the electrostatic module.

5.1.2 Space and boundary conditions

Boundary conditions for each species are required for the cathode, the anode and the insulators. Physically the electron and ion densities are zero at surfaces because the charges are neutralized there [6]. Fixing the electron and ion densities to zero at the surfaces as [60] or [53] can lead to large gradients in a thin layer close to the boundary. Any attempt to find a solution will then lead to numerical instabilities [56]. Another way is to fix densities at a very small value but nonzero [61]. Instead of boundary conditions using zero densities ($n_\mathrm{i} = n_\mathrm{e} = 0$), flux boundary conditions are chosen here up to an undefined thin boundary layer thereby avoiding large gradients and numerical instabilities [56]. In this numerical model, the boundary condition on the anode for ions is a condition of zero flux as in [10] because no ions arrive at the anode. The boundary conditions on the cathode are secondary emission for the electron and convective flux for the ions [56]. The boundary conditions of various authors are:

	Anode	Cathode
[10]	$J_\mathrm{i} = 0$	$J_\mathrm{e} = \gamma J_\mathrm{i}$
[53]	$n_\mathrm{e} = n_\mathrm{i} = 0$	$J_\mathrm{e} = \gamma J_\mathrm{i}$
[61]	$n_\mathrm{e} = n_\mathrm{i} \sim 0$	$J_\mathrm{e} = \gamma J_\mathrm{i}$
[56]	$n_\mathrm{e} = 0$ and $J_\mathrm{i} = J_\mathrm{i}^{\mathrm{Convective}}$	$J_\mathrm{e} = \gamma J_\mathrm{i}$ and $J_\mathrm{i} = J_\mathrm{i}^{\mathrm{Convective}}$

where J_i and J_e are the ion and electron current densities respectively, and γ the secondary electron emission coefficient. [56] states to justify the ion flux boundary condition (and not the use of the zero density boundary condition): "The positive ion boundary condition (also at the cathode) is that the ion flux at the anode is due only to drift. This forces a nonzero ion density at the electrode surface, even if the ion neutralization is suspected to be efficient near the surface. Since a perfectly absorbing boundary implies a zero particle density at the surface, this flux boundary condition is not strictly correct. The formation of an extremely thin ion diffusion boundary layer is neglected since the primary interest is not the details of the ion density profile very near the electrode surface. Moreover, the flux boundary condition gives a good approximation to the ion flux at the boundary, which is the more important quantity. In the limit of larger electric fields, an asymptotic analysis shows that this approximation becomes exact, so under typical discharge conditions, this boundary condition works well." The reason to avoid the very thin ion diffusion boundary layer is because of numerical difficulties as described by [61]. If the steep boundary layers are not sufficiently resolved, oscillations will occur in the solution. This problem is avoided by the use of the flux boundary conditions, which appear to be accurate if the electric fields are high enough.

The cathode is a source of electrons created by ion impact quantified by the secondary electron emission coefficient γ_{se}. Only electrons are lost at the anode. Finally the insulators are defined as charge absorbing surfaces: each electron or ion reaching an insulator is neutralized. As self-consistency test in a single gap geometry with a constant electric field, the total electron/ion flux should be conserved across the full gap width. From all tested boundary conditions, those which give convergence and self-consistent results are described for the ions by :

$$\vec{n} \cdot \vec{\Gamma}_i^{\text{cathode}} = \vec{n} \cdot \vec{\Gamma}_i^{\text{Convective}} , \tag{5.7}$$

$$\vec{n} \cdot \vec{\Gamma}_i^{\text{anode}} = 0 , \tag{5.8}$$

$$\vec{n} \cdot \vec{\Gamma}_i^{\text{insulator}} = \vec{n} \cdot \vec{\Gamma}_i^{\text{Convective}} , \tag{5.9}$$

and for the electrons by :

$$\vec{n} \cdot \vec{\Gamma}_e^{\text{cathode}} = -\gamma_{\mathrm{se}} \, \vec{n} \cdot \vec{\Gamma}_i^{\text{cathode}} , \tag{5.10}$$

$$\vec{n} \cdot \vec{\Gamma}_e^{\text{anode}} = \vec{n} \cdot \vec{\Gamma}_e^{\text{Convective}} , \tag{5.11}$$

$$\vec{n} \cdot \vec{\Gamma}_e^{\text{insulator}} = \vec{n} \cdot \vec{\Gamma}_e^{\text{Convective}} , \tag{5.12}$$

with ñ the normal vector outward to the surface. The source term in equation (5.3) is defined only by the gas ionization. Other sources like photoionization and losses such as attachment or recombination are neglected. The final source term $S_i = S_e = S$, which is the number of ion-electron pairs per unit volume created by gas ionization through electron impact, can be written as follows :

$$S \quad = \quad \alpha \cdot \Gamma_e^{\text{Convection}} + S_{\text{cosmic}}, \tag{5.13}$$

where α is the Townsend first ionization coefficient and S_{cosmic} is the constant background ionization rate due to cosmic radiation. The background ionization is needed to initiate the ionization in the volume but could not lead to breakdown by itself because it cannot generate the electron avalanche. S_{cosmic} is therefore arbitrary set to 1 [ion pairs $\text{m}^{-3}\text{s}^{-1}$]. The most important factor in the source S for numerical breakdown calculation is the first term ($\alpha \cdot \Gamma_e^{\text{Convection}}$). It is responsible for the so called electron avalanche and describes the particle production through ionization generated by the electron flow in the volume. The initial conditions for densities is $n_e = n_i = 0$ because the gas is assumed not to be ionized at the begin of the breakdown numerical simulation. If the initial densities are set with too high values there could be a density drop in the first time steps leading to numerical instabilities. In order to represent the experimental measurements a voltage ramp is applied using a time dependent solver. The applied voltage is first defined as constant (100 V which is below the breakdown voltage) over $t = 1$s used to stabilize the simulation. This process helps to obtain an equilibrium state before breakdown (equilibrium between particle losses on the walls and production): With a physical point of view, the dark current corresponding to 100 V is reached. The voltage is then increased linearly with time with a ramp of $1000\,\text{V}\,\text{s}^{-1}$, slow enough to keep numerical overvoltage errors as low as possible and reasonable calculation times, but not too slow to avoid long calculation times. In the table below is shown an example of a breakdown simulation in a parallel plate geometry:

Voltage ramp [V s^{-1}]	Calculated breakdown voltage [V]	Calculation time [s]
1000	480	183
100	473	3050
10	470	65022

(a) Simple mesh: uniform element size of 10^{-4} m

(b) Refined mesh near the electrodes: smallest size $5 \cdot 10^{-5}$ m (blue) and biggest $5 \cdot 10^{-5}$ m (red)
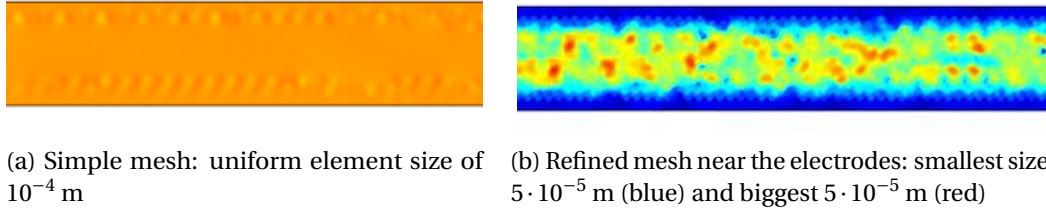
Figure 5.2: Typical mesh size for a parallel plate configuration with a gap of 1 mm

5.1.3 Meshing

The meshing is very important in finite element calculations. The surface or volume is separated into a number of smaller elements. The computation time increases with the number of mesh elements. The meshing should therefore be fine enough (especially in region where high gradients are present) to get accurate results, convergence and stability, and coarse enough to avoid long calculation times. The widely used triangle shape elements generally give good results in simple geometries. An element size distribution is shown in figure 5.2 for a parallel plate geometry. The mesh is generally refined near the electrodes for plasma numerical simulation (see figure 5.2(b)) because high gradients can appear there. For a complex geometry like a ring assembly in a big vacuum chamber it is much more difficult to obtain an ideal meshing (for short calculation times and accurate solutions) because there are small and large distances to cover. The aim was to find a mesh usable for all pressures. Figure 5.3(a)-(d) illustrates some examples to avoid (wrong meshing, no refinement, too large mesh size gradient, too big mesh size elements). Nevertheless the mesh in figure 5.3(e) and figure 5.3(f) both worked quite well in our situation. The mesh in figure 5.3(e) needed nevertheless longer calculation times to get the solution than the one in figure 5.3(f) because there were more elements than necessary. This particular meshing is used for the full range of pressure. For calculation only at high pressure the breakdown occurs in the smaller gaps. Either the mesh could be refined only in the small gaps or the full geometry can be reduced to the small gaps in order to avoid unnecessary calculation in the long gaps.

### 5.1.4 Swarm parameters and secondary electron emission coefficient

In the transport equations there are the swarm parameters for the electrons (D_e and μ_e) and for the ions (D_i and μ_i). The mobility coefficient μ_j, and diffusion coefficient D_j for electrons and ions as well as the first Townsend ionization coefficient α and
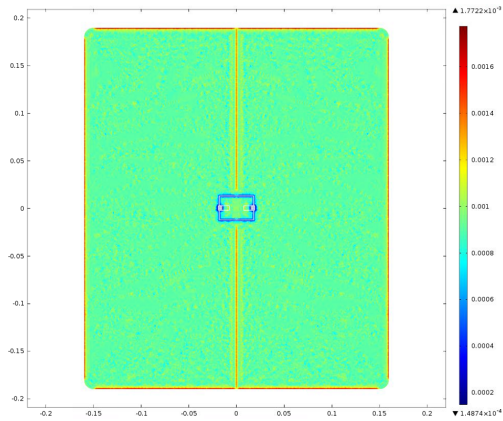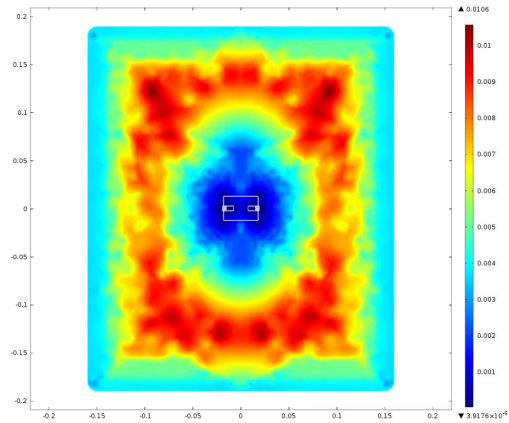
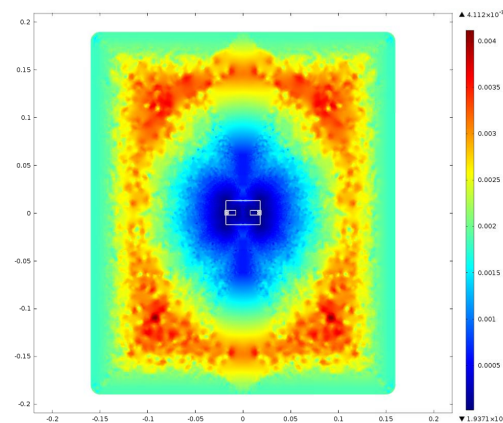(a) Element size bigger near the vacuum chamber wall than in the volume
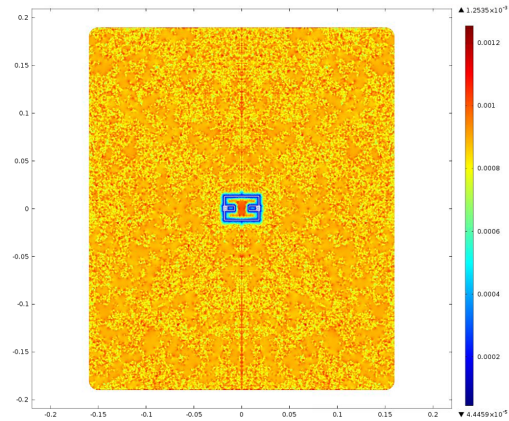
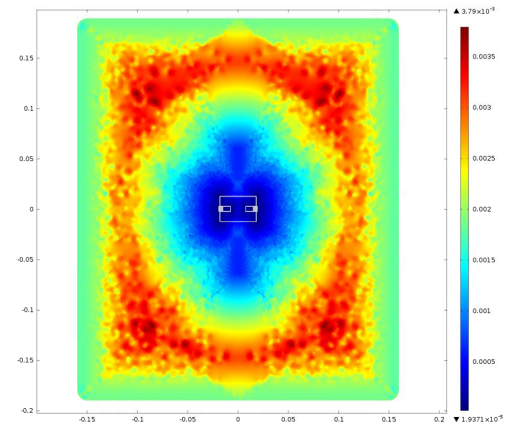(b) No refined mesh near the vacuum chamber wall
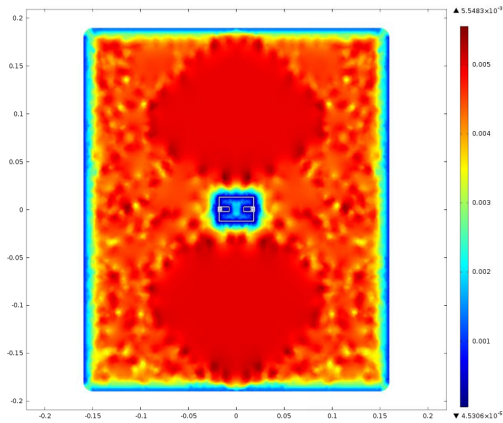
(c) Mesh size changes too fast

(d) Maximum mesh size in the volume too large

(e) Too many elements

(f) Ideal mesh

Figure 5.3: Different meshing size distribution for the ring assembly (white) in the middle of the vacuum chamber.

secondary electron emission γ_{se} coefficient are functions of the local reduced field E/p. Initially the swarm parameters from [53] where used but the model covered only numerical simulation at atmospheric pressure. The need for precise swarm parameter for electrons and ions covering a large pressure and electric field range was mandatory. The coefficients for electrons could be derived by first solving the electron Boltzmann equation and then by formally fitting the numerical data as in [62] or taken in literature such in [63]. Each method can give results with some differences as in [64] which compares the Boltzmann and Monte Carlo calculations. A more recent method similar to [65] is suggested here. Using cross section data from [66] for N_2 and [67] for O_2 in BOLSIG+ (Boltzmann equation solver software [68]) the electron transport coefficients as well the ionization rate in air were obtained using a gas composition of 80% N_2 and 20% O_2 at 273 K. The fit expressions of electron swarm parameters are in fair agreement with the presented coefficients for $N_2 : O_2$ mixture of a ratio $80 : 20$ in [69]. α has been fitted with its theoretical expression $\alpha = A\,p\,\exp(-B\,p/E))$. The collision cross section decreases for very high energies leading to strong changes of all the swarm parameters values [9]. For E/p above 10^5 Vm^{-1}mbar^{-1} the extrapolated swarm parameter validity is not guaranteed. The fit expressions used in this thesis are :

$$
\mu_e \cdot p = 948.5 \tanh\left(-3.494 - 0.6097\log\left(\frac{E}{100\,p}\right)\right) + 948.5 \qquad \frac{E}{p} < 0.18 \qquad (5.14)
$$

$$
= 139.6\left(\frac{E}{100\,p}\right)^{-0.3455} \qquad\qquad 0.18 \le \frac{E}{p} < 1150 \qquad (5.15)
$$

$$
= 60, \qquad\qquad \frac{E}{p} > 1150, \qquad (5.16)
$$

$$
D_e \cdot p = 46 + 22.26\left(\frac{E}{100\,p}\right)^{0.2807} + 0.5787\left(\frac{E}{100\,p}\right), \qquad (5.17)
$$

$$
\alpha/p = 2900\exp\left(-28070\frac{p}{E}\right). \qquad (5.18)
$$

Many authors have determined ion swarm parameters for various conditions [70, 71]. Based on cross sections, ion swarm coefficients have been calculated in dry air from an optimized Monte Carlo method adapted for ion transport in gas mixtures [71]. Swarm parameters for N_2^+ and O_2^+ are similar. Since the ion density ratio of N_2^+ to O_2^+ is unknown, the transport coefficients of N_2^+ have been taken as an approximation for ions in air. Ion diffusion and mobility fit expressions used in this numerical simulation are:

$$\mu_i = 4.6 \cdot 10^{-5} + 0.0801 \exp\left(-0.005 \cdot \left(\frac{E}{100 \, p} + 1251\right)\right), \tag{5.19}$$

$$D_i \cdot p = 0.645163 + 0.0562447 \left(\frac{E}{100 \, p}\right)^{0.8378}. \tag{5.20}$$

The secondary electron emission coefficient γ_{se} has been set with a typical value of 0.01 on both rings and vacuum chamber walls for the numerical simulation as in [53]. As the rings and the chamber walls are made of different metals it can be expected that γ_{se} could be different [72]. γ_{se} can also vary according to the kind of ion impacting on the electrodes. γ_{se} has been studied for different electrode materials and gases [73, 74, 75] or temperature [76]. The results show variations over several orders of magnitude for γ_{se} as a function of reduced electric field or temperature which would strongly affect the breakdown voltage calculations as can be seen from equation 2.9. Moreover the secondary electron emission coefficient could be considered as an effective coefficient of secondary emission [73] taking into account not only secondary electrons released by ion or metastable impact on the cathode but also other contributing secondary electron production processes such as photoemission. Each additional process modifies the value of γ_{se} as illustrated by [77] which showed a γ_{se} change with electron backscattering consideration. Figure 5.4 illustrates the effect of γ_{se} on breakdown voltages using analytic expression (equation (2.9)). A higher γ_{se} decreases the minimum breakdown voltage and shifts $(pd)_{V_{Bd}}$ to the left (see equation (2.10)).

5.2   Model validation in a parallel plate geometry

In order to verify our model, breakdown voltages for a single gap parallel plate geometry were calculated numerically and compared to the analytic expression. The simulation is in good agreement with the theoretical expression of the Paschen curve as shown in figure 5.5. Moreover the coefficient A and B extrapolated from the simulation curve have the same order of magnitude as the values given for air in [6, Table 14.1] or [9, Table 4.1].

In the steady state case with unidirectional drift and assuming that diffusion is negligible in comparison to drift, the continuity equation (5.3) changing the fluxes into
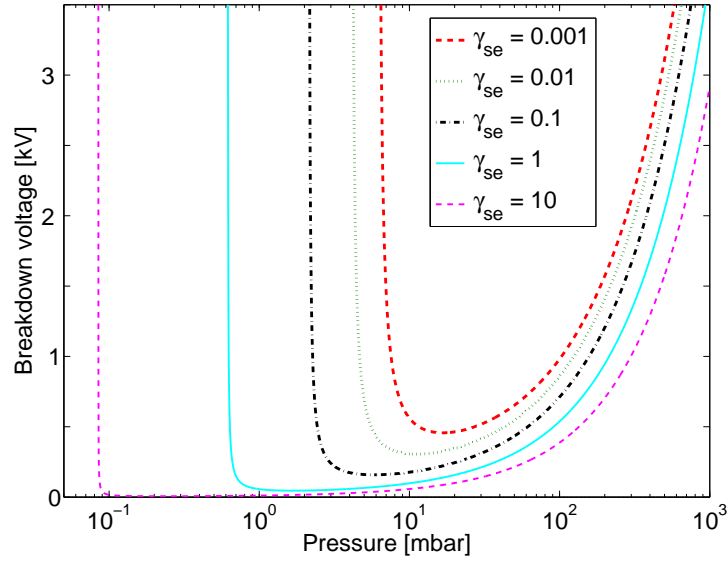
Figure 5.4: Analytic Paschen curves in a 1 mm gap width parallel geometry for different γ_{se} based on A and B in air from [9]. An increase of γ_{se} reduces the minimum breakdown voltage and widens the Paschen curve.
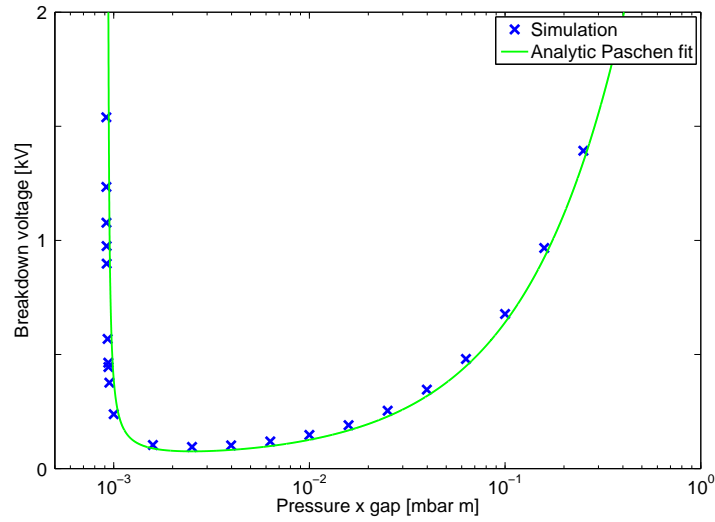

Figure 5.5: Paschen curve for a single gap parallel plate ($d = 0.001$ m, $\gamma_{se} = 0.01$): Simulation and analytic fit ($A = 4984 \pm 14$ mbar$^{-1} \cdot$ m^{-1}, $B = 30000 \pm 1299$ V$\cdot$mbar$^{-1} \cdot$ m^{-1}).

current densities becomes:

$$\frac{\mathrm{d}J_i}{\mathrm{d}x} = -\alpha \cdot J_e \tag{5.21}$$

$$\frac{\mathrm{d}J_e}{\mathrm{d}x} = \alpha \cdot J_e \tag{5.22}$$

The background ionization S_{cosmic} has also been neglected because its value is weak compared to the particle production by ionization. The total current density is obtained by adding the two equations above and integrating:

$$J = J_i + J_e = \mathrm{const}\,, \tag{5.23}$$

as in figure 5.6. In the next paragraph the profile of the ion and electron current densities will be deduced. The current density boundary conditions at the anode ($x = 0$) is determined by the secondary electron emission by ion impact and at the cathode ($x = \mathrm{L}$) the absence of ion emission:

$$J_e(x = 0) = \gamma_{\mathrm{se}} J_i(x = 0) = \underbrace{\frac{\gamma_{\mathrm{se}}}{1 + \gamma_{\mathrm{se}}} J}_{\text{using equation (5.23)}} \tag{5.24}$$

$$J_i(x = \mathrm{L}) = 0 \tag{5.25}$$

$$J_e(x = \mathrm{L}) = J \tag{5.26}$$

For a fixed pressure, a steady state case and a uniform electric field across the gap, $\alpha(E/p) = \mathrm{const}$. Equation (5.22) is integrated across the gap and the current density is obtained with the help of the boundary condition on the cathode (equation (5.24)):

$$J_e(x) = \frac{\gamma_{\mathrm{se}}}{1 + \gamma_{\mathrm{se}}} J \exp(\alpha x) \tag{5.27}$$

Additionally the boundary condition on the anode can be satisfied only if the self-sustained criterion is fulfilled: $\exp(\alpha \mathrm{L}) = 1 + 1/\gamma_{\mathrm{se}}$ [9]. Using this last equation the current density can be written:

$$J_e(x) = J \exp[\alpha(x - \mathrm{L})] \tag{5.28}$$

$$\underbrace{\Rightarrow}_{\text{equation (5.23)}} J_i(x) = J\{\exp[-\alpha(x - \mathrm{L})] - 1\} \tag{5.29}$$

These two last equations describing the electron and ion current densities across the gap now fulfill both the boundary conditions (defined by equation (5.24), equation (5.25) and equation (5.26)). These electron and current profiles correspond to the
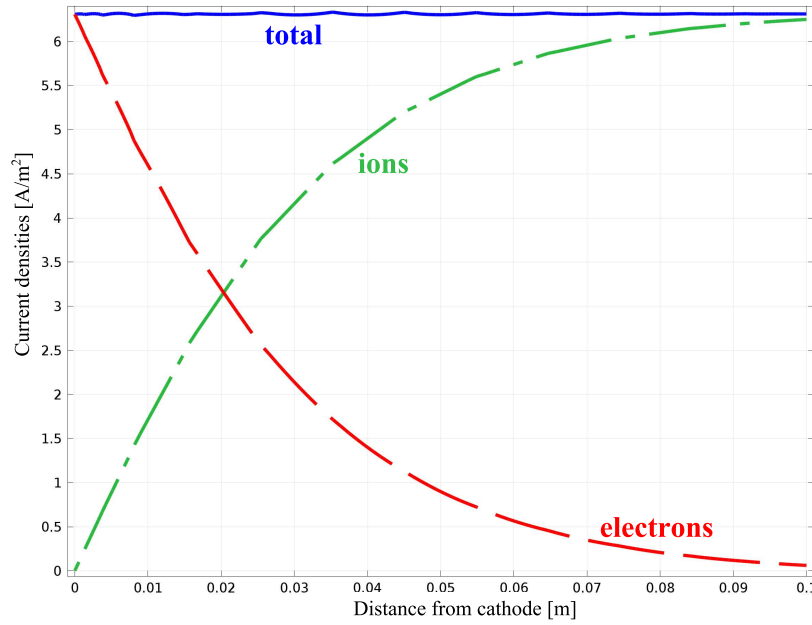
Figure 5.6: Calculated total, electron and ion current densities across 100 mm single gap geometry at 1 Pa and 1 kV. Total flux constant over the gap as in [9, figure 8.6] and in agreement with equation (5.23).

ones calculated in the numerical simulation as presented in figure 5.6.

The electron and ion density as well as the fluxes across the gap are represented in figure 5.7-figure 5.8. The ions are moving towards the cathode, in the opposite direction of the electrons as expected. Based on equation (5.23) the total flux is constant across the gap by adding the electron and ion flux whatever the pressure. Moreover the electron and ion density gradients are bigger at high pressure because diffusion becomes important only at low pressures and is quite negligible at high pressures.

5.3   Double and multi gap geometries

As a second step for understand breakdown in complex geometry, it is helpful to consider a double gap geometry as shown in figure 5.9 which is an axisymmetric geometry with a 1 mm central gap (d_1) surrounded by a 100 mm gap (d_2). These dimensions were chosen in accordance with the shortest and longest electric field line lengths in the ring assembly geometry. The 100 mm gap corresponds approximatively to the distance from the anode ring to the farthest cathode, the grounded vacuum chamber, whereas the 1 mm gap represents roughly the smallest distance between

(a) Electron density
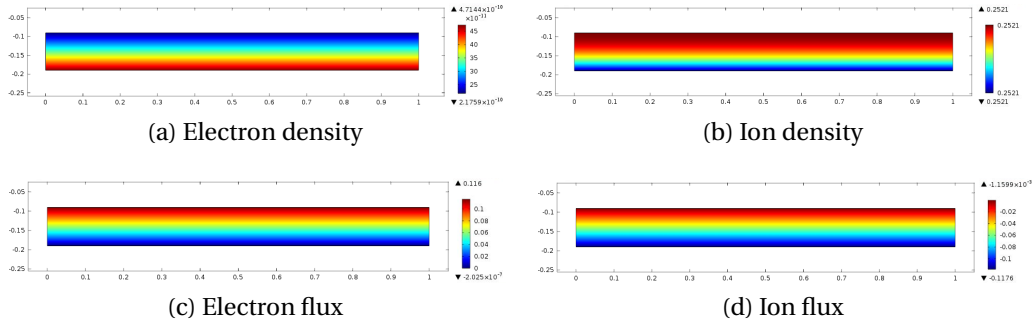
(b) Ion density

(c) Electron flux

(d) Ion flux

Figure 5.7: Parallel plate geometry with 1 mm gap at 0.001 mbar and 1000 V. The X-axis is the radius and the Y-axis is the height in m. The top electrode is grounded and the bottom electrode is at high voltage.

(a) Electron density

(b) Ion density
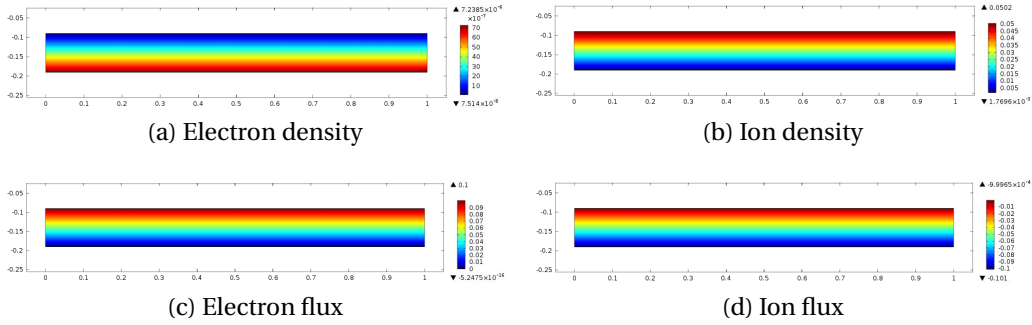
(c) Electron flux

(d) Ion flux

Figure 5.8: Parallel plate geometry with 1 mm gap at 1000 mbar and 1000 V. The X-axis is the radius and the Y-axis is the height in m. The top electrode is grounded and the bottom electrode is at high voltage.

two conductor rings. In figure 5.9(a), the electrodes are separated by an insulating wall and therefore electric field lines are vertical, so there are only two distinct path lengths for breakdown. If the insulating wall is replaced by a conductor as in figure 5.9(b), the geometry can be considered to be multi-gap because all path lengths between 1 mm and 100 mm are available for breakdown as shown by the curved electrical field lines. Figure 5.10 shows the dimensions of the double and multi-gap geometries used in the numerical simulation.

Figure 5.11 shows the calculated breakdown voltages versus pressure for single gap parallel plates geometries (1 mm and 100 mm) compared to the double and multi-gap geometries in figure 5.9(a) and figure 5.9(b). Breakdown voltages are shown as a function of pressure, not pressure times distance as in the Paschen curve, because these geometries present more than a single breakdown path. Expressed as a function of pressure times gap width, breakdown voltage curves for parallel plate geometries with single gap widths of 1 mm and 100 mm are superposed (Paschen curves). These
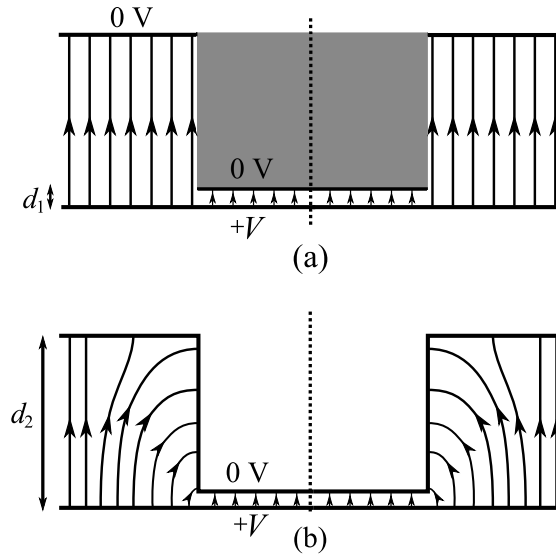
Figure 5.9: Schematic of cylindrically-symmetric (d_1 and d_2) geometry showing electric field lines between the electrodes taken from COMSOL. The base electrode is at positive potential V and the other electrodes are grounded. (a) Double gap: Insulator separation (grey region) between the two gaps leading to only two electric field path lengths. (b) Multi gap: All surfaces are conductors and therefore many electric field path lengths are available for breakdown.
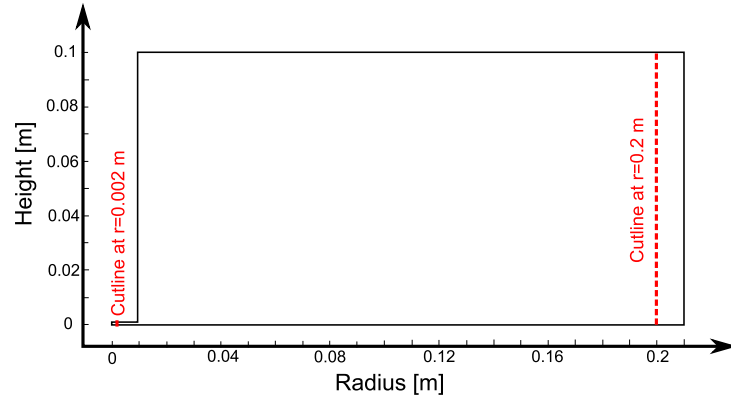

Figure 5.10: Dimensions of the double or multi-gap geometry. The cut lines are set for current densities profiles across the small and big gap (1 mm and 100 mm).

single gap curves are shifted on the X-axis in figure 5.11 by a factor 100 corresponding to the ratio of their gap width because the breakdown voltage is expressed only versus the pressure and no more versus pd. For gas pressures above 1 mbar, double gap geometry breakdown voltages correspond to 1 mm single gap ones. In fact, breakdown occurs in the smallest gap of the double gap at these high gas pressures because
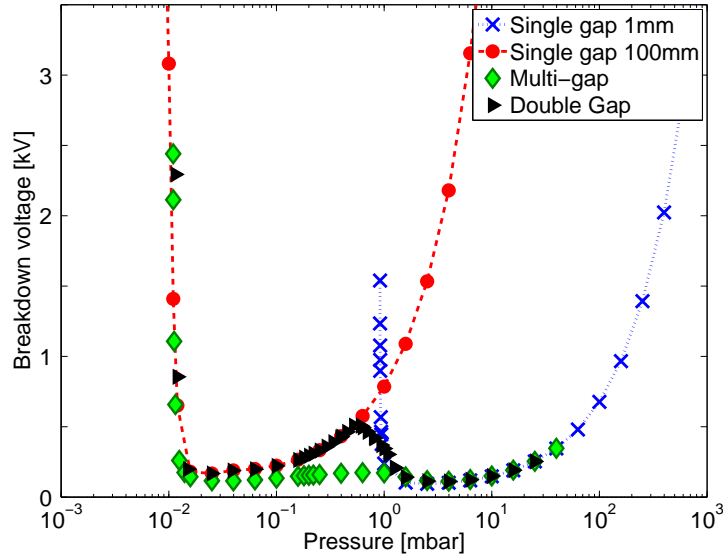
Figure 5.11: Calculated breakdown voltage versus pressure curve for 1 mm single gap, 100 mm single gap, double gap and multi-gap geometry.

breakdown in the 100 mm gap needs a much higher voltage as in the 1 mm gap as shown in figure 5.11. For gas pressures below 1 mbar, breakdown is located in the 100 mm gap because lower voltage is needed for breakdown in bigger gaps than for smaller gaps for so low gas pressures. For the double gap geometry in figure 5.9(a), the locus of the breakdown curve therefore follows the lowest values of the 1 mm and 100 mm Paschen curves. The breakdown switches from one gap to the other as the pressure changes across the curve intersection near 1 mbar. The same explanations can be used to describe the breakdown voltages for the multi-gap geometry in figure 5.9(b). Breakdown occurs in the gap which needs the least voltage for breakdown compared to the other gaps. Contrary to double gap geometry, multi-gap offers not only 1 mm and 100 mm breakdown paths but also every distance in between. An example of breakdown in an intermediate gap is shown in figure 5.13 by the net current density following a curved intermediate-length electric field line. This explains the constant minimum breakdown voltage from 0.02 mbar to 1 mbar in figure 5.11. At higher and lower gas pressures, the breakdown is located respectively in the smallest and biggest gap of the double gap geometry as confirmed experimentally by Marić et al. [78]. The electron densities in figure 5.12 at different pressures support these last conclusions. Above 2.5 mbar the densities reach their maximum in the smallest (1 mm) gap. If the pressure decreases, the difference between the double and multi-gap geometry becomes clear: The densities spread in the biggest gap for the double gap geometry whereas the electrons remain in an intermediate gap of the multi-gap

geometry. When the pressure is low enough ($p < 0.02$ mbar) the densities look again similar because both fill the biggest gap. Due to high diffusion at lower pressure the particles can fill almost the entire volume.

The validity of the fluid model needs to be discussed for double and multi-gap geometries. For a single gap parallel plate geometry the low pd threshold based on equation (2.10) equals to $9.25 \cdot 10^{-4}$ m $\cdot$ mbar (with $A = 4984$ mbar$^{-1} \cdot$ m^{-1} from the fit in figure 5.5 and $\gamma_{se} = 0.01$ default value as used in simulation). According to this value and to the fluid model validity criterion $pd > 6.42 \cdot 10^{-4}$ mbar $\cdot$ m calculated in 5.1 it is possible to confirm the fluid model validity in our case for parallel plate geometry. The Knudsen number Kn $= \lambda_{\mathrm{mfp}}/d$ is theoretically defined with the smallest characteristic dimension in configuration studied, i.e. 1 mm for our present geometries. Based on the fluid validity criterion, the pressure should therefore be more than 0.64 mbar to ensure the fluid model validity. Below this pressure, the mean free path is longer than a tenth of the small gap width which is a necessary condition to use the fluid model. Nevertheless, the fluid model can still be used even for pressures below this fluid validity criterion, because breakdown no longer occurs in the 1 mm gap but in a longer path length where the fluid model is still valid.

This last conclusion can be supported by the current densities across the gap in the multi-gap geometry (figure 5.14 and figure 5.15). Cut lines have been placed at $r = 0.002$ m for the 1 mm gap and at $r = 0.2$ m for the 100 mm as shown in figure 5.10 and are used to show the current densities along the line across the small and the big gap. The total current density is constant across the smallest gap at higher pressure because the fluid model is valid figure 5.14(a)-(b). The model then loses its validity (figure 5.14(c)-(f)) below 1 mbar, around the fluid model validity threshold. Contrary to the smallest gap the total current density is constant in the biggest gap (100 mm) illustrated in figure 5.15. No plasma is present in the 100 mm gap (figure 5.15(a)-(d)). In fact the linear profile of the electron and ion current densities shows the absence of plasma. When the first ionization coefficient α is very small these current densities are linear according to equation (5.27). Breakdown occurs in the biggest gap only below 0.1 mbar in figure 5.15(e)-(f) because in the multi-gap geometry breakdown can still ignite in the intermediate gaps. Moreover as the pressure decreases, the diffusion becomes more and more important compared to the drift. The constant current density across the gap defined by equation (5.23) is no longer respected as shown by figure 5.15(f) at 0.04 mbar. In fact equation (5.23) was deduced by neglecting the diffusion.
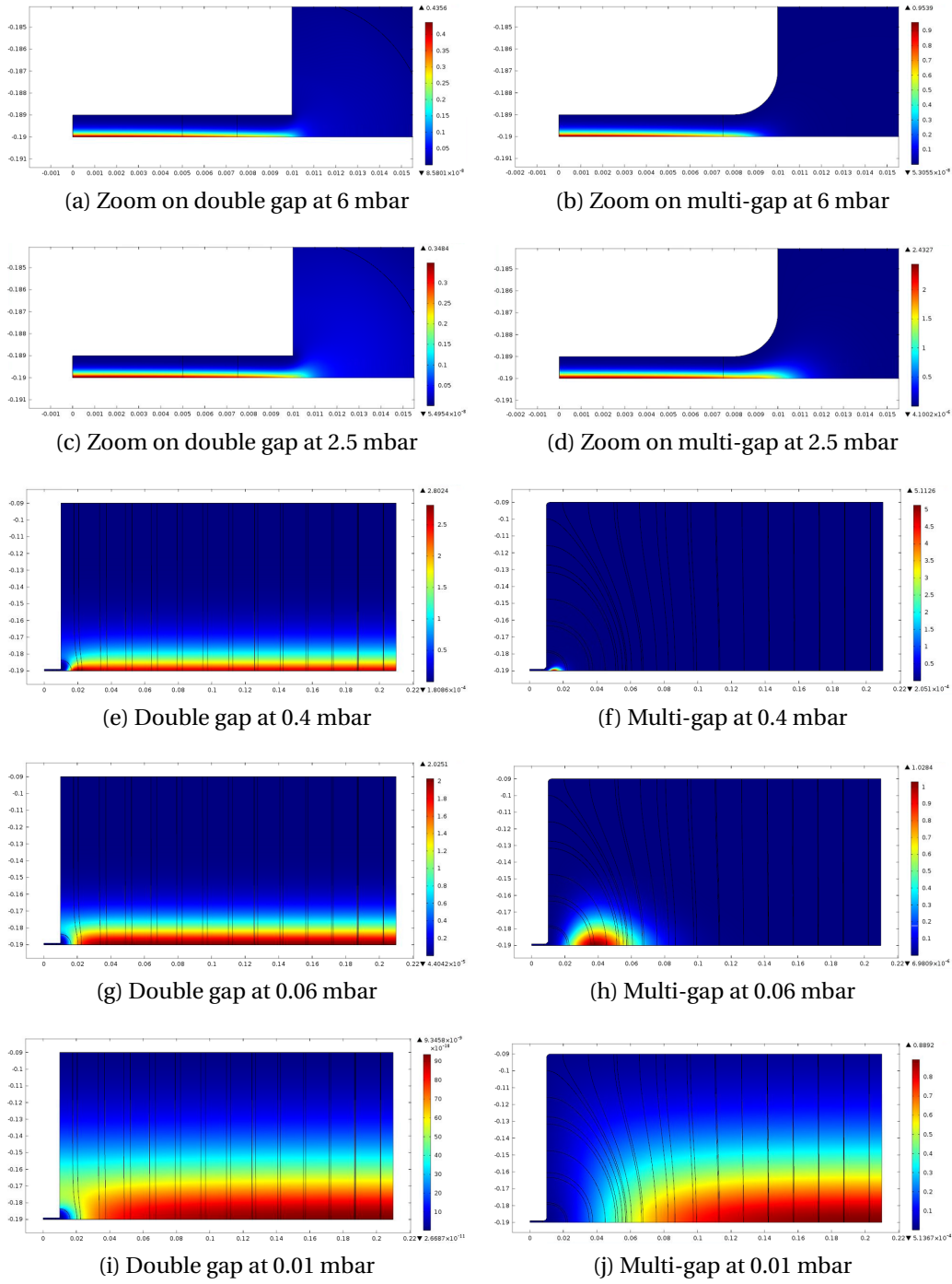
(a) Zoom on double gap at 6 mbar

(b) Zoom on multi-gap at 6 mbar

(c) Zoom on double gap at 2.5 mbar

(d) Zoom on multi-gap at 2.5 mbar

(e) Double gap at 0.4 mbar

(f) Multi-gap at 0.4 mbar

(g) Double gap at 0.06 mbar

(h) Multi-gap at 0.06 mbar

(i) Double gap at 0.01 mbar

(j) Multi-gap at 0.01 mbar

Figure 5.12: Electron densities ($1/m^3$) at breakdown voltage in a double gap geometry on the left and in a multi-gap geometry on the right. The smallest gap is 1 mm whereas the biggest one is 100 mm. The X-axis is the radius and the Y-axis is the height in m.
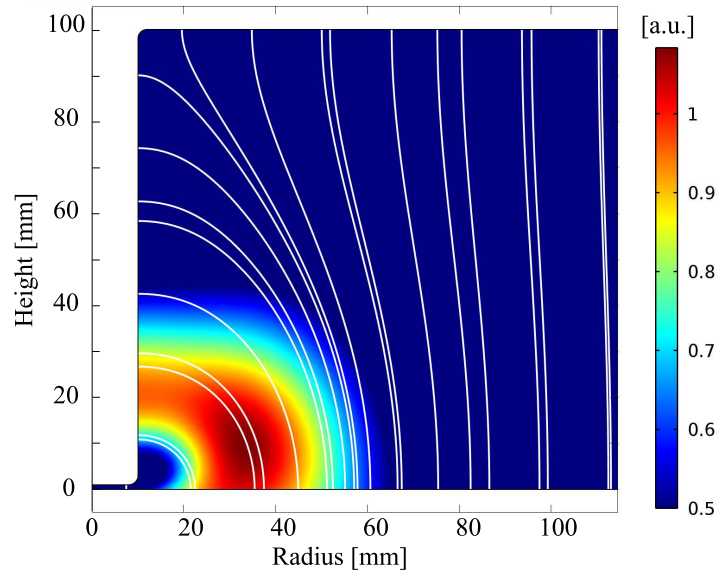
Figure 5.13: Calculated net current density of electron and ion fluxes following electric field lines (white) in double gap geometry (1 mm and 100 mm) at 0.039 mbar in air just before breakdown.

(a) 10 mbar

(b) 4 mbar

(c) 1mbar
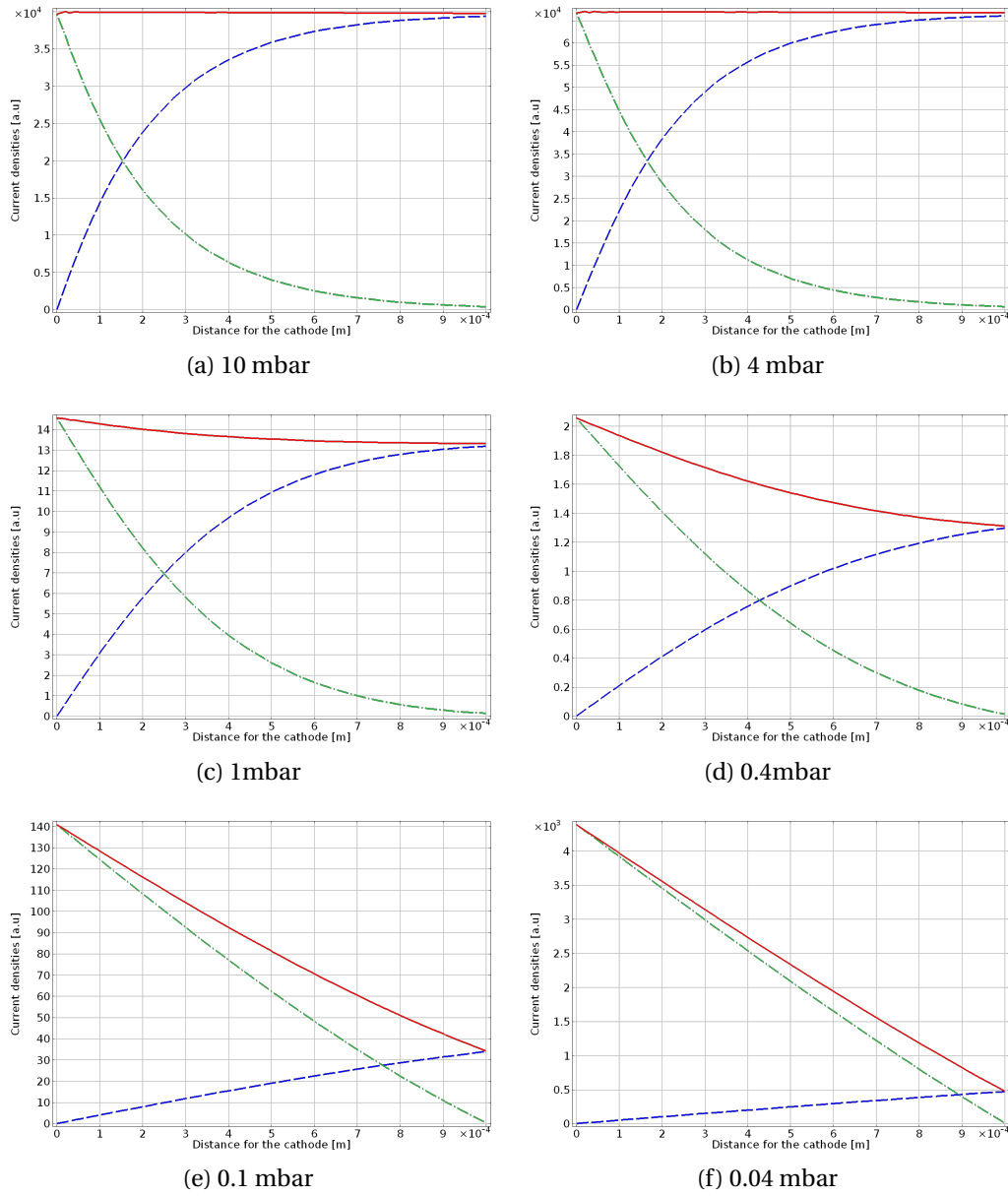
(d) 0.4mbar

(e) 0.1 mbar

(f) 0.04 mbar

Figure 5.14: Total current density (red full line), for ions (blue dashed line) and for electrons (green dash-dotted line) in the small gap (1 mm) of the multi-gap geometry (1 mm and 100 mm). The cut line is at $r = 0.002$ m.

(a) 10 mbar

(b) 4 mbar
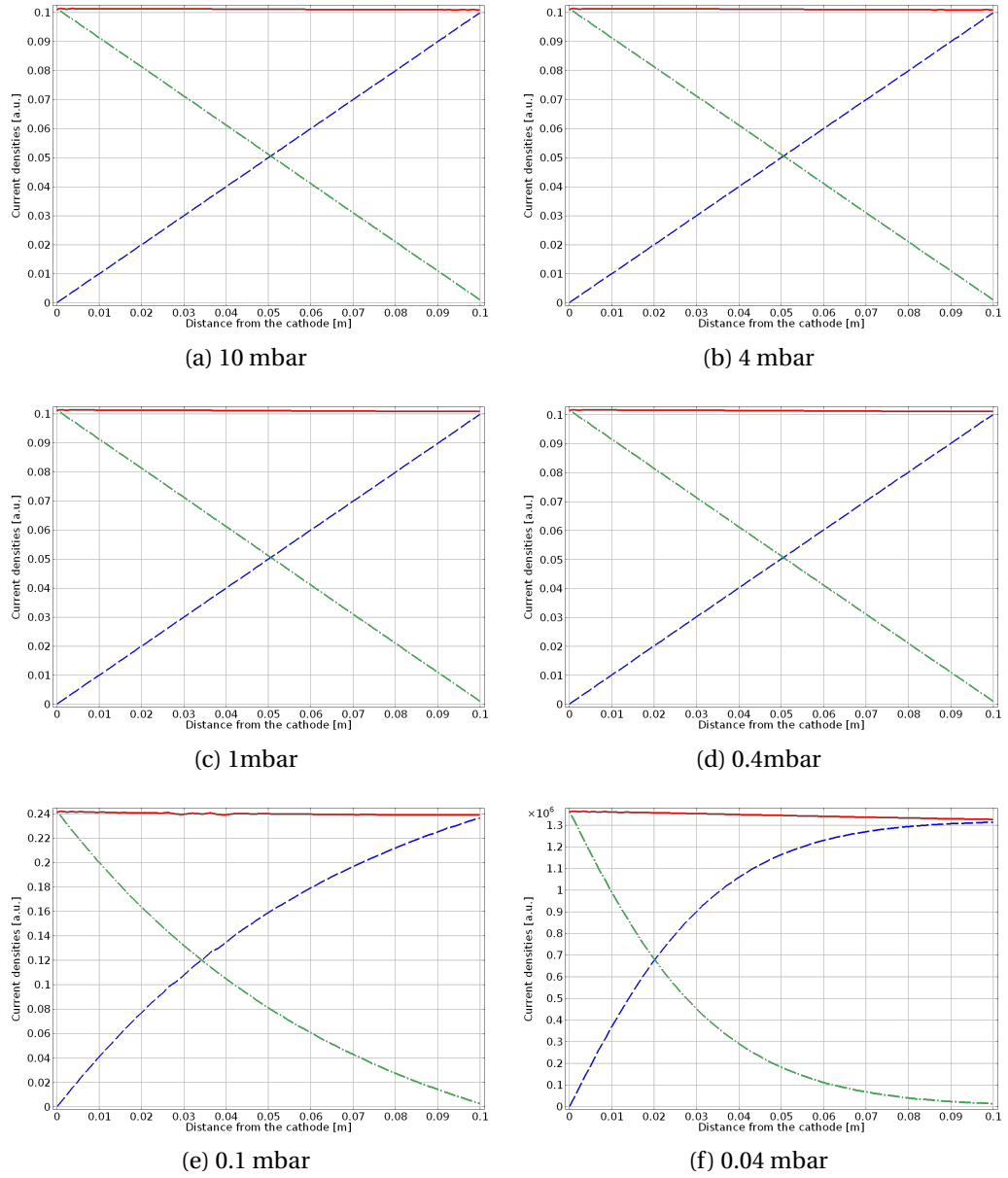
(c) 1mbar

(d) 0.4mbar

(e) 0.1 mbar

(f) 0.04 mbar

Figure 5.15: Total current density (red full line), for ions (blue dashed line) and for electrons (green dash-dotted line) in the big gap (100 mm) of the multi-gap geometry (1 mm and 100 mm). The cut line is at $r = 0.2$ m.

5.4   Ring assembly geometry

The electic field lines between the ring assembly and the chamber as well as between the rings itself are shown in figure 5.16 respectively figure 5.17. Obviously due to the complex nature of the setup there are many possible breakdown path lengths: Between the high voltage and the grounded ring as shortest path and between the high voltage ring and the vacuum chamber walls as longest path.

The calculated current densities in the ring assembly show the evolution of the breakdown location: At high pressure a channel forms between the rings (see figure 5.19(a)-(b)). When the pressure deceases it is more and more extending in the volume and moving away from the grounded rings and extending in the volume as in figure 5.19(c)-(h). This effect is also illustrated by the calculated ion density (figure 5.20). At low pressure the ions fill almost the full vacuum chamber in figure 5.20(a) due to the breakdown in the longest path and the higher diffusion at lower pressure. When the pressure increases the ion density becomes more and more compact but the discharge still breakdown against the wall. At around 1 mbar the breakdown takes place only between the rings. At high pressure the ion density is concentrate in thin channels between the rings according to the experimental observations (figure 5.20(g)-(h)).

These simulation results were obtained using the same swarm parameters and secondary electron emission coefficient as for the simpler geometries with no fitted parameters. Figure 5.18 shows the experimental and the simulated breakdown voltages versus pressure for the ring assembly. As in the multi-gap geometry, the breakdown voltage remains relatively constant over a decade of intermediate pressures. At high pressure the simulated breakdown voltages are slightly high than the experimental ones. In this region of pressure the densities become so high that the space charge which has been neglected could play a role. Moreover the neglected photo ionization processes are certainly also contributing to the breakdown voltage difference between the experimental and calculated breakdown voltages.

At lower pressure the calculations give higher values than the measured ones. Below 1 mbar the observation showed the apparition of positive corona. This kind of discharge needs a photo emission processes which have not been taken into account for the numerical simulation. Moreover the parameters chosen in the simulation could also contribute to the difference in breakdown voltage between simulation and experiment. As discussed in section 5.1.4 the swarm parameters and secondary
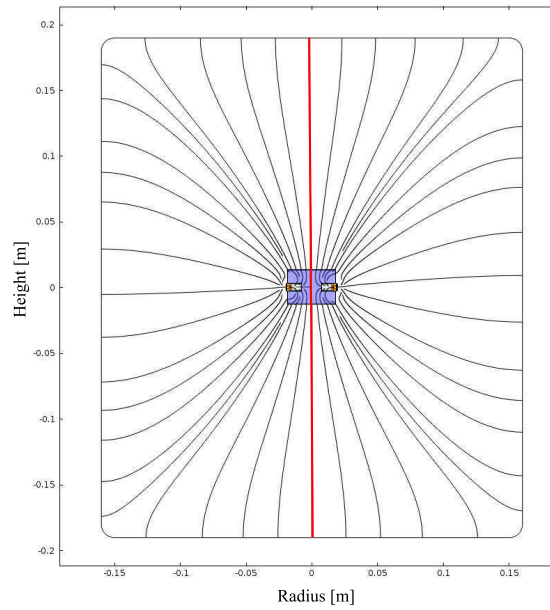
Figure 5.16: Electric field lines for a schematic of cylindrically-symmetric (axis in red) ring assembly geometry (yellow and brown) held by the PTFE holder (purple) in the grounded vacuum chamber.

electron emission coefficient can vary with the electric field and the pressure. The only parameter that has no been adjusted or calculated is the secondary electron emission coefficient. The simulation could therefore be made to fit the experimental values by suitable choice of γ_{se} (which then will be called effective secondary emission coefficient). The uncertainty in the values for γ_{se} means nevertheless that numerical simulation approach cannot give precise predictive results for the experimental breakdown voltage, but it is still useful to understand the general shape of the breakdown curve.
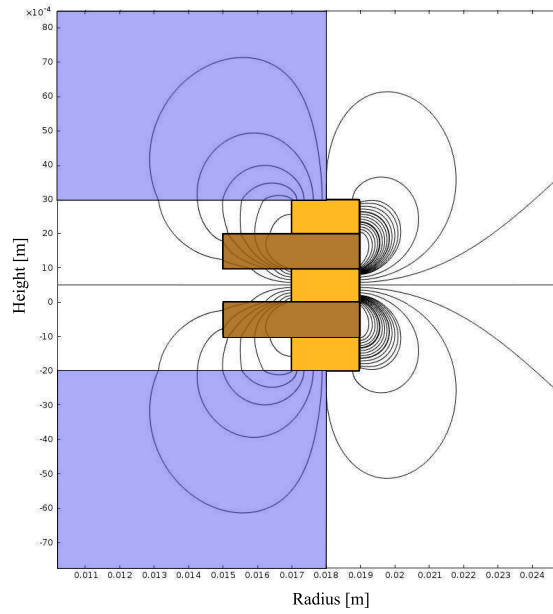
Figure 5.17: Zoom on the ring assembly in figure 5.16. Ring assembly with the same dimensions as in experiment (figure 3.6(b)) Electric field lines between the conductor rings (yellow) of a ring assembly hold by the PTFE holder (purple). The insulator rings (brown) internal barriers limit possible breakdown paths.
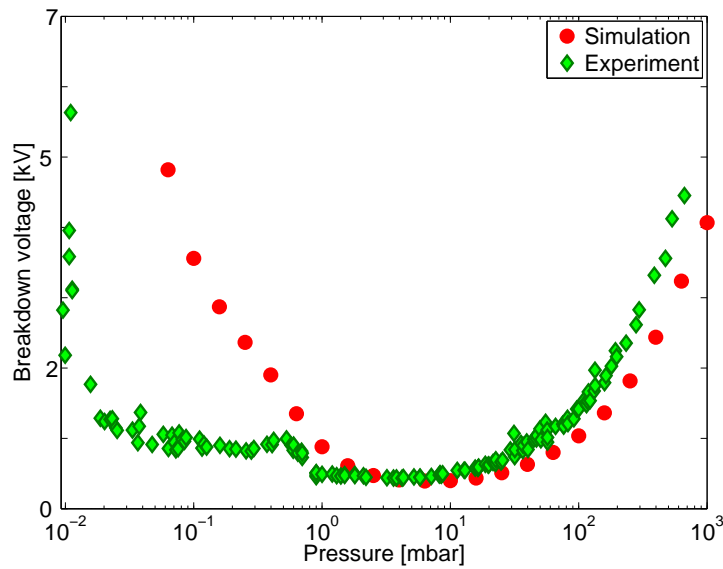

Figure 5.18: Experimental and simulation breakdown voltage versus pressure for the ring assembly geometry. No fitted parameters were used. The experimental values are the same as in figure 4.1 for the gas discharge region.

(a) 15 mbar

(b) 6 mbar

(c) 1.5 mbar

(d) 1 mbar

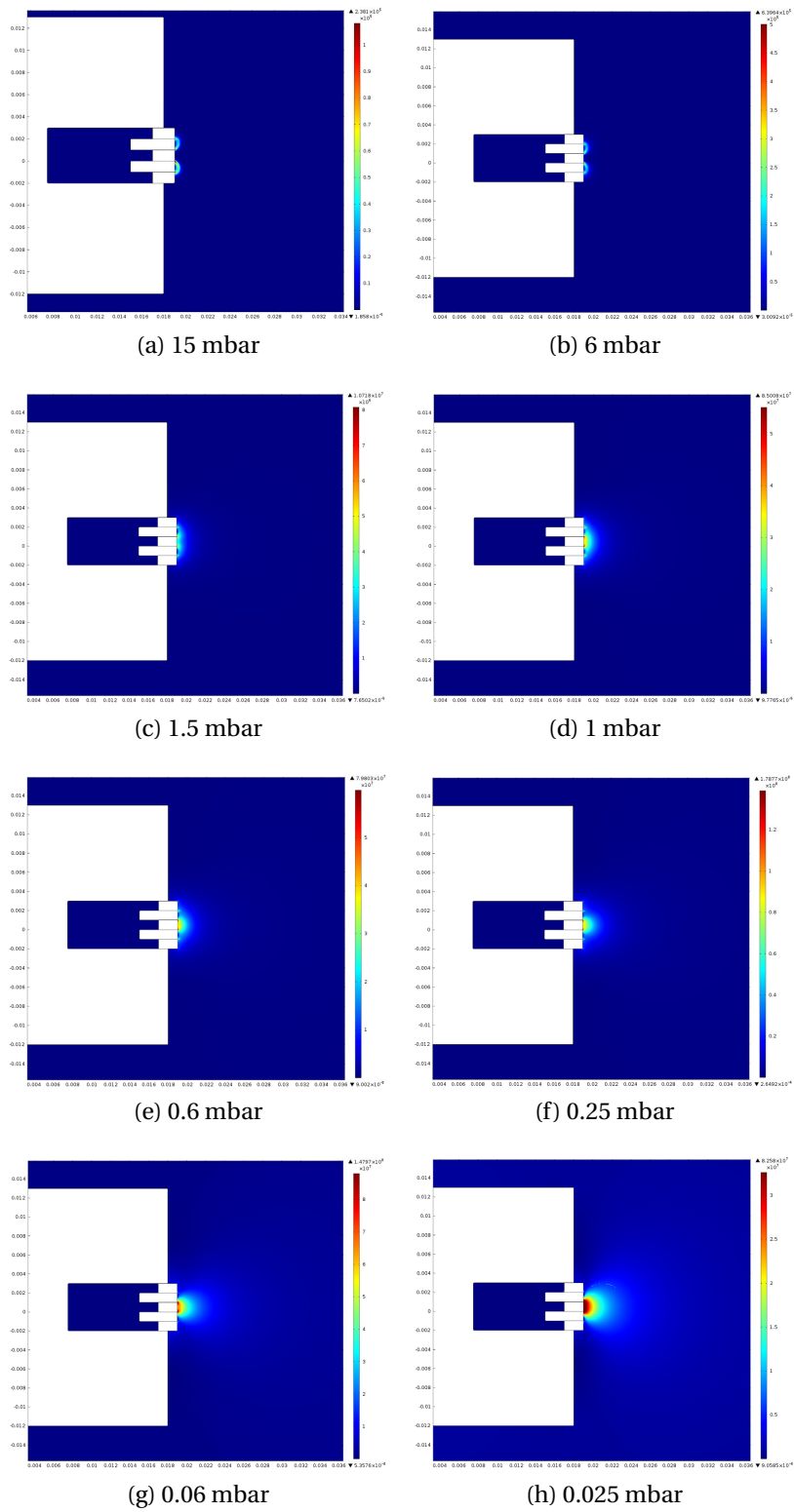(e) 0.6 mbar

(f) 0.25 mbar

(g) 0.06 mbar

(h) 0.025 mbar

Figure 5.19: Calculated net current density just before breakdown in the ring assembly (view as in figure 5.17) for various pressures. The X-axis and Y-axis are the radius respectively the height in m.

(a) 0.025 mbar

(b) 0.06 mbar

(c) 0.15 mbar

(d) 0.6 mbar

(e) 1.5 mbar

(f) 4 mbar
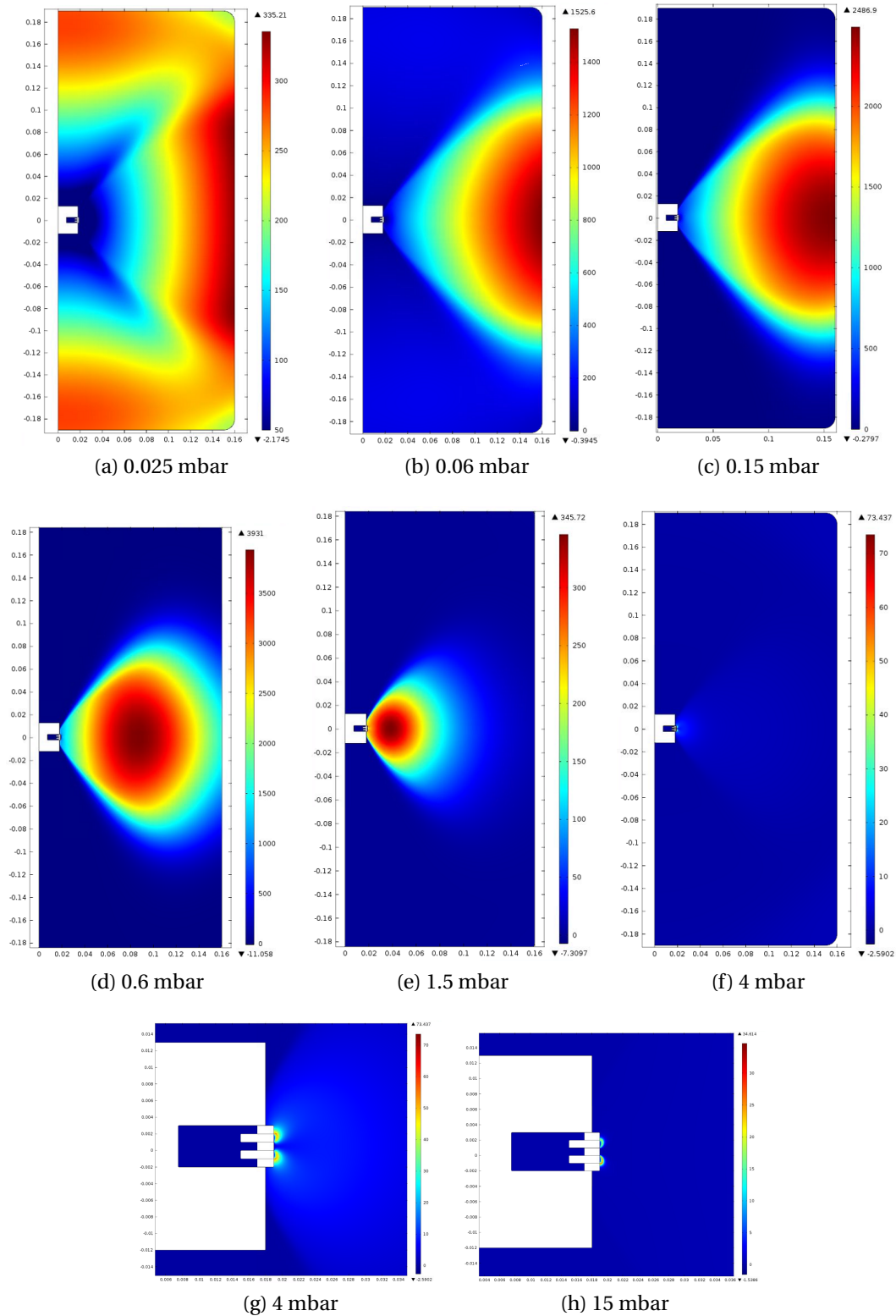
(g) 4 mbar

(h) 15 mbar

Figure 5.20: Calculated ion density just before breakdown in the ring assembly (view as in figure 5.16 and figure 5.17) for various pressures. The X-axis and Y-axis are the radius respectively the height in m.

5.5   Another approach for breakdown study

This section presents another interesting numerical method for breakdown study. Eriksson tried to calculated the streamer criterion (equation (2.13)) in a complex geometry using COMSOL 4.3 which offers the possibility to calculate integrals over field lines [19]. Breakdown criterion is defined by:

$$\int \alpha \mathrm{d}l = \alpha d = \ln(1 + 1/\gamma_{\mathrm{se}}) \,, \tag{5.30}$$

as shown in section 2.1. It is therefore theoretically possible to calculate the left term of equation (5.30) and observe if breakdown condition is reached. As $\gamma_{\mathrm{se}} = 0.01$ has been set in the simulation, breakdown should occur for $\alpha d > 4.61$ in parallel plates. In order to verify the breakdown condition the integral was calculated in a parallel plate geometry (1 mm) for each pressure with a breakdown voltage taken from the numerical simulation results presented in figure 5.11 from section 5.2. As illustrated in figure 5.21 the breakdown criterion fits well at high pressures. It should theoretically stay constant but below 100 mbar the value decreases. The breakdown criterion is defined over a limited reduced field range. Unfortunately large pressure and voltage ranges generate reduced electric fields over several orders of magnitude as presented in figure 5.22. At high pressure breakdowns, the reduced electric field remains quite low because both the pressure and the electric field are high. But for pressures below $p_{(V_{\mathrm{Bd}})_{\mathrm{min}}}$, the pressures becomes low and the electric field is still high, generating large values of E/p. Additionally the different swarm parameters (first ionization coefficient and particle diffusion and mobility) are also defined over a limited range of reduced electric field. In order to have a comparison with experimental values, this method has been applied to the ring assembly:

Based on experimental breakdown voltages the left term of equation (2.8) was solved for particle trajectories along electric field lines without attachment coefficient. Integrating the ionization coefficient along all possible breakdown paths gives not only the breakdown location but indicates the length of the breakdown path, the value of γ_{se} as well as the electric field strength. The maximum value of the integral of α over the field lines (for a fixed voltage and pressure) gives the most favorable breakdown location as shown in figure 5.23 where breakdown occurs between the rings at 666 mbar.

The breakdown path lengths over the gas discharge pressure range (figure 5.24) show a clear transition of breakdown locus. At high pressures the breakdown occurs in the shortest gap. When the pressure decreases below 10 mbar, the breakdown still occurs between the ring but is following longer field lines. The threshold of breakdown between the ring and the wall just below 1 mbar is consistent with the observations
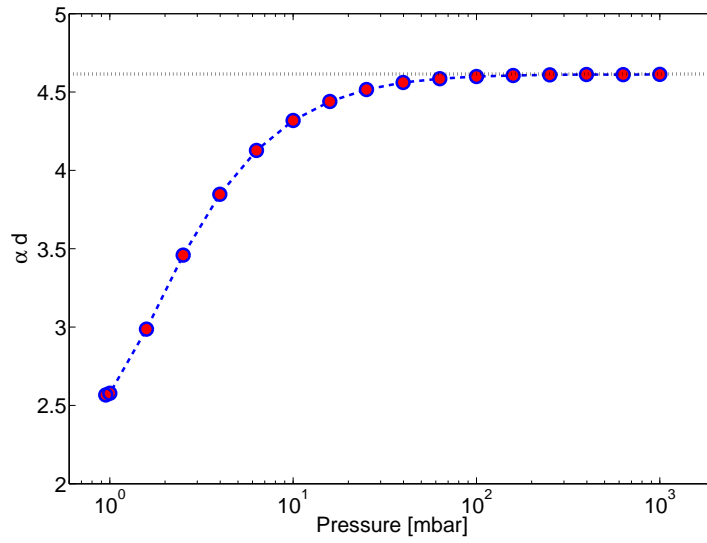
Figure 5.21: Value of $\alpha \mathrm{d}l$ from the numerical simulation integrated over the field lines in a 1 mm parallel plate geometry. The voltage was set to the calculated voltage from the fluid model simulation for each pressure. The horizontal line represent the value of $\ln(1 + 1/\gamma_{\mathrm{se}}) = 4.61$ with $\gamma_{\mathrm{se}} = 0.01$.
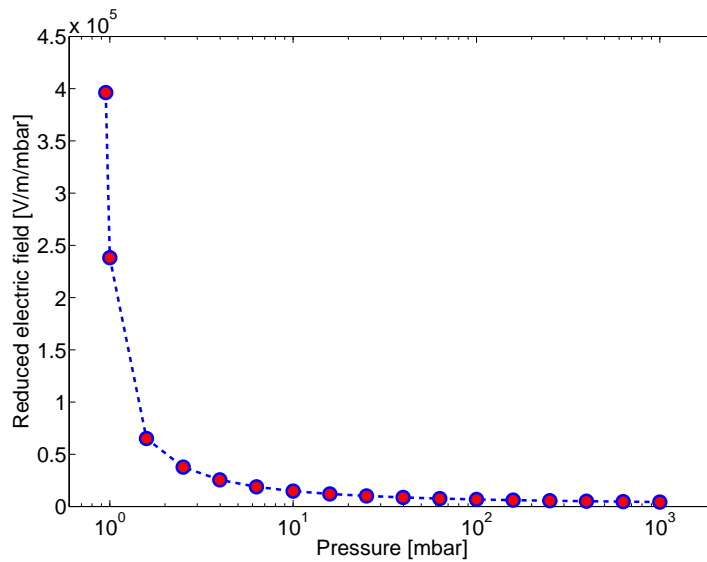

Figure 5.22: Reduced electric field in a 1 mm parallel plate geometry from the fluid model simulation for each pressure.
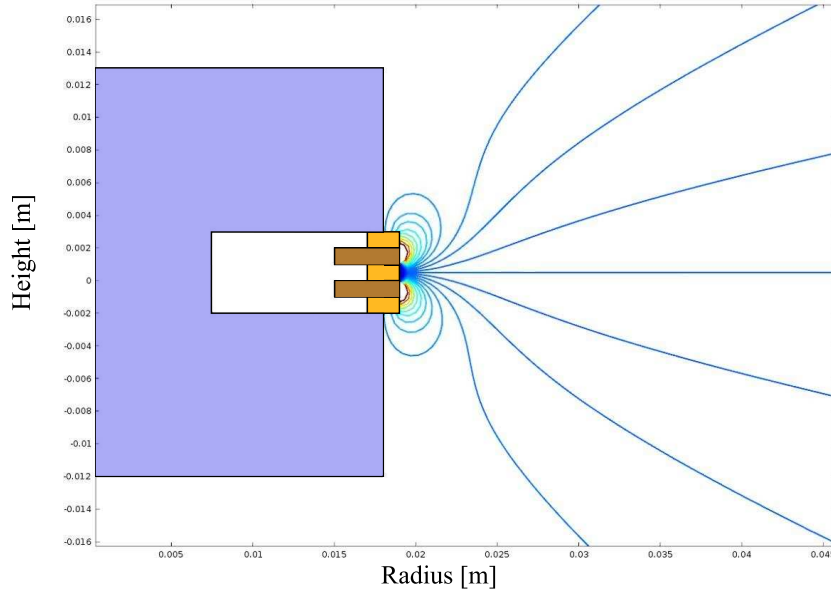
Figure 5.23: Calculation of the left term of equation (5.30) along electric field lines in the ring assembly at 666 mbar and 4452 V. The maximum values are colored in red and show that breakdown occurs between the rings.

(section 4.2). The longest breakdown path, corresponding to the distance from the ring to a top or bottom edge of the chamber, is longer than the chamber radius.

Obviously γ_{se} is not a constant and figure 5.25 shows that it can vary with the reduced electric field. γ_{se} depends on the contributions by positive ions, photons and metastables and therefore a generalized coefficient can be used to encompass a large pressure values in gas discharges, i.e., reduced electric field [14]. Moreover when the breakdown switches location and more importantly metal type, γ_{se} should show a clear transition. This is probably compensated by an additional processes from photons, positive ions or metasables. If these values of γ_{se} would have been used instead of 0.01 in the fluid model simulation, the breakdown voltage between the experiment and the calculations will be in better agreement.

There are some assumptions which could lead to errors: Attachment has been neglected, the particle trajectory has been set along the field line even if the diffusion at low pressure could change their paths, and $\alpha(E)$ for high E/p values is not well defined. Nevertheless it is possible with this approach to see the approximate breakdown location with much less effort than resolving the fluid model and electrostatics equations. Breakdown will occur where the breakdown condition described by equation (2.8) is the highest. The difficulty is to know exactly the different coefficients and how they evolve with the external parameters such as electric field and pressure.
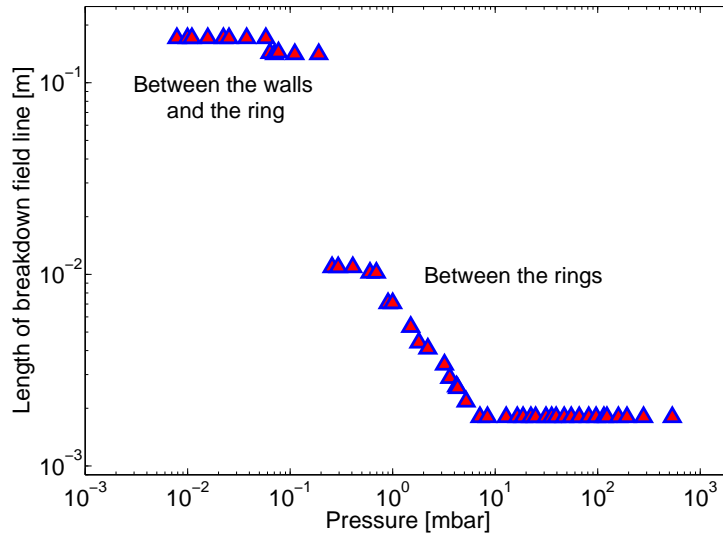
Figure 5.24: Breakdown path length in the ring assembly calculated using the experimental breakdown voltages for air as input for COMSOL.
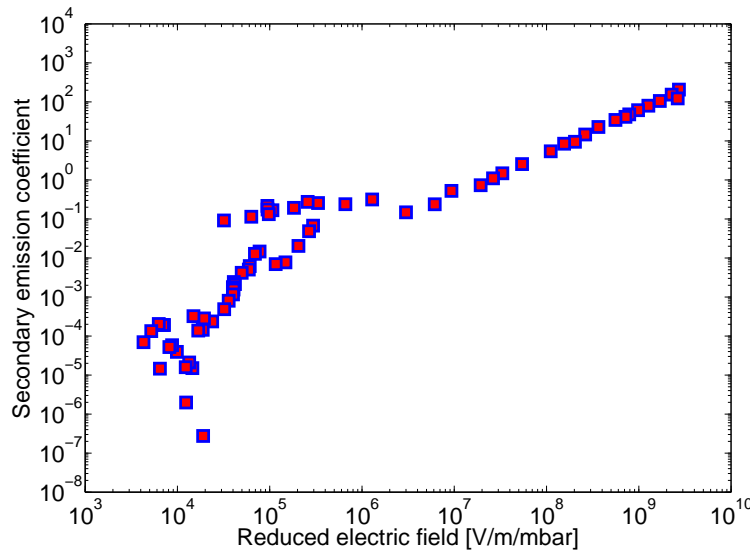

Figure 5.25: Secondary emission coefficient γ_{se} determined using the calculated value of the breakdown condition (equation (2.8)) in the ring assembly with the experimental breakdown voltages for air as input for COMSOL

In this chapter we focused on gas discharge breakdown because experimentally the breakdown voltage were low compared to vacuum discharges. As shown, the fluid

model is no longer valid for breakdowns in vacuum discharge area. Breakdown in high vacuum could nevertheless be calculated with a different approach: a particle in cell simulation which handles very low densities. Moreover the real slip ring assembly has brushes which should also be considered because breakdowns could also occur between brushes. The introduction of brushes in the numerical simulation implies a 3D geometry instead of a 2D cylindrically-symmetric one, leading to a large increase of memory use and calculation time even with a simple numerical model.

6 Conclusions and applications

This work presented an investigation of DC breakdown in a complex geometry (ring assembly) for a large pressure range. Breakdowns for a complex geometry showed not only gas discharges above 10^{-2} mbar but also discharges governed by vacuum discharge mechanisms below 10^{-3} mbar. Between 10^{-3} and 10^{-2} mbar both mechanisms act together. This distinction was also supported by optical emission spectroscopy and observations. Various geometrical parameters have shown their impact on breakdown voltage such as the external insulator barrier. Moreover, during the current-voltage investigations for gas discharges, the external circuit has been identified as the key component determining the kind of discharge after breakdown. The kind of discharge is not only dependent on pressure but also on current and voltage. Varying the current and voltage after the breakdown showed various discharges such as positive and negative corona, glow discharges or arcs. Some of these discharges with high currents have clearly shown that damages or failures are possible. For lower pressure vacuum discharges are in any case modifying slightly the experimental setup surface due to the nature of the breakdown mechanisms. The use during a long time of metal vapor to ignite vacuum discharges can finally lead to failure.

A numerical model based on fluid and electrostatics equations was developed for breakdown simulation in air. Starting from the understanding of breakdown in simple geometries like single gaps, the overall shape of breakdown voltage versus pressure has been clarified for more complex geometries such as double and multi-gap geometries. The constant voltage zone near the minimum breakdown voltage finds its origin in the multiple discharge path availability in complex geometries. The low (high) pressure thresholds are determined by the longest (shortest) electric field path length where breakdown occurs. The comparison of simulated and experimental breakdown voltages for a complex geometry such as a ring assembly was helpful to identify the strongly impacting parameters such as the secondary electron emission

coefficient and swarm parameters. Finally the general breakdown behavior in air for a complex geometry has been well described by a model which nevertheless needs to be improved to exactly fit the experimental data of gas discharges. Breakdown will not occur only in the smallest gap but can appear in longer gaps according to pressure.

The numerical simulation approach can be used to determine approximately the DC breakdown voltage for any kinds of geometry. Additionally the second approach based on the integral of the ionization coefficient along the electric field lines could even inform about the breakdown location.

The experimental and numerical approach are based on the same structure. We started with a geometry as simple as possible and tried to establish an understanding of breakdown. Based on this knowledge it was possible to further investigate step by step and finally to obtain a description of breakdown in more complex geometries.

6.1   Impact for the industrial project

Initially the objective of our project on "Robust Electrical Transfer System" (RETS 129.62) funded by European Space Agency (ESA) was to identify the weakness of the slip ring assembly of our industrial partner RUAG Space [1]. Rapidly our investigations showed high breakdown voltages compared to the functional voltages for their slip ring assembly. Instead of improving their design, a test bench has finally been setup to qualify their products: A breakdown limit test and a functional test. Both tests will be done with an automated base procedure similar to our experimental investigations: pressure and voltage sweep. The change in temperature will additionally be tested. The first test will determine the worst case breakdown voltage limit. The second test is a simulation of a real operational situation and should show if the device is safe under standard functional conditions.

These tests are approved by ESA to qualify power transmission mechanisms and should contribute to improve the reliability of this important functional part in satellites.

After investing in several research and development projects during the past few years, our industrial partner RUAG Space got its biggest contract ever signed at the end of the year 2011: 167 collectors (containing slip ring assembly). These pieces will equip 81 satellites of the Iridium satellite constellation, next worldwide telecommunication satellite generation [79].

6.2 Outlook

This thesis focused on DC breakdown in complex geometries. We first consider further experimental investigations followed by numerical ones.

Secondary electron emission mechanisms are key processes for breakdown in gas discharges. The number of released secondary electrons per ion impact is not constant but depends on many parameters such as pressure, gas type, electric field or electrode material. It is hard to quantify the secondary electron coefficient in complex geometries because it depends on the reduced electric field [75] and a simple geometry such as parallel plate is needed for this kind of experimental investigation. A change of the secondary electron emission coefficient may for example impact on the minimum breakdown voltage as shown in figure 5.5. A change of conductor material will not only change the secondary electron emission but also impacts on breakdown of vacuum discharges because the work function is changed. Using conductors with a high work function will increase the breakdown voltages for vacuum discharges, but these materials should have high electric conductivity in order to keep an optimal electric power transmission.

Moreover each kind of discharge observed such as corona, glow discharges, arcs could be investigated for complex geometries in much more detail with time-resolved spectroscopy, fast imaging or current/voltage characteristics. The study of the transition between a glow discharge and an arc for example could give more information on how to avoid this phenomena and damages by the same time.

The numerical model could be extended with a secondary electron emission coefficient varying with the reduced electric field to obtain a more realistic calculation but this coefficient needs to be known. Additional processes such as space charge at high pressures or photoionization at lower pressures could also complete the model. The model has been developed for DC breakdown in gas discharges but it could be modified to calculate discharges with an external circuit or with a pulsed voltage input. This approach is useful to obtain the particle densities, the current flowing between the electrodes or even the power of the discharge. The ring assembly is the simplified representation of a slip ring assembly. The breakdown could also be calculated for this really complex geometry including the brushes but using a 3D geometry. The calculation time will nevertheless strongly increase with such kind of input.

Finally the vacuum breakdown could be investigated with a particle in cell approach because the densities are so low that the fluid model is no longer valid. The Paschen model is therefore replaced by typical processes for vacuum breakdown such as field or thermionic emission.

Bibliography

[1] ESA RETS project 129.62, Technical Notes.

[2] USC satellite database
http://www.ucsusa.org/nuclear_weapons_and_global_security/space_
weapons/technical_issues/ucs-satellite-database.html.

[3] R.K. DeKosky. William Crookes and the fourth state of matter. *Isis*, 67(1):36–60, 1976.

[4] I. Langmuir. Oscillations in ionized gases. *Proceedings of the National Academy of Sciences of the United States of America*, 14(8):627, 1928.

[5] F.F. Chen and J.P. Chang. *Lecture notes on principles of plasma processing*. Springer, 2003.

[6] M.A. Lieberman and A.J. Lichtenberg. *Principles of Plasma Discharges and Materials Processing*. John Wiley & Sons, Inc., 2nd edition, 1994.

[7] J.D. Huba. NRL: plasma formulary. Technical report, DTIC Document, 2004.

[8] W. Rieder. *Plasma und Lichtbogen*. Friedr. Vieweg & Sohn, Braunschweig, 1967.

[9] Y.P. Raizer. *Gas discharge physics*. Springer-Verlag Berlin, 1991.

[10] M. J. Druyvesteyn and F. M. Penning. The mechanism of electrical discharges in gases of low pressure. *Rev. Mod. Phys.*, 12:87–174, Apr 1940.

[11] J.M. Meek and J.D. Craggs. *Electrical Breakdown of Gases*. John Wiley & Sons, Ltd., New York, NY, 1978.

[12] Heinz Raether. *Electron avalanches and breakdown in gases*. Butterworths London, 1964.

[13] L.B. Loeb and J.M. Meek. *The mechanism of the electric spark*. Stanford University Press, 1941.

Bibliography

[14] E. Husain and R.S. Nema. Analysis of paschen curves for air, N2 and SF6 using the townsend breakdown equation. *Electrical Insulation, IEEE Transactions on*, (4):350–353, 1982.

[15] O. Goossens, T. Callebaut, Y. Akishev, A. Napartovich, N. Trushkin, and C. Leys. The dc glow discharge at atmospheric pressure. *IEEE Trans. on Plasma Science*, 30(1):176–177, 2002.

[16] J.S. Chang, P.A. Lawless, and T. Yamamoto. Corona discharge processes. *IEEE Trans. on Plasma Science*, 19(6):1152–1166, 1991.

[17] J.J. Lowke and R. Morrow. Theory of electric corona including role of plasma chemistry. *Pure & Appl. Chem.*, 66(6):1287–1294, 1994.

[18] P. Osmokrovic, M. Vujisic, K. Stankovic, A. Vasic, and B. Loncar. Mechanism of electrical breakdown of gases for pressures from 10^{-9} to 1 bar and inter-electrode gaps from 0.1 to 0.5 mm. *Plasma Sources Sci. Technol.*, 16(3):643, 2007.

[19] G. Eriksson. Easy evaluation of streamer discharge criteria. In *Proc. 2012 COMSOL Conf. (Milan, Italy)*, 2012.

[20] M. Abdel-Salam and E.K. Stanek. On the calculation of breakdown voltages for uniform electric fields in compressed air and SF6. *Industry Applications, IEEE Transactions on*, 24(6):1025–1030, 1988.

[21] J.D. Cobine, G.A. Farrall, L.P. Harris, G. Ecker, and A.N. Greenwood. *Vacuum Arcs.* J.M. Lafferty, ed., Wiley Interscience, New York.

[22] G.A. Farrall. *Vacuum Arcs : Chapter 2*, chapter Electrical Breakdown in Vacuum. J. M. Lefferty Wiley Interscience, New York, 1980.

[23] J.P. Barbour, W.W. Dolan, J.K. Trolan, E.E. Martin, and W.P. Dyke. Space charge effects in field emission. *Phys. Rev.*, 92(1):45–54, 1953.

[24] L.W. Nordheim. The effect of the image force on the emission and reflexion of electrons by metals. *Proceedings of the Royal Society of London. Series A*, 121(788):626–639, 1928.

[25] H.C. Miller. Values of fowler-nordheim field emission functions $v(y)$, $t(y)$, $s(y)$. *J. Franklin Institute*, 282(6):382–388, 1966. General Electric Research and Development Center, Schenectady, New York.

[26] H.C. Miller. Values of the election emission functions $v(y)$, $t(y)$, $\theta(y)$; $y \geq 1$. *J. Franklin Institute*, 287(4):347–351, 1969. Laboratory Operation, General Electric Company, Philadelphia, Pennsylvania.

[27] K. Tsuruta. Change in work function of vacuum-gap electrode by residual gas adsorption. *Japan. J. Appl. Phys.*, 25(4):650–651, 1986.

[28] K. Tsuruta and M. Yano. Residual gas adsorption on electrode surfaces in vacuum. *Japan. J. Appl. Phys.*, 22(6):1017–1019, 1983.

[29] S. Kobayashi, Y. Saito, Y. Nagai, and A. Yamamoto. Vacuum breakdown strengh of vacuum degassed oxygen free copper electrodes. *IEEE Trans. on Dielectrics and Electrical Insulation*, 28(4):500–506, 1993.

[30] A. Descoeudres, T. Ramsvik, S. Calatroni, M. Taborelli, and W. Wuensch. DC breakdown conditioning and breakdown rate of metals and metallic alloys under ultrahigh vacuum. *Phys. Rev. ST Accel. Beams*, 12(032001):1–8, 2009.

[31] A. Descoeudres, S. Calatroni, and M. Taborelli. DC breakdown experiments for CLIC. *Proceedings of EPAC08*, pages 577–579, 2008.

[32] S. Kobayashi. Recent experiments on vacuum breakdown of oxygen free copper electrodes. *IEEE Trans. on Dielectrics and Electrical Insulation*, 4(6):841–847, 1997.

[33] B. Bonin. Field emission and surface conditioning. *Vacuum*, 46(8):907–912, 1995.

[34] H.P.S. Powell and P.A. Chatterton. Prebreakdown conduction between vacuum insulated electrodes. *Pregamon Press Ltd*, 20(10):419–429, 1970.

[35] K. Jousten. *Wutz Handbuch Vakuumtechnik*. Vieweg Verlag, 9th edition.

[36] Von Roll Holding AG, Vetronite® G-11, http://www.vonroll.com/media/files/downloads/brochures/Composites_EN.pdf.

[37] Advanced Polymer Technologies, Ultem® 2300R Resin, http://www.aptllc.net/datasheets/Ultem2300R.pdf.

[38] Corning Incorporated, Lighting & Materials, Macor® datasheet, http://www.corning.com/docs/specialtymaterials/pisheets/Macor.pdf.

[39] BEHLKE, Fast high voltage transistor switches http://www.behlke.com/pdf/201-03-gsm.pdf.

[40] M.M. Pejovic, G.S. Ristic, and J.P. Karamarkovic. Electrical breakdown in low pressure gases. *J. Phys. D: Applied Physics*, 35(10):R91, 2002.

[41] M.M. Pejović, E.N. Živanović, M.M. Pejović, and J.P. Karamarković. Analysis of processes responsible for the memory effect in air at low pressures. *Plasma Sources Science and Technology*, 19(4):045021, 2010.

Bibliography

[42] Princeton Instruments, inc. *WinSpec/32 User's Manual*, Software Version 2.3, Manual Revision K edition, 1998.

[43] V.A. Lisovsky and V.D. Yegorenkov. Low-pressure gas breakdown in combined fields. *J. Phys. D: Applied Physics*, 27(11):2340, 1994.

[44] D.P. Lymberopoulos and D.J. Economou. Fluid simulations of glow discharges: Effect of metastable atoms in argon. *Journal of applied physics*, 73(8):3668–3679, 1993.

[45] R. Hackam. Comparison between 50Hz AC and DC vacuum breakdown. *J. Phys. D: Appl. Phys.*, 8:L53–L55, 1975.

[46] R. Hackam and L. Altcheh. AC (50Hz) and DC electrical breakdown of vacuum gaps and with variation of air pressure in the range $10^{-9} - 10^{-2}$ Torr using OFHC copper, nickel, aluminium, and niobium parallel planar electrodes. *J. Appl. Phys.*, 46(2):627–636, 1975.

[47] V Lj Marković, SR Gocić, and SN Stamenković. New distributions of the statistical time delay of electrical breakdown in nitrogen. *Journal of Physics D: Applied Physics*, 39(15):3317, 2006.

[48] NIST atomic spectra database lines form http://physics.nist.gov/PhysRefData/ASD/lines_form.html.

[49] Alf Lofthus and Paul H Krupenie. The spectrum of molecular nitrogen. *Journal of physical and chemical reference Data*, 6:113, 1977.

[50] Z.L. Petrović, N. Škoro, D. Marić, C.M.O Mahony, P.D. Maguire, M. Radmilović-Rađenović, and G. Malović. Breakdown, scaling and volt–ampere characteristics of low current micro-discharges. *J. Phys. D: Appl. Phys.*, 41(19):194002, 2008.

[51] R. Morrow. Numerical modelling of time-dependent electrical breakdown in non-uniform electric fields. In *Proc. XVIII ICPIG (Swansea, Wales)*, 1987.

[52] A. Villot, Y.F.J. Gonthier, E. Gonze, and A. Bernis. Numerical model of current–voltage curve for the wire-cylinder electrostatic precipitators in negative voltage in the presence of nonpolar gases. *IEEE Trans. on Plasma Sci.*, 38(8):2031–2040, 2010.

[53] N. Leoni and B. Paradkar. Numerical simulation of Townsend discharge, Paschen breakdown and dielectric barrier discharges. In *Proc. IS&T's NIP, Springfield, VA*, page 229, 2009.

[54] R. Schnyder, A.A. Howling, D. Bommottet, and C. Hollenstein. DC breakdown in gases for complex geometries from high vacuum to atmospheric pressure. *J. Phys. D: Applied Physics*, 46(28):5205, 2013.

[55] *COMSOL Inc.* http://www.comsol.com.

[56] D.B. Graves and K.F. Jensen. A continuum model of dc and rf discharges. *IEEE Trans. Plasma Sci.*, 14(2):78–91, 1986.

[57] R.J. Kee, M.E. Coltrin, and P. Glarborg. *Chemically reacting flow: theory and practice*. Wiley-Interscience, 2003.

[58] S.G. Jennings. The mean free path in air. *J. of Aerosol Science*, 19(2):159–166, 1988.

[59] K. Yanallah, F. Pontiga, and A. Castellanos. Numerical simulation of an oxygen-fed wire-to-cylinder negative corona discharge in the glow regime. *J. Phys. D: Appl. Phys.*, 44(5):055201, 2011.

[60] I.M. Cohen. Asymptotic theory of a photoionization chamber. *Physics of Fluids*, 8:2097, 1965.

[61] M.A. Jog, I.M. Cohen, and P.S. Ayyaswamy. Electrode heating in a wire-to-plane arc. *Phys. Fluids B*, 4(2):465–472, 1992.

[62] V. Guerra, M.J. Pinheiro, B.F. Gordiets, J. Loureiro, and C.M. Ferreira. Calculated data on electron transport and excitation rate coefficients in and discharges. *Plasma Sources Science and Technology*, 6(2):220, 1997.

[63] E.W. McDaniel. *Collision phenomena in ionized gases*. John Wiley & Sons, Inc., 1964.

[64] G.L. Braglia and J.J. Lowke. Comparison of monte carlo and boltzmann calculation of electron diffusion to absorbing electrodes. *J. Phys. D: Appl. Phys.*, 12(11):1831, 2001.

[65] G.J.M. Hagelaar and L.C. Pitchford. Solving the boltzmann equation to obtain electron transport coefficients and rate coefficients for fluid models. *Plasma Sources Sci. Technol.*, 14(4):722, 2005.

[66] A.V. Phelps and L.C. Pitchford. A compilation of atomic and molecular data for nitrogen, but with a rescaling of the c state (multiplied by 0.67) at 11.03 ev and a separation of the ionization into two levels. *Phys. Rev.*, 31:2932, 1985.

[67] SA Lawton and AV Phelps. Excitation of the b 1Σ+ g state of O2 by low energy electrons. *The Journal of Chemical Physics*, 69(3):1055–1068, 1978.

[68] *BOLSIG+.* http://www.bolsig.laplace.univ-tlse.fr/.

[69] S. Dujko, U. Ebert, R.D. White, and Z.Lj. Petrovic. Boltzmann equation analysis of electron transport in a n2–o2 streamer discharge. *Jap. J. Appl. Phys*, 50:08JC01, 2011.

[70] A. Bekstein, M. Yousfi, M. Benhenni, O. Ducasse, and O. Eichwald. Drift and reactions of positive tetratomic ions in dry, atmospheric air: Their effects on the dynamics of primary and secondary streamers. *J. Appl. Phys.*, 107(10):103308–103308, 2010.

[71] D. Nelson, M. Benhenni, O. Eichwald, and M. Yousfi. Ion swarm data for electrical discharge modeling in air and flue gas mixtures. *J. Appl. Phys.*, 94(1):96–103, 2003.

[72] E.M. Baroody. A theory of secondary electron emission from metals. *Phys. Rev.*, 78(6):780, 1950.

[73] Y. Sosov and C.E. Theodosiou. Determination of electric field-dependent effective secondary emission coefficients for he/xe ions on brass. *J. Appl. Phys.*, 95(8):4385–4388, 2004.

[74] Ph. Guillot, Ph. Belenguer, L. Therese, V. Lavoine, and H. Chollet. Secondary electron emission coefficient of standard samples for GDOES. *Surf. Interface Anal.*, 35:590–592, 2003.

[75] G. Auday, Ph. Guillot, J. Galy, and H. Brunet. Experimental study of the effective secondary emission coefficient for rare gases and copper electrodes. *Journal of applied physics*, 83(11):5917–5921, 1998.

[76] A.N. Lodygin, L.M. Portsel, and Y.A. Astrov. DC Townsend discharge in nitrogen: Temperature-dependent phenomena. *Contributions to Plasma Physics*, 52(8):682–691, 2012.

[77] A.A. Kudryavtsev and L.D. Tsendin. Cathode boundary conditions for fluid model discharges on the right-hand branch of the paschen curve. *Technical Physics Letters*, 28(8):621–624, 2002.

[78] D. Marić, N. Škoro, P.D. Maguire, C.M.O Mahony, G. Malović, and Z.L. Petrović. On the possibility of long path breakdown affecting the paschen curves for microdischarges. *Plasma Sources Sci. Technol.*, 21(3):035016, 2012.

[79] E. Borloz. A Nyon, RUAG Space vient de décrocher la lune. *24 heures.* Published 30.10.2011.

Acknowledgements

Une thèse est un processus avec des hauts et des bas que je n'aurais su réaliser sans mes superviseurs. J'aimerais donc remercier Christoph Hollenstein et Alan Howling d'abord pour m'avoir permis d'effectuer un travail de doctorat dans leur groupe et pour avoir pris le temps de accompagner pendant ces années de dur labeur. Durant les longues discussions, ces deux savants de la physique des plasmas possèdant une énorme source de connaissance dans ce domaine pointu, ont été d'une aide efficace.

Ce travail de recherche appliqué a été possible grâce à la collaboration de notre partenaire industriel RUAG Space Nyon, que je remercie. Un merci particulier à Daniel Bommottet qui nous a laissé une certaine liberté académique tout au long du projet RETS.

Je voudrais également remercier les membres du jury Philipp Rudolf von Rohr, Nebuloni Stefano and Furno Ivo pour avoir consacré du temps à lire et commenter ma thèse mais surtout d'avoir assité à ma défense orale.

Un grand merci également à tout le groupe des plasmas industriels: Boris, Michael, Marina, Sylvain, Pierre, David, Mouche, Loïc, Remy et Phillipe: Pour les discussions à midi qui ont souvent été très enrichissantes touchant tous les domaines possibles et imaginables, allant de la cosanguinité en Valais à la météo du dimanche en passant par les tensions franco-anglaises à travers les millénaires. Pour les nombreuses parties de fléchettes qui ont suscité beaucoup d'émotions lors des records tout comme des contre performances, même si en fin de thèse j'ai renoncé à y jouer. À Boris de m'avoir transmis cette passion magique de la physique des plasmas alors qu'il supervisait mon travail de Master. À Marina d'avoir apporté une touche féminine au labo. À Mouche frère valaisan toujours là pour me rappeler mes origines. À Loïc pour son partage de sa passion, la musique classique. À Pierre pour ses pécieux conseils aussi

115

Schnyder Ralph
Route de la Plaine 42
1958 Uvrier

Switzerland (Bratsch, VS)
Single
Mobile +41 78 741 32 08

ralph.schnyder@postmail.ch

PhD in physics, I am looking for new challenges in research and development. As a fast learner I am able to quickly solve problems through my perseverance and organizational skills.

Education

PhD in Physics at Swiss Federal Institute of Technology Lausanne (EPFL) Experimental investigation of high voltage breakdown mechanisms in vacuum and development of numerical simulation model for direct current (DC) gas breakdown based on theoretical research.	2010 - current
Master of Science MSc in Physics at EPFL Master thesis in plasma processing (financed by Oerlikon Solar).	2005 - 2010

Projects & Work experience

European Space Agency (ESA) project in collaboration with RUAG Space Switzerland Nyon Analysis of breakdowns in satellite high power transmission device. As physicist, technical expertise brought an efficient solution: Development of a qualification test bench (functional limits and quality certifications approved by ESA) which could facilitate product selling or reassure clients. The good project progress was assured by short deadlines, regular reporting and good communication with the partners.	2010 - 2013
Principal teaching assistant (general physics for Prof. Tran at EPFL) Management of assistants and conception of exercises and tests for the students.	2011 - 2013
Scientific collaborator at Institute of Applied Radio Physics (IRA) Lausanne Proceeding paper as co-author for SSRMP Annual Scientific Meeting 2009: "Exposure of the Swiss population from radiological examinations: a prospective study to estimate the examination frequency".	2009

Languages

Swiss German	native, fluent
French	bilingual, fluent
German	C1, speaking: fluent, written: intermediate
English	C1, fluent (working field)

Complementary knowledge

Software	COMSOL Multiphysics, Matlab, Labview, Mathematica, OOPIC
Programming languages	LaTeX, SQL, HTML, PHP, C++
Microsoft office	Excel, Word, PowerPoint, Access
Management courses	Engaged scholarship (4 credits), Leading a team (3 days)

Extra curricular activities

Athletics: Throwing (shot put) trainer for the regional team (cadres valaisans) Training organization and coordination with regional clubs/ federation	2008-current